Universitat Politècnica de Catalunya
Programa de Doctorat en Matemàtica Aplicada

Departament d'Enginyeria Civil i Ambiental

LOCALLY ADAPTIVE PHASE-FIELD MODELS AND TRANSITION TO FRACTURE

by

Alba Muixí Ballonga

Doctoral Thesis
Advisors: Sonia Fernández-Méndez
Antonio Rodríguez-Ferran

Barcelona, July 2020

Abstract

Locally adaptive phase-field models and transition to fracture

Alba Muixí Ballonga

This thesis proposes a new computational model for the efficient simulation of crack propagation, through the combination of a phase-field model in small subdomains around crack tips and a discontinuous model in the rest of the domain. The combined model inherits the advantages of both approaches. The phase-field model determines crack propagation at crack tips, and the discontinuous model explicitly describes the crack elsewhere, enabling to use a coarser discretization and thus reducing the computational cost.

In crack-tip subdomains, the discretization is refined to capture the phase-field solution, while in the discontinuous part, sharp cracks are incorporated into the coarse background discretization by the eXtended Finite Element Method (XFEM). As crack-tip subdomains move with crack growth, the discretization is automatically updated and phase-field bands are replaced by sharp cracks in the wake of cracks.

The first step is the development of an adaptive refinement strategy for phase-field models. To this end, two alternatives are proposed. Both of them consider two types of elements, standard and refined, which are mapped into a fixed background mesh. In refined elements, the space of approximation is uniformly h-refined. Continuity between elements of different type is imposed in weak form to handle the non-conformal approximations in a natural way, without spreading of refinement nor having to deal with hanging nodes, leading to a very local refinement along cracks.

The first adaptive strategy relies on a Hybridizable Discontinuous Galerkin (HDG) formulation of the problem, in which continuity between elements is imposed in weak form. The second one is based on a more efficient Continuous Galerkin (CG) formulation; a continuous FEM approximation is used in the standard and refined regions and, then, continuity on the interface between regions is imposed in weak form by Nitsche's method.

The proposed strategies robustly refine the discretization as cracks propagate and can be easily incorporated into a working code for phase-field models. However, the computational cost can be further reduced by transitioning to the discontinuous in the combined model. In the wake of crack tips, the phase-field diffuse cracks are

replaced by XFEM discontinuous cracks and elements are derefined. The combined model is studied within the adaptive CG formulation. Numerical experiments include branching and coalescence of cracks, and a fully 3D test.

Acknowledgments

First and foremost, I would like to thank my supervisors, Sonia Fernández and Antonio Rodríguez, for their guidance and dedication. Thank you for being always supportive and making everything easier, with optimism and contagious motivation. I truly value your advice and the opportunities you have given me.

I am grateful to all my colleagues at LaCàN, I have learned from all of them. Especially, I want to thank Jordi, with whom I have shared all the ups and downs of this PhD experience. Many thanks also to Onofre for his patience and generosity.

Finally, I would like to thank my family and my friends for their unconditional encouragement during these years, for celebrating my successes and remedying bad days.

Contents

List of Figures

Chapter 1

Introduction

Fracture is a complex phenomenon that plays a fundamental role in many processes across various fields. In structural and mechanical engineering, fracture is typically viewed in a negative light and thought of as material failure. In many applications –such as rock quarry mining and hydraulic fracturing–, a controlled fracture is a key ingredient for success. Fracture also plays a crucial role in some natural events, such as egg hatching.

The ultimate goal of fracture mechanics is to understand and predict fracture inception and propagation, with the aim of avoiding, stopping and mitigating cracks, or promoting and controlling them, depending on the particular application.

The advances in computational mechanics have established numerical simulations as a reliable tool to complement experimental analysis of fracture. Current limitations include the high computational cost of these simulations. This thesis is devoted to the development of an efficient strategy for computational modelling of crack propagation in brittle or quasi-brittle materials, through the combination of classical approaches for fracture and advanced discretization methods.

1.1 Modelling of fracture, a brief overview

Classical approaches to model crack propagation can be classified into discontinuous and continuous models, depending on the way cracks are described. In discontinuous models, cracks are represented as discontinuities in the displacement field (*sharp*

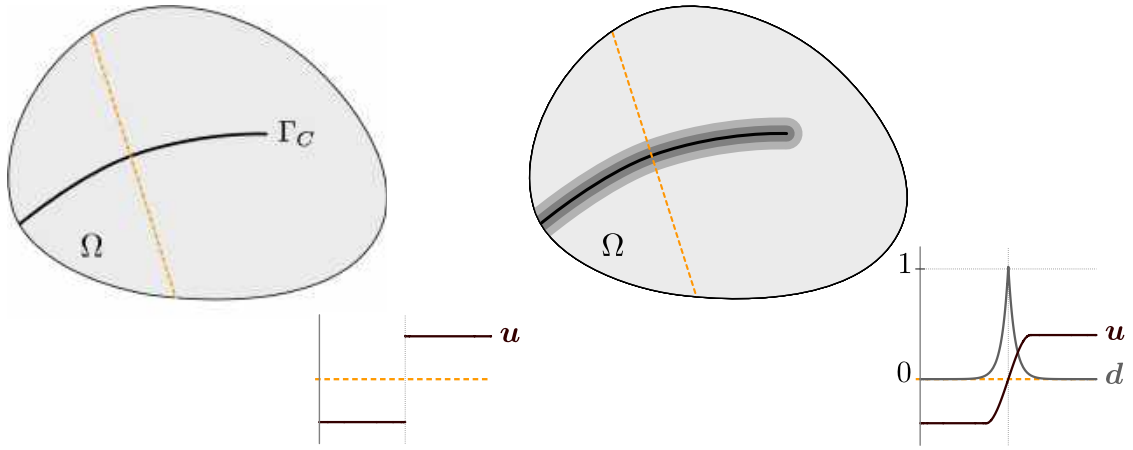

Figure 1.1: Body with a sharp crack Γ_C (left) and a diffuse phase-field representation of the crack with damage variable d (right).

cracks). On the contrary, continuous models, usually phase-field or gradient-damage models, assume continuous displacement fields and represent cracks as damaged regions that have lost their load-carrying capacity (*diffuse cracks*). Figure 1.1 sketches the two representations for the same cracked body in a domain Ω. The profile of the displacement field along the dotted section shows how the discontinuity from the sharp crack is approximated by a continuous function with a steep variation in phase-field models.

The thesis is focused on phase-field models, but the ideas and techniques are easily extendable to gradient-damage due to their common features. Throughout this work, the bulk is modelled as a continuum with small strain kinematics, and sharp cracks are traction-free. The term crack tips is used to refer both to crack tips, in 2D, and to crack fronts, in 3D.

1.1.1 Discontinuous models

Discontinuous models are characterized by discontinuous displacement fields across cracks. Also, it can be analytically shown that in linear elastic models stresses around crack tips vary according to $r^{-1/2}$, where r is the distance to the crack tip, see for instance the analysis by Sun and Jin [2012]. This singularity is physically unrealistic. Numerical techniques need to account for the discontinuities and for a proper approximation around crack tips, in order to guarantee the accuracy of the solution.

The standard Finite Element Method (FEM) requires a mesh fitted to the crack geometry to allow the discontinuity of displacements. This implies an update of the

mesh at every growth step of cracks. Remeshing as cracks propagate is computationally inefficient and has an impact on the accuracy because of the projection of the solution from one mesh to another. Moreover, the mesh has to be fine enough near the crack tip to properly approximate the singularity of the solution.

The most popular method for discontinuous models is the eXtended FEM (XFEM), which was first proposed by Belytschko and Black [1999], and later enhanced by Moës et al. [1999]. It is based on the Partition of the Unity Method (Melenk and Babuška [1996], Babuška and Melenk [1997]) and takes advantage of a priori knowledge of the solution. In XFEM, the discretization space is enriched with functions needed to represent the discontinuities and singularities in the solution and which cannot be spanned from the classical finite element shape functions, that is, discontinuous functions across every crack and near-tip asymptotic functions. Discontinuous functions are typically taken as Heavisides with values $+1$ and -1 on each side of the crack. The mesh does not need to be adapted to cracks and remeshing is avoided.

XFEM has demonstrated its applicability and computational efficiency in many applications, see for instance the reviews by Fries and Belytschko [2010] and Sukumar et al. [2015], but it presents some limitations for crack simulations.

From a practical point of view, the definition of a proper XFEM enrichment around crack tips is not straightforward. More precisely, to ensure convergence under uniform mesh refinement, the area where the crack-tip enrichment is applied should be kept fixed; but this strategy leads to severe ill-conditioning. On other hand, if the area for the crack-tip enrichment is reduced with the element size, asymptotic convergence cannot be observed, as studied by Laborde et al. [2005]. Some modifications of the method have been proposed to deal with these issues, including the modification of integration in elements with enriched nodes, also in Laborde et al. [2005], and the use of preconditioners, see Béchet et al. [2005]. An overview of the advances of the method to solve problems in fracture mechanics can be found in Sukumar et al. [2015].

Nevertheless, the main limitation of the discontinuous approach is that crack inception and propagation are not implicitly described by the governing equations for the bulk: the model is not complete until equipped with additional criteria. Different criteria have been proposed to determine the direction and velocity of propagation using local information of the solution at crack tips, see for instance Erdogan and Sih [1963], Sih [1974], Chang [1981], but a robust theory is not well-established yet. This is not the case for phase-field models, which handle crack evolution in a natural way.

1.1.2 Phase-field models

Phase-field models of brittle fracture were first proposed by Bourdin et al. [2000], as a regularization of the energetic formulation by Francfort and Marigo [1998]. Given the energy functional of the system, cracks are assumed to propagate along the path of least energy.

Cracks are represented by means of the so-called *phase-field variable* or *damage field*, which is denoted by d. The damage takes value 1 on the fracture path, value 0 in intact parts of the material and smoothly varies between the two values, as plotted in Figure 1.1. The damage field is introduced as an additional unknown into the system of equations. Thus, evolution of cracks is determined by the model itself.

The width of the diffuse cracks is regulated through a length-scale parameter l. Values of l are usually taken small in order to mimic sharp cracks. This implies steep variations for the displacement and the damage across cracks, and the need of very fine meshes along cracks to properly approximate the solution. The high computational cost associated to the demands in the spatial discretization is the main drawback of phase-field models.

In some problems, the crack path is known a priori, either exactly or approximately; consider, for instance, a straight crack in a symmetrical quasi-static configuration or a curved crack starting at a notch tip. In such scenarios, one may resort to a non-structured mesh with small elements along the expected crack path and larger elements in the rest of the domain. This is a rather common approach, see for instance Borden et al. [2012], Ambati et al. [2015] and Geelen et al. [2018]. On the contrary, if the crack path is not known beforehand, as for example happens in branching tests in dynamic fracture, or with complex crack patterns in heterogenous media, it is convenient to combine phase-field models with an automatic refinement strategy to modify the space of approximation as cracks propagate.

The computational cost also comes from solving the resulting system of equations for the displacement and the damage fields, which is nonlinearly coupled. The system is usually solved within a staggered scheme, in which the equations are alternately solved until convergence. In practice, many iterations are needed to converge at each load step. The alternative is solving the system with a monolithic scheme, but this is not straightforward since the Jacobian of the system is indefinite. Even though some modifications to the Newton's method have been explored, see the proposals by Gerasimov and De Lorenzis [2016] and Heister et al. [2015], the staggered approach

is still the common choice due to its simplicity and robustness.

It is also worth mentioning that phase-field models are not able to explicitly describe material separation within damage bands, leading to the transmission of spurious forces across cracks. This is also an inconvenience for some applications that need to model crack-surface physics, such as in hydraulic fracturing processes. This issue is tackled in continuous-discontinuous failure models, commented in next section.

For an extense and detailed review on the advances of phase-field models, we refer to the excellent work by Wu et al. [2019]. Also, Ambati et al. [2015] present a compilation of variations in the formulation, both from the physics and the mechanics communities.

1.1.3 Continuous-discontinuous models

The idea behind phase-field models with transition to fracture is to combine a discontinuous and a phase-field model; the first one to explicitly describe cracks and the second one to determine propagation. Some recent works in this line are the ones by Tamayo-Mas and Rodríguez-Ferran [2015] and Geelen et al. [2018].

The strategy followed by these models can be summarised as:

i. Solving with a phase-field model (background model) in the whole domain.

ii. Transitioning from the diffuse cracks to a sharp representation if a switching criterion is satisfied. This includes locating the crack path in the damaged zone and introducing the sharp crack in the discretization via XFEM.

iii. Applying a load increment and starting all over with the new discretization.

In these models, both descriptions of cracks (continuous and discontinuous) are overlapped. Critical issues are related to the introduction of discontinuities: when and where (switching and locating criteria, respectively). The introduction of sharp cracks in the bulk explicitly models material opening. However, they still have a high computational cost that comes from solving the phase-field equations in the whole domain with a properly refined mesh. Also, when introducing the sharp discontinuity within the diffuse crack, the discontinuity still keeps a region with $d \simeq 1$ around it, which may cause an extra weakening of the material.

1.2 Motivation and demands for a combined computational model

The advantages for fracture simulation of discontinuous and phase-field models are complementary. On the one hand, discontinuous models lack a rigorous theory to describe crack propagation on crack tips, but permit a coarse approximation of the crack on its wake. On the other hand, phase-field models contain information on the crack evolution but need a very fine mesh along the whole crack, implying a high computational cost.

This thesis proposes a combined model, with a phase-field approximation only in small subodmains around crack tips, and a discontinuous approximation in the rest of the domain, inheriting the main advantages of both approaches. The fine mesh is only needed in the crack-tip subdomains, focusing the computational efforts only where phase-field is used to determine propagation, and cracks are explicitly described via XFEM elsewhere, where no evolution of cracks is expected. The idea of the model is sketched in Figure 1.2.

Using XFEM in the discontinuous region and an automatic refinement strategy in phase-field subdomains, the mesh does not need to be adapted to the crack geometry and it can be fixed during all the simulation.

Notice that in order to avoid the disadvantages of continuous-discontinuous models, sharp and diffuse descriptions of cracks are not overlapped. Instead, the diffuse band is replaced by its sharp approximation far enough from crack tips. The critical issue is gluing of the two approximations on the interface between the phase-field and the discontinuous subdomains, with a non-conformal discretization and different representations of the crack (sharp and diffuse) in each part.

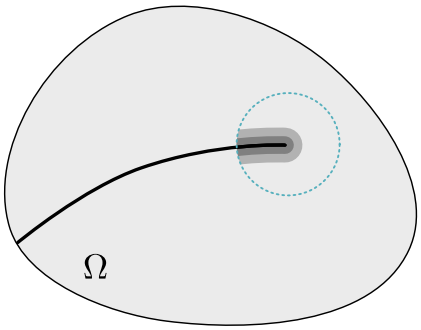

Figure 1.2: In the combined model, cracks are approximated as sharp cracks with diffuse crack tips.

The essentials in our proposal are:

- a combined model driving crack propagation and with explicit crack opening in almost the whole domain,
- the robustness of the method to cover a wide range of scenarios in brittle fracture while ensuring accuracy, both in 2D and 3D, and accounting for rapid crack growth,
- a very local refinement inside crack-tip subdomains, with neither remeshing nor spreading of refinement from the finer to the coarser parts of the discretization, in order to reduce the computational cost to the minimum,
- an automatic update of the crack-tip subdomains as cracks propagate, refining elements in the nose of crack tips and derefining them in its wake,
- the imposition of continuity in weak form on the interface between subdomains, to naturally handle the non-conformal approximations without having to deal with hanging nodes,
- no additional variables in the formulation, solving only for the damage and the displacement fields, and
- a simple implementation by reducing to only two types of elements (refined and standard) in a fixed background mesh, exploiting the characteristics of the problem to determine the refinement factor needed and the update of the crack-tip subdomains.

1.3 State of the art on adaptive refinement in phase-field models

In this section, we give an overview of the proposals in the literature which aim to efficiently simulate fracture by using a phase-field model to drive the propagation. Taking into account that fracture is an extremely localized process, adaptive refinement is important when the crack path is not known in advance, especially in 3D simulations. All proposals are based on updating the discretization as cracks evolve, to obtain more accuracy along cracks, where the solution is more demanding.

First, we review adaptive refinement strategies for phase-field –which refine the discretization along cracks and use a coarser discretization elsewhere– and, then, the recent combined XFEM phase-field approaches –which use a phase-field model to determine the propagation only in small subdomains containing crack tips, together with an XFEM approximation of cracks.

1.3.1 Adaptive phase-field models

Some authors opt for automatic remeshing as cracks propagate. For instance, Areias et al. [2016] propose a local remeshing technique, in which elements near cracks are divided and nodes are then relocated, and Burke et al. [2010] follow a node bisection method to divide elements while guaranteeing conformal meshes. These approaches modify the mesh according to the evolution of cracks, overcoming the limitations of using a globally refined mesh. However, remeshing still has a high computational cost.

In classical *hp*-refinement in FEM, elements to be refined are replaced by smaller elements, which may lead to non-conformal approximations. Dealing with hanging nodes complicates the implementation, specially for arbitrary refinement factors and for 3D problems, since hanging nodes have to be properly constrained to ensure continuity of the numerical solution. Heister et al. [2015] rely on the popular deal.II FEM library to define a strategy for *h*-adaptivity in phase-field simulations in 2D. The current implementation of this library is limited to one hanging node per element side and, therefore, to reach the desired element size in the refined region, the refinement spreads from the finest to the coarsest elements. The same approach is extended to 3D by Lee et al. [2016].

Proposals focused on simplifying the treatment of non-conformal approximations between refined and nonrefined regions may be classified into two categories, depending on whether the continuity on the interface between regions is imposed in strong form or in weak form.

Within the category of strong form continuity, Nagaraja et al. [2019] use the multi-level *hp*-FEM to dynamically refine the discretization around cracks with a fixed background mesh. Elements near cracks are refined by the superposition of a finer mesh. As many layers as needed can be superposed until the desired refinement is achieved, and the final approximation is the sum of all coarse and fine approximations. The mesh is *h*-refined up to a fixed depth, with an element size grading from the

coarsest to the finest parts of the mesh. This multi-level refinement relies on the use of regular grids; to handle irregular boundaries, it is combined with the Finite Cell Method, an immersed boundary approach. The strategy is implemented and tested in 2D.

Patil et al. [2018a] propose a refinement technique which is based on the Multiscale FEM (MsFEM). Elements near cracks are h-refined with a uniform submesh. To couple refined and nonrefined degrees of freedom on the non-conformal interface, they use multiscale basis functions, which are numerically constructed as a preprocess by solving boundary value problems at elemental level. The approach is applied in 2D, obtaining a very local refinement near cracks, but only for linear approximations. A drawback of MsFEM is the need of oversampling to avoid oscillations and guarantee an acceptable accuracy, see Hou and Wu [1997]. Moreover, the accuracy of the method is very sensitive to the chosen boundary conditions for the local problems, see Zhang et al. [2010].

Also motivated by the cumbersome implementation of hanging nodes in FEM, Shao et al. [2019] exploit the element-free Galerkin (EFG) method for h-adaptivity in 2D. In Shao et al. [2020], the same authors extend the approach to phase-field problems in 3D. EFG is a mesh-free method that depends on scattered nodes that can be freely added. As simulations evolve, nodes are added in a gradual distribution from dense regions to the sparse ones, spreading the refinement. However, the main drawback of EFG is its high computational cost when compared to FEM.

There have also been some proposals in the framework of isogeometric analysis by Hennig et al. [2016, 2018]. In these works, they assume one hanging node per element side, with the corresponding spreading of refinement.

Finally, Geelen et al. [2020] propose a global-local formulation. The solution is approximated with a global problem, modelling the structural response of the piece with a coarse mesh, and with a local problem, that models crack evolution and is discretized with a finer mesh. To couple the two approximations, the local solution is used to enrich the space of approximation for the global problem using numerically constructed functions, following the global-local Generalized FEM approach by Duarte et al. [2007], and the global solution is set as the Dirichlet value for the local problem. The strategy is successfully applied to 2D and 3D.

On the other hand, dealing with non-conformal approximations can be naturally tackled by imposing continuity in weak form between refined and nonrefined regions.

The resulting discretizations are very locally refined in narrow bands along cracks; no gradation of the element size or refinement level is needed and there is no spreading of refinement. This is the case in the global-local approach by Noii et al. [2020]. They define two domains corresponding to refined and nonrefined regions, covered with two independent meshes, and then weakly impose continuity between them by means of Lagrange multipliers, which are added as new unknowns to the system.

1.3.2 Combined XFEM phase-field models

Recent approches consider a phase-field model only in moving subdomains containing crack tips in combination with an XFEM representation of cracks, in order to improve the efficiency of the simulations.

Giovanardi et al. [2017] propose a two-scale strategy. A global solution for the displacement field is obtained with XFEM in the whole domain. Then, propagation is determined by solving a phase-field problem in subdomains containing the crack tips with a finer mesh, with Dirichlet boundary conditions approximated by the global solution. The strategy needs to iterate between the global and the local problem. Notice that using an XFEM discretization in the whole domain requires crack-tip enrichment to ensure accuracy, which is not straightforward. Numerical examples involve only one propagating crack.

Patil et al. [2018b] present a similar approach: cracks are described by an XFEM discretization in the whole domain, and a phase-field approximation is used in small circular subdomains around crack tips to determine propagation. The definition of the subdomains is based on the background mesh. Elements in the crack-tip regions and near the XFEM discretization are uniformly h-refined. Following the adaptive strategy in Patil et al. [2018a], the degrees of freedom in the transition between refined and nonrefined regions are glued via MsFEM. The strategy is successfully applied to simple cases of branching and coalescence of cracks.

The proposal in this thesis also exploits a combined XFEM phase-field model with sharp and diffuse representations of cracks. Differently to the above-mentioned strategies, in our approach the two representations are non-overlapped: the phase-field model is used in small crack-tip subdomains, while the XFEM representation is used in the rest of the domain. With the same philosophy as in Patil et al. [2018b], the strategy is based on a fixed background mesh. However, in our proposal only elements in the crack-tip subdomains are h-refined, while elements in the wake of

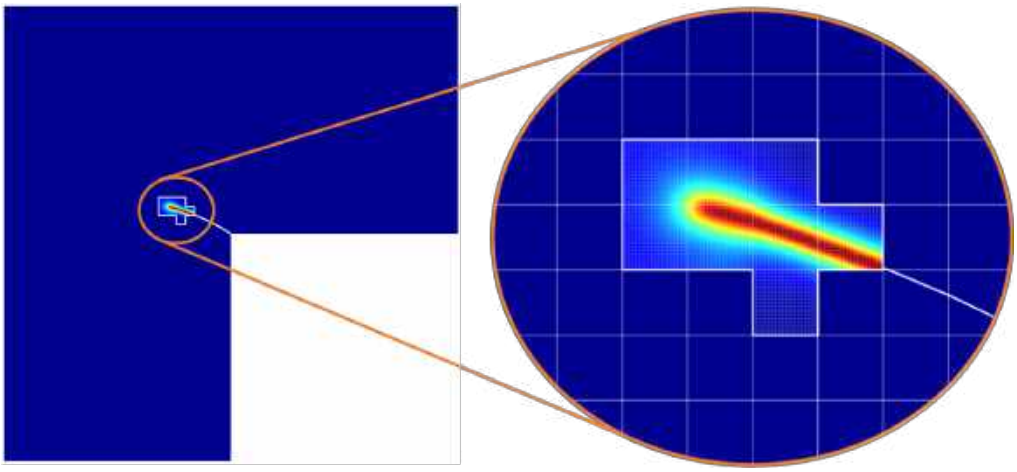

Figure 1.3: Discretization for the L-shaped panel test in Section 4.6.2, at imposed displacement $u_D = 0.26$ mm. Elements near the crack tip are refined with a submesh of 20×20 elements to capture the phase-field solution. The diffuse phase-field crack is replaced by a sharp XFEM crack in the wake of the tip.

crack tips are derefined with an inexpensive XFEM representation of the crack path. The crack-tip subdomains do not have to be circular thanks to the definition of proper boundary conditions for the damage field. This flexibility enables to define the crack-tip regions as the elements close to crack-tips and that reach some threshold for the damage, leading to an extremely localized refinement, see an example in Figure 1.3. Continuity of displacements between regions is imposed in weak form to easily account for the non-conformal discretizations.

It is also worth mentioning that in the previous proposals, the crack-tip regions are not updated within one load step, this is, cracks are assumed to stay inside these regions. With this assumption, it is not possible to capture brutal crack growth, which is typical in brittle fracture.

Finally, to the author's best knowledge, combined XFEM phase-field models have not been extended to 3D previously to this thesis.

1.4 Goals and layout of this thesis

The ultimate goal of this thesis is the efficient simulation of crack propagation with a combined XFEM phase-field computational model, as described in Section 1.2. An important requirement to ensure efficiency is the use of the same computational mesh during all the simulation, to avoid remeshing as cracks propagate. Thus, the steps to

achieve this goal are:

1. **The development of an adaptive refinement strategy for phase-field models,** to automatically h-refine the elements along cracks as they propagate.

   Two formulations are proposed in this thesis, which are based on an element-by-element local refinement, without remeshing, spreading of refinement nor additional unknown fields. A key ingredient in the strategies is the use of a fixed refinement factor, which is known a priori depending on the length-scale parameter l in the phase-field model. Then, only two types of elements are considered: standard and refined. Refined elements are mapped to a refined reference element, which is uniformly split into subelements. Continuity between elements of different type is imposed in weak form, thus the formulations naturally handle the non-conformal discretizations. The peculiarities of the problem are exploited to simplify the implementation, reducing to the minimum the number of cases to consider and enabling to easily integrate the refinement into a working code for phase-field. The very local and non-conformal h-refinement is illustrated in Figure 1.4.

   Chapter 2 describes the first strategy. It is based on a Hybridizable Discontinuous Galerkin (HDG) formulation of the problem, and takes advantage of HDG being a DG method that enables to use different approximation functions in neighboring elements.

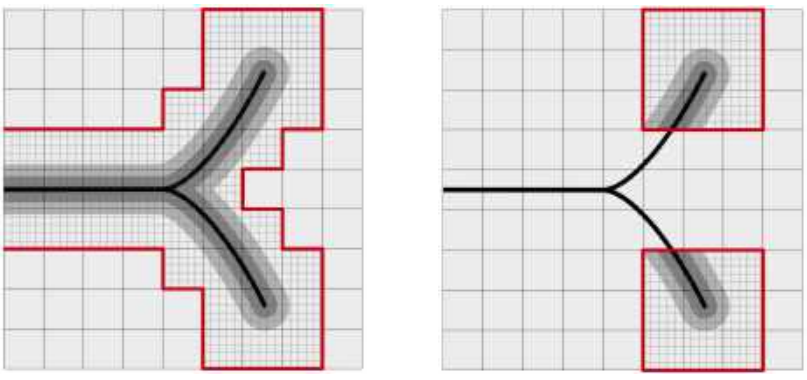

Figure 1.4: In the adaptive strategies, the discretization has h-refined elements along cracks and standard elements in the rest of the domain (left). In the combined model, refined elements are only used in subdomains around crack-tips, and the diffuse band is replaced by a sharp crack in the wake of crack tips (right).

Chapter 3 is devoted to adaptive refinement using Nitsche's method with continuous FE approximations. The strategy presents common features with the first proposal, but within a continuous FEM formulation, which is the usual choice in the fracture mechanics community.

2. **The transition to fracture in the adaptive phase-field model,** replacing diffuse cracks by sharp discontinuities via XFEM in the wake of crack tips.

   The proposed automatic adaptive refinements robustly refine the discretization in phase-field simulations. The weaknesses of the strategies are the inability of phase-field to explicitly describe crack opening and, more importantly, the reduced but still important computational cost associated to the refinement in all elements along the crack path. Thus, the next natural step is derefining the elements in the wake of the crack tips and replacing the diffuse band by a sharp crack by means of an XFEM coarser approximation, as sketched in Figure 1.4.

   A combined computational model with XFEM and phase-field is presented in Chapter 4. The coupling of the two subdomains follows the refinement formulation in Chapter 3. The combined model implies a substantial reduction in the number of degrees of freedom when compared to plain phase-field refinement.

All the numerical techniques in the thesis are implemented in Matlab.

1.5 Governing equations

This section recalls the governing equations for the discontinuous and the phase-field models of brittle fracture. We focus on the quasi-static regime: simulations are performed with incremental load steps, this is, evolution is driven by incremental boundary conditions.

As a representative phase-field model, we use the hybrid phase-field model by Ambati et al. [2015]. In this section, the derivation of the classical phase-field model and the special considerations in the hybrid model are discussed. Choosing a different phase-field model (in quasi-static or dynamic fracture) would not imply any changes in the proposed strategies in the thesis, since they are based on common features of all phase-field models.

We consider a linear elastic body with a traction-free crack, occupying a domain $\Omega \subset \mathbb{R}^{n_{sd}}$, with $n_{sd} = 2, 3$, and under the assumption of small deformations, as illustrated in Figure 1.1. We restrict ourselves to linear isotropic materials.

1.5.1 Discontinuous model

If no body forces are applied and inertia effects are neglected, the balance of linear momentum for the body in Ω leads to the system

$$\begin{cases} \boldsymbol{\nabla} \cdot \boldsymbol{\sigma} = \mathbf{0} & \text{in } \Omega \setminus \Gamma_C, \quad (1.1a) \\ \boldsymbol{u} = \boldsymbol{u}_D & \text{on } \Gamma_D, \quad (1.1b) \\ \boldsymbol{\sigma} \cdot \boldsymbol{n} = \boldsymbol{t}_N & \text{on } \Gamma_N, \quad (1.1c) \\ \boldsymbol{\sigma} \cdot \boldsymbol{n} = \mathbf{0} & \text{on } \Gamma_C^+ \cup \Gamma_C^-. \quad (1.1d) \end{cases}$$

The relation between the displacement field $\boldsymbol{u}$ and the stress tensor $\boldsymbol{\sigma}$ is given by the constitutive equation

$$\boldsymbol{\sigma} = \frac{\partial \Psi_0(\boldsymbol{\varepsilon})}{\partial \boldsymbol{\varepsilon}}, \tag{1.2}$$

where $\boldsymbol{\varepsilon}$ is the small strain tensor, defined as $\boldsymbol{\varepsilon}(\boldsymbol{u}) = \left(\boldsymbol{\nabla u} + (\boldsymbol{\nabla u})^T\right)/2$, and Ψ_0 is the elastic energy density. For linear isotropic materials, $\Psi_0 = (\boldsymbol{\varepsilon} : \boldsymbol{C} : \boldsymbol{\varepsilon})/2$ and $\boldsymbol{\sigma} = \boldsymbol{C} : \boldsymbol{\varepsilon}$, with $\boldsymbol{C}$ a fourth order positive definite tensor depending on the Lamé parameters. The Dirichlet and Neumann boundaries are denoted by Γ_D and Γ_N, respectively, and satisfy $\Gamma_D \cup \Gamma_N = \partial\Omega$ and $\Gamma_D \cap \Gamma_N = \emptyset$. Prescribed displacements and tractions are $\boldsymbol{u}_D$ and $\boldsymbol{t}_N$, and $\boldsymbol{n}$ is the exterior unit normal. Equation (1.1d) imposes traction-free conditions on the crack faces, denoted by Γ_C^+ and Γ_C^-.

1.5.2 Phase-field model

Energetic derivation of phase-field equations

Phase-field equations are obtained by the minimization of a regularized functional for the total energy of the system.

Following Francfort and Marigo [1998], the total energy of the body can be expressed as the sum of the bulk elastic energy and the crack surface energy, this is,

$$E(\boldsymbol{u}, \Gamma_C) = \int_\Omega \Psi_0(\boldsymbol{\varepsilon}) \, \mathrm{d}V + G_C \int_{\Gamma_C} \mathrm{d}s, \tag{1.3}$$

with G_C the critical energy release rate. Minimization of the energy functional (1.3) determines the fracture process.

To enable the numerical treatment of (1.3), Bourdin et al. [2000] regularized the formulation by introducing the damage field d, smearing the representation of the crack, see Figure 1.1 (right). Recall that the phase-field d has value 0 at intact points of the material and 1 at fully damaged points, and varies smoothly between both values. The energy functional is approximated by

$$E_l(\boldsymbol{u}, d) = \int_\Omega g(d)\Psi_0(\boldsymbol{\varepsilon}) \, \mathrm{d}V + G_C \int_\Omega \left(\frac{d^2}{2l} + \frac{l}{2}|\boldsymbol{\nabla} d|^2 \right) \, \mathrm{d}V, \tag{1.4}$$

where l is a length-scale parameter regulating the width of the diffuse crack and is typically chosen small to approximate the behavior of sharp cracks. Thus, the value of l determines the spatial discretization needed to resolve the cracks. The function $g(d)$ is called the *degradation function* and here is taken as

$$g(d) = (1 - d)^2. \tag{1.5}$$

Adding a small dimensionless parameter η to $g(d)$ was a common practice in the first phase-field models in order to prevent a complete loss of stiffness in cracked regions. However, according to our numerical experience and some other recent works, see for instance Geelen et al. [2019], Lo et al. [2019] and Wu et al. [2019], no artificial stiffness is needed in practice.

The regularized formulation (1.4) Γ-converges to the original (1.3) as l tends to zero, as proved by Bourdin et al. [2008].

Minimizing the regularized functional in (1.4) we obtain the governing equations

$$\begin{cases} \boldsymbol{\nabla} \cdot \boldsymbol{\sigma} = \boldsymbol{0}, \\ -l^2 \Delta d + d = \dfrac{2l}{G_C}(1 - d)\Psi_0, \end{cases} \tag{1.6}$$

with the stress tensor $\boldsymbol{\sigma}$ defined as

$$\boldsymbol{\sigma}(\boldsymbol{u}, d) = g(d) \frac{\partial \Psi_0(\boldsymbol{\varepsilon})}{\partial \boldsymbol{\varepsilon}} = g(d) \, \boldsymbol{C} : \boldsymbol{\varepsilon}(\boldsymbol{u}). \tag{1.7}$$

The stress tensor is degraded by the function $g(d)$. In fully broken parts of the material, where $d = 1$, this implies a complete loss of stiffness. In parts of the material with $d = 0$, the linear elastic stress-strain constitutive relation (1.2) is recovered.

This formulation does not distinguish between tension and compression, and unphysical cracks under compression can appear, as observed by Bourdin et al. [2000].

To remedy this issue, Miehe et al. [2010a,b] proposed a splitting of the elastic energy density into its tensile and compressive components, Ψ_0^+ and Ψ_0^-, based on the spectral decomposition of the strain tensor. More specifically, denoting by $\{\varepsilon_i\}_{i=1,\dots,n_{sd}}$ the principal strains and by $\{\boldsymbol{d}_i\}_{i=1,\dots,n_{sd}}$ the principal strain directions,

$$\Psi_0^{\pm}(\boldsymbol{\varepsilon}) = \frac{1}{2}\lambda\langle \mathrm{tr}(\boldsymbol{\varepsilon})\rangle_{\pm}^2 + \mu \mathrm{tr}\left(\boldsymbol{\varepsilon}_{\pm}^2\right), \tag{1.8}$$

where $\boldsymbol{\varepsilon}_{\pm} = \sum_{i=1}^{n_{sd}} \langle\varepsilon_i\rangle_{\pm} \boldsymbol{d}_i \otimes \boldsymbol{d}_i$ and $\langle\odot\rangle_{\pm} = (\odot \pm |\odot|)/2$. The total energy functional is then redefined to allow only the degradation of the tensile energy Ψ_0^+,

$$E_l(\boldsymbol{u}, d) = \int_\Omega \left(g(d)\Psi_0^+(\boldsymbol{\varepsilon}) + \Psi_0^-\right) \mathrm{d}V + G_C \int_\Omega \left(\frac{d^2}{2l} + \frac{l}{2}|\boldsymbol{\nabla} d|^2\right) \mathrm{d}V. \tag{1.9}$$

The stress-strain constitutive equation obtained in this case is

$$\boldsymbol{\sigma}(\boldsymbol{u}, d) = g(d)\frac{\partial \Psi_0^+(\boldsymbol{\varepsilon})}{\partial \boldsymbol{\varepsilon}} + \frac{\partial \Psi_0^-(\boldsymbol{\varepsilon})}{\partial \boldsymbol{\varepsilon}}, \tag{1.10}$$

and the equation governing the phase-field evolution becomes

$$-l^2\Delta d + d = \frac{2l}{G_C}(1-d)\Psi_0^+. \tag{1.11}$$

Notice in (1.11) that the phase-field variable only evolves due to tensile elastic energy, avoiding damage in compression. Also, keeping Ψ_0^- undegraded in (1.10) prevents the interpenetration of faces in case of crack closure.

To enforce irreversibility of cracks, Miehe et al. [2010a,b] replace Ψ_0^+ in (1.11) by a history-field variable defined as

$$\mathcal{H}^+(\boldsymbol{x}, t) = \max_{\tau\in[0,t]} \Psi_0^+\left(\boldsymbol{\varepsilon}\left(\boldsymbol{x}, \tau\right)\right). \tag{1.12}$$

The system is solved in an incremental procedure. Given the solution at load step n, the solution at step $n+1$ is computed solving the system in (1.14) with boundary conditions

$$\begin{cases} \boldsymbol{\sigma}\cdot\boldsymbol{n} = \boldsymbol{t}_N^{n+1} & \text{on } \Gamma_N, \\ \boldsymbol{u} = \boldsymbol{u}_D^{n+1} & \text{on } \Gamma_D, \\ \boldsymbol{\nabla} d \cdot \boldsymbol{n} = 0 & \text{on } \partial\Omega, \end{cases} \tag{1.13}$$

where $\boldsymbol{t}_N^{n+1}$ and $\boldsymbol{u}_D^{n+1}$ are the prescribed tractions and displacements at load step $n+1$.

The presented phase-field model is based on *i)* a spectral decomposition of the strain energy into tensile and compressive parts, equation (1.8); *ii)* a quadratic energetic degradation function $g(d) = (1-d)^2$, first integral in equation (1.9); *iii)* a

quadratic geometric crack function $\alpha(d) = d^2/2l$, second integral in equation (1.9). Various alternative phase-field models, with different choices for these three ingredients, can be found in the literature, see for instance Ambati et al. [2015], Wu et al. [2019], Amor et al. [2009], Freddi and Royer-Carfagni [2010].

Computationally, the main advantage of the system (1.6) is that both equations are linear within a staggered approach, while in formulations with a tension-compression splitting, the equilibrium equation becomes nonlinear due to the splitting in (1.10). In order to preserve the linearity of the equilibrium equation and to inhibit cracking in compression, Ambati et al. [2015] proposed the so-called *hybrid phase-field model*, which is considered in all numerical examples in this thesis.

The hybrid phase-field model

The hybrid phase-field model by Ambati et al. [2015] is characterized by incorporating a tension-compression splitting, while maintaining a linear equilibrium equation within a staggered scheme to solve the system.

The system of equations to be solved for the body in Ω reads

$$\begin{cases} \boldsymbol{\nabla} \cdot \boldsymbol{\sigma} = \mathbf{0} \quad \text{with} \quad \boldsymbol{\sigma} = g(d) \dfrac{\partial \Psi_0(\boldsymbol{\varepsilon})}{\partial \boldsymbol{\varepsilon}}, & \text{(1.14a)} \\ -l^2 \Delta d + d = \dfrac{2l}{G_C}(1-d)\mathcal{H}^+, & \text{(1.14b)} \\ g(d) := \begin{cases} (1-d)^2 & \text{where} \quad \Psi_0^+ \geq \Psi_0^-, \\ 1 & \text{otherwise.} \end{cases} & \text{(1.14c)} \end{cases}$$

The idea is to degrade the whole elastic energy density in the stress-strain relation in (1.14a) and to introduce the tension-compression splitting only in the damage equation (1.14b). The splitting comes into play in the source term of (1.14b) through the history field $\mathcal{H}^+$. Considering only the tensile component in the source term ensures that cracks are caused only by tension.

The condition in equation (1.14c) complements the system to ensure no interpenetration of faces occurs under compression, restoring the original stiffness of the material when compression dominates over tension. This is actually an alternative to incorporating the splitting in equation (1.14a). In this way, we are able to keep a linear equilibrium equation in the staggered scheme.

Staggered scheme

At each load step, we solve the system using a staggered scheme. This is, we solve the equilibrium and the damage equations alternately until convergence. The condition in equation (1.14c) is checked in the elemental computations for the equilibrium equation, using the solution from the previous staggered iteration. As a stopping criterion, we require the relative error of the damage field d in the Euclidean norm to be lower than a fixed tolerance.

Chapter 2

An HDG phase-field model with adaptivity[1]

In this chapter, we introduce an adaptive strategy for phase-field models based on an element-by-element local refinement along crack paths, in the setting of a novel Discontinuous Galerkin (DG) formulation for the problem. DG formulations impose continuity of the solution between elements in weak form, which makes them suitable for adaptivity since they naturally handle having adjacent elements with different spaces of approximation.

The strategy exploits the fact that the refinement needed to capture the solution is known a priori from the length-scale parameter in the model. Thus, only two types of elements are considered in our approach: standard elements and refined elements. Each type of element is mapped to the corresponding reference element (standard or refined), and the original background mesh is kept fixed during all the simulation. The refined reference element is uniformly split into subelements, with the corresponding basis functions and integration points. This simplifies the implementation and reduces the computational cost of the adaptive process. Continuity of the displacement and damage fields between elements is imposed in weak form by the DG formulation, without refinement transition regions nor additional unknown fields.

Within the DG family, we choose a Hybridizable Discontinuous Galerkin (HDG) method, because they are significantly cheaper than other DG methods. The cost of

[1]This chapter is based on Muixí et al. [2020c].

HDG has been studied, for instance, by Kirby et al. [2012], Yakovlev et al. [2016], Giorgiani et al. [2013], Paipuri et al. [2018] and Kronbichler et al. [2019].

The adaptive strategy is tested with the hybrid phase-field model by Ambati et al. [2015], but it is also applicable to other models.

The chapter is structured as follows. First, a novel HDG formulation for phase-field models is developed in Section 2.1. The proposed adaptive strategy is discussed in detail in Section 2.2. Numerical examples in Section 2.3 demonstrate the applicability and robustness of the methodology, providing accurate solutions with a very localized refinement along cracks and no transition regions. The conclusions of Section 2.4 close the chapter.

2.1 HDG formulation

We propose an HDG formulation to solve the system of equations of the hybrid phase-field model in (1.14). Within a staggered approach to solve the system, we consider independent HDG formulations for the equilibrium and for the damage field equations. For the equilibrium equation, we choose the HDG formulation for linear elasticity proposed by Soon et al. [2009], adding the damage degradation function in the stress-strain constitutive equation. However, the proposed strategy could also be applied with alternative HDG formulations in the literature, such as the ones by Qiu et al. [2018] and Sevilla et al. [2018]. For the damage equation, we add the reaction term to the HDG formulation for diffusion by Cockburn et al. [2009]. In this section, we briefly recall both formulations and present the algorithm used to solve the coupled system (1.14).

The HDG formulation for phase-field models is numerically compared to the FEM formulation for a benchmark test in Appendix A. The comparison is done using the isotropic phase-field model by Bourdin et al. [2000], which differs from the hybrid model in not considering a tension-compression splitting.

In what follows, the domain Ω is covered by a finite element mesh with $\mathrm{n_{el}}$ disjoint elements K_i satisfying

$$\bar{\Omega} \subset \bigcup_{i=1}^{\mathrm{n_{el}}} \bar{K}_i, \;\; K_i \cap K_j = \emptyset \text{ for } i \neq j, \tag{2.1}$$

and the union of the $\mathrm{n_{fc}}$ faces Γ_f of the mesh is denoted as

$$\Gamma = \bigcup_{i=1}^{\mathrm{n_{el}}} \partial K_i = \bigcup_{f=1}^{\mathrm{n_{fc}}} \Gamma_f.$$

2.1.1 HDG for the equilibrium equation

Consider the equilibrium equation (1.14a) for a given damage field d. In the broken space of elements, the problem can be expressed as a set of local problems, one for each element, and some global equations on the skeleton of the mesh, Γ. Local problems state the equilibrium equation at each element K_i with Dirichlet boundary conditions, this is,

$$\begin{cases} \boldsymbol{\nabla} \cdot \boldsymbol{\sigma}(\boldsymbol{J}, d) = \boldsymbol{0} & \text{in } K_i, \quad (2.2a) \\ \boldsymbol{J} - \boldsymbol{\nabla} \boldsymbol{u} = \boldsymbol{0} & \text{in } K_i, \quad (2.2b) \\ \boldsymbol{u} = \hat{\boldsymbol{u}} & \text{on } \partial K_i, \quad (2.2c) \end{cases}$$

for $i = 1...\mathrm{n_{el}}$, with $\boldsymbol{\sigma}(\boldsymbol{J}, d) = g(d)\, \boldsymbol{C} : \frac{1}{2}(\boldsymbol{J} + \boldsymbol{J}^T)$. The new variable $\boldsymbol{J}$ is the gradient of $\boldsymbol{u}$, enabling to split the problem into a system of first order PDE, and $\hat{\boldsymbol{u}}$ is the trace of $\boldsymbol{u}$ on Γ, see Figure 2.1. Instead of introducing $\boldsymbol{J}$ as the mixed variable, one could use the strain tensor $\boldsymbol{\varepsilon}$; both formulations are equivalent as proved by Fu et al. [2015].

Given $\hat{\boldsymbol{u}}$, the local problems (2.2) can be solved to determine $\boldsymbol{u}$ and $\boldsymbol{J}$. Thus, the problem reduces to determining the trace variable $\hat{\boldsymbol{u}}$. This is done by solving the so-called global problem, which imposes equilibrium of tractions on faces and the

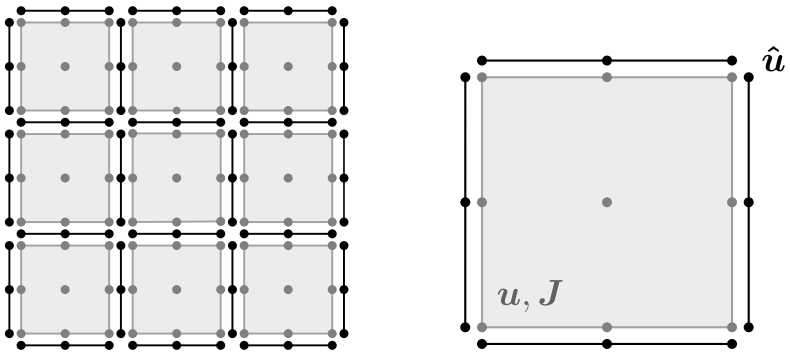

Figure 2.1: Left: HDG discretization of the domain, with the skeleton of the mesh in black. Right: HDG discretization for the local problem in one element.

boundary conditions, namely,

$$\begin{cases} [\![\boldsymbol{\sigma}\cdot\boldsymbol{n}]\!] = \boldsymbol{0} & \text{in } \Gamma\setminus\partial\Omega, \\ \boldsymbol{\sigma}\cdot\boldsymbol{n} = \boldsymbol{t}_N & \text{on } \Gamma_N, \\ \hat{\boldsymbol{u}} = \boldsymbol{u}_D & \text{on } \Gamma_D, \end{cases} \tag{2.3}$$

where $[\![\cdot]\!]$ stands for the jump operator defined at a face Γ_f as $[\![\odot]\!] = \odot_{L_f} + \odot_{R_f}$, with L_f and R_f the left and right elements sharing the face and $\odot_i$ the value of $\odot$ from element K_i. Notice that the continuity of $\boldsymbol{u}$ across Γ is imposed through the boundary condition $\boldsymbol{u} = \hat{\boldsymbol{u}}$ of the local problems, since $\hat{\boldsymbol{u}}$ is single-valued on faces.

The HDG formulation of the problem is obtained by discretizing the local and global problems. The discrete spaces considered to approximate the elemental variables, $\boldsymbol{u}$ and $\boldsymbol{J}$, and the trace variable, $\hat{\boldsymbol{u}}$, are

$$\begin{aligned} \mathcal{V}^h(\Omega) &= \{v \in L^2(\Omega) : v|_{K_i} \in \mathcal{P}^p(K_i) \text{ for } i = 1...\mathrm{n_{el}}\}, \\ \Lambda^h(\Gamma) &= \{\hat{v} \in L^2(\Gamma) : \hat{v}|_{\Gamma_f} \in \mathcal{P}^p(\Gamma_f) \text{ for } f = 1...\mathrm{n_{fc}}\}, \end{aligned} \tag{2.4}$$

where $\mathcal{P}^p$ denotes the space of polynomials of degree less or equal to p. To keep the notation simple, we use $\boldsymbol{u}$, $\boldsymbol{J}$ and $\hat{\boldsymbol{u}}$ to denote both the solutions and their approximations.

For an element K_i, the weak form for the local problem (2.2) is: given $\hat{\boldsymbol{u}} \in [\Lambda^h(\Gamma)]^{n_{sd}}$, find $\boldsymbol{u} \in [\mathcal{P}^p(K_i)]^{n_{sd}}$, $\boldsymbol{J} \in [\mathcal{P}^p(K_i)]^{n_{sd}\times n_{sd}}$ such that

$$\int_{K_i} \boldsymbol{v}\cdot(\boldsymbol{\nabla}\cdot\boldsymbol{\sigma}(\boldsymbol{J},d))\ \mathrm{d}V + \int_{\partial K_i} \tau\boldsymbol{v}\cdot\Big(\big(\boldsymbol{C} : [(\hat{\boldsymbol{u}}-\boldsymbol{u})\otimes\boldsymbol{n}]\big)\cdot\boldsymbol{n}\Big)\ \mathrm{d}s = 0, \tag{2.5a}$$

$$\int_{K_i} \boldsymbol{Q} : \boldsymbol{J}\ \mathrm{d}V + \int_{K_i} (\boldsymbol{\nabla}\cdot\boldsymbol{Q})\cdot\boldsymbol{u}\ \mathrm{d}V - \int_{\partial K_i} (\boldsymbol{Q}\cdot\boldsymbol{n})\cdot\hat{\boldsymbol{u}}\ \mathrm{d}s = 0, \tag{2.5b}$$

for all $\boldsymbol{v} \in [\mathcal{P}^p(K_i)]^{n_{sd}}$, for all $\boldsymbol{Q} \in [\mathcal{P}^p(K_i)]^{n_{sd}\times n_{sd}}$. Equation (2.5a) is derived from (2.2a) by applying integration by parts, replacing the numerical flux

$$\hat{\boldsymbol{\sigma}} := \boldsymbol{\sigma}(\boldsymbol{J},d) + \tau\ \boldsymbol{C} : \big((\hat{\boldsymbol{u}}-\boldsymbol{u})\otimes\boldsymbol{n}\big) \tag{2.6}$$

on the boundary and undoing the integration by parts. The parameter τ is a positive stabilization parameter, which we will take constant in all the domain. Equation (2.5b) is obtained by applying integration by parts on (2.2b) and replacing $\boldsymbol{u} = \hat{\boldsymbol{u}}$ on the element boundary.

The discretization of the local problem (2.5) leads to a system of the form

$$\begin{bmatrix} \boldsymbol{A}^i_{uu} & \boldsymbol{A}^i_{uJ} \\ \boldsymbol{A}^i_{Ju} & \boldsymbol{A}^i_{JJ} \end{bmatrix} \begin{bmatrix} \boldsymbol{u}^i \\ \boldsymbol{J}^i \end{bmatrix} = - \begin{bmatrix} \boldsymbol{A}^i_{u\hat{u}} \\ \boldsymbol{A}^i_{J\hat{u}} \end{bmatrix} \boldsymbol{\Lambda}^i, \tag{2.7}$$

which can be arranged as the *local solver* for each element K_i, expressing $\boldsymbol{u}$ and $\boldsymbol{J}$ in the element in terms of $\hat{\boldsymbol{u}}$,

$$\boldsymbol{u}^i = \mathbf{U}^{K_i}\boldsymbol{\Lambda}^i, \ \boldsymbol{J}^i = \mathbf{Q}^{K_i}\boldsymbol{\Lambda}^i, \tag{2.8}$$

with matrices $\mathbf{U}^{K_i}, \mathbf{Q}^{K_i}$. The vectors $\boldsymbol{u}^i$ and $\boldsymbol{J}^i$ are the vectors of nodal values of the element and $\boldsymbol{\Lambda}^i$ is the vector of nodal values of $\hat{\boldsymbol{u}}$ on the n_f faces of K_i,

$$\boldsymbol{\Lambda}^i := \begin{bmatrix} \hat{\boldsymbol{u}}^{F_{i,1}} \\ \vdots \\ \hat{\boldsymbol{u}}^{F_{i,n_f}} \end{bmatrix}. \tag{2.9}$$

For the global problem (2.3), replacing $\boldsymbol{\sigma}$ by the numerical flux $\hat{\boldsymbol{\sigma}}$, the weak form reads: find $\hat{\boldsymbol{u}} \in [\Lambda^h(\Gamma)]^{n_{sd}}$ such that $\hat{\boldsymbol{u}} = \mathbb{P}_2(\boldsymbol{u}_D)$ on Γ_D and

$$\int_\Gamma \hat{\boldsymbol{v}} \cdot [\![\hat{\boldsymbol{\sigma}} \cdot \boldsymbol{n}]\!] \ \mathrm{d}s + \int_{\Gamma_N} \hat{\boldsymbol{v}} \cdot (\hat{\boldsymbol{\sigma}} \cdot \boldsymbol{n}) \ \mathrm{d}s = \int_{\Gamma_N} \hat{\boldsymbol{v}} \cdot \boldsymbol{t}_N \ \mathrm{d}s, \tag{2.10}$$

for all $\hat{\boldsymbol{v}} \in [\Lambda^h(\Gamma)]^{n_{sd}}$ such that $\hat{\boldsymbol{v}} = \mathbf{0}$ on Γ_D, where $\mathbb{P}_2$ denotes the L^2 projection onto $[\Lambda^h(\Gamma)]^{n_{sd}}$. Discretizing the global weak form and replacing $\boldsymbol{u}$ and $\boldsymbol{J}$ in terms of $\hat{\boldsymbol{u}}$ by the local solver (2.8), a system for $\hat{\boldsymbol{u}}$ is obtained. Once $\hat{\boldsymbol{u}}$ is determined, $\boldsymbol{u}$ and $\boldsymbol{J}$ are computed for each element using the local solvers (2.8).

As proved by Fu et al. [2015], $\boldsymbol{u}$ converges with order $p+1$ in L^2 norm and $\boldsymbol{J}$ with order $p+1/2$, if an approximation of degree p is used. In a more recent formulation, Sevilla et al. [2018] report convergence of order $p+1$ for $\boldsymbol{J}$ based on numerical experiments.

It is important noting that solving the global system of equations only involves the trace variable $\hat{\boldsymbol{u}}$. Thus, the number of degrees of freedom and the computational efficiency are similar to the ones obtained with continuous finite elements with static condensation, see Kirby et al. [2012] for a comparison. Nevertheless, HDG provides a suitable framework for very local h-refinement without hanging nodes nor transition regions of refinement.

2.1.2 HDG for the damage equation

The HDG formulation for the damage field equation (1.14b), with a given source term $\mathcal{H}^+$, can be obtained following the same steps as for the equilibrium equation. Two new variables are defined: $\boldsymbol{q}$ as the gradient of d, and $\hat{d}$ as the trace of d on the

skeleton of the mesh. The local problems impose the equation in every element K_i with Dirichlet boundary conditions, and their weak form is: given $\hat{d} \in \Lambda^h(\Gamma)$, find $d \in \mathcal{P}^p(K_i)$, $\boldsymbol{q} \in [\mathcal{P}^p(K_i)]^{n_{sd}}$ such that

$$\begin{aligned} -\int_{K_i} G_C l\ v\boldsymbol{\nabla}\cdot\boldsymbol{q}\ \mathrm{d}V - \int_{\partial K_i} G_C l\tau\ (\hat{d}-d)v\ \mathrm{d}s + \int_{K_i}\left(\frac{G_C}{l}+2\mathcal{H}^+\right)vd\ \mathrm{d}V \\ = \int_{K_i} v2\mathcal{H}^+\ \mathrm{d}V, \qquad (2.11) \\ \int_{K_i}\boldsymbol{w}\cdot\boldsymbol{q}\ \mathrm{d}V + \int_{K_i}(\boldsymbol{\nabla}\cdot\boldsymbol{w})d\ \mathrm{d}V - \int_{\partial K_i}\boldsymbol{w}\cdot\boldsymbol{n}\ \hat{d}\ \mathrm{d}s = 0, \end{aligned}$$

for all $v \in \mathcal{P}^p(K_i)$, $\boldsymbol{w} \in [\mathcal{P}^p(K_i)]^{n_{sd}}$. In this case, the numerical flux on the boundary of every element is

$$\hat{\boldsymbol{q}} := \boldsymbol{q} + \tau(\hat{d}-d)\boldsymbol{n} \qquad (2.12)$$

with τ the stabilization parameter. Also in this case, the stabilization parameter can be any positive value, that here is taken constant in all Ω.

The weak form of the global problem is: find $\hat{d} \in \Lambda^h(\Gamma)$ such that

$$\int_{\Gamma\setminus\partial\Omega}\hat{v}\cdot[\![\hat{\boldsymbol{q}}\cdot\boldsymbol{n}]\!]\ \mathrm{d}s = 0, \qquad (2.13)$$

for all $\hat{v} \in \Lambda^h(\Gamma)$.

In this case, for degree of approximation p, both d and $\boldsymbol{q}$ converge with order $p+1$ in the L^2 norm. See Cockburn et al. [2009] for a proof for the Laplace equation.

Remark 1 (Postprocessed damage d^*)**.** A second element-by-element postprocess can be done to compute a superconvergent solution, d^*. At every element K_i, given $d \in \mathcal{P}^p(K_i)$ and $\boldsymbol{q} \in [\mathcal{P}^p(K_i)]^{n_{sd}}$, $d^* \in \mathcal{P}^{p+1}(K_i)$ can be computed as the solution of

$$\begin{aligned} &\int_{K_i}\boldsymbol{\nabla}d^*\cdot\boldsymbol{\nabla}v\ \mathrm{d}V = \int_{K_i}\boldsymbol{q}\cdot\boldsymbol{\nabla}v\ \mathrm{d}V \quad \forall v\in\mathcal{P}^{p+1}(K_i), \\ &\int_{K_i} d^*\ \mathrm{d}V = \int_{K_i} d\ \mathrm{d}V. \end{aligned} \qquad (2.14)$$

The postprocessed solution d^* converges with order $p+2$ in the L^2 norm and, since the problem is solved at element level, the computational cost is negligible. See Cockburn et al. [2012] for more details.

2.1.3 Staggered scheme

We solve the phase-field system of equations (1.14) by using a staggered scheme to decouple the system. Given the solution at load step n, the solution at load step $n+1$ is computed by solving alternately the equilibrium and phase-field equations until convergence is reached, see Algorithm 2.1.

Algorithm 2.1 Staggered scheme with HDG

Initialization
Take $d^{*,0}(\boldsymbol{x}) = 0$, $\mathcal{H}^{+,0}(\boldsymbol{x}) = 0$ for all $\boldsymbol{x}$ in Ω.
Loop in load steps
for each load step n **do**
Initialization
Define $[d^{*,n+1}]^0 = d^{*,n}$.
Loop in staggered iterations
for each staggered iteration i **do**

1. **Compute displacement field** $[\boldsymbol{u}^{n+1}]^{i+1}$ by solving the equilibrium equation

$$\boldsymbol{\nabla} \cdot \boldsymbol{\sigma}\left([\boldsymbol{u}^{n+1}]^{i+1}, [d^{*,n+1}]^{i}\right) = 0 \text{ in } \Omega,$$

with $\boldsymbol{\sigma} = ((1-d)^2 + \eta)\,\frac{\partial \Psi_0(\boldsymbol{\varepsilon})}{\partial \boldsymbol{\varepsilon}}$ and boundary conditions $\boldsymbol{\sigma} \cdot \boldsymbol{n} = \boldsymbol{t}^{n+1}$ on Γ_N, $[\boldsymbol{u}^{n+1}]^{i+1} = \boldsymbol{u}_D^{n+1}$ on Γ_D.

2. **Update the history field** $[\mathcal{H}^{+,n+1}]^{i+1} = \max\left(\mathcal{H}^{+,n}, \left[\Psi_0^{+,n+1}\right]^{i+1}\right)$.

3. **Compute damage field** $[d^{n+1}]^{i+1}$ by solving

$$-l^2 \Delta \left[d^{n+1}\right]^{i+1} + \left[d^{n+1}\right]^{i+1} = \frac{2l}{G_C}\left(1 - \left[d^{n+1}\right]^{i+1}\right)\left[\mathcal{H}^{+,n+1}\right]^{i+1} \text{ in } \Omega,$$

with boundary condition $\left(\nabla \left[d^{n+1}\right]^{i+1}\right) \cdot \boldsymbol{n} = 0$ on $\partial\Omega$.

4. **Compute postprocessed damage field** $[d^{*,n+1}]^{i+1}$ by solving the element-by-element problem (2.14).

5. **Stopping criterion.** If $\|[d^{*,n+1}]^{i+1} - [d^{*,n+1}]^{i}\|_2 < \text{tol}$, stop iterating and set

$$d^{*,n+1} := \left[d^{*,n+1}\right]^{i+1}, \; \mathcal{H}^{+,n+1} := \left[\mathcal{H}^{+,n+1}\right]^{i+1}$$

end for
end for

Remark 2 (Evaluation of $\mathcal{H}^+$)**.** In order to enable the convergence of the staggered scheme, special care has to be taken in the evaluation of the history field $\mathcal{H}^+$. This

field is computed using the nodal values of $\boldsymbol{J}$ obtained by solving the equilibrium equation. If $\mathcal{H}^+$ is evaluated at nodes, it may become negative when interpolated to integration points to solve the damage field equation if we use approximation functions of degree higher than 1. This may lead to unphysical solutions for d and to the non-convergence of the staggered scheme. See Appendix A for a numerical example of this behavior. To avoid negative values of $\mathcal{H}^+$ at integration points, we first interpolate $\boldsymbol{J}$ at integration points and then evaluate $\mathcal{H}^+$ at these points. It is also worth noting that the update of $\mathcal{H}^+$ in step 2 of Algorithm 2.1 is done using the value of the field at the previous load step, and not the previous staggered iteration, because the former is a converged solution with physical meaning. This can be seen from the definition of $\mathcal{H}^+$ in (1.12).

Remark 3 (Postprocessed displacement $\boldsymbol{u}^*$)**.** Analogously to the computation of the postprocessed damage d^*, it is possible to recover a postprocessed displacement $\boldsymbol{u}^*$ by solving an element-by-element problem, as detailed in Soon et al. [2009]. The postprocessed $\boldsymbol{u}^*$ converges with order $p+3/2$ in the L^2 norm when using approximation functions of degree p. In this case, since the history field $\mathcal{H}^+$ is computed using $\boldsymbol{J}$, we are not interested in computing $\boldsymbol{u}^*$ at every iteration. Once the staggered scheme has converged for a load step, the postprocessed $\boldsymbol{u}^*$ can be computed to have a better approximation for the displacements if desired.

2.2 Adaptive refinement strategy

The presented HDG formulation for phase-field can be exploited to implement an adaptive refinement strategy which is naturally handled by the method. Because HDG is a Discontinuous Galerkin method, different basis functions can be used to approximate the solution in adjacent elements. In particular, we can h-refine the elements along the crack, where more accuracy is needed to capture the solution, with no numerical treatment of the transition between refined and non-refined elements. Here, p-refinement is not considered because using significantly high degrees to approximate solutions with steep gradients may give oscillations. However, the ideas are extendable to p and $hp-$refinement.

We consider two types of element, *standard* and *refined*, and use different approximation spaces in each one of them. Here, no recursive refinements are contemplated, since the final element size required to capture the solution inside refined elements

is determined by the length-scale parameter l in the phase-field model. As a rule of thumb, the refinement factor m can be computed as

$$m = \left\lceil \frac{ah}{lp} \right\rceil, \tag{2.15}$$

where a is a positive scalar, h is the element size of the background mesh and p is the degree of approximation. In our experience, a reasonable value for a is between 3 and 5.

In standard elements, the approximation space is the standard one in FEM, this is, $\mathcal{P}^p$. In refined elements the space is h-refined: given the refinement factor m, we consider a uniform submesh of $m \times m$ subelements and we define the approximation space as the sum of the standard approximation spaces for all subelements. For an element K_i that is refined, its subelements are denoted as $K_{i,j}$ for $j = 1...m^2$. The faces Γ_f shared by two refined elements, as well as the boundary faces of refined elements, are also refined, meaning that they are divided in subfaces $\Gamma_{f,j}$ for $j = 1...m$. Faces belonging to standard elements are not refined, even the faces shared with a refined element, since we assume the face is far enough from the critical region near the crack, see Figure 2.2.

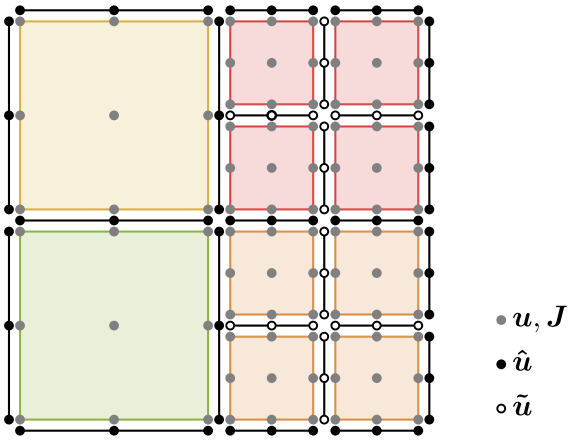

Figure 2.2: Example of an HDG discretization for the equilibrium equation for a mesh of 2×2 elements with 2 standard elements (left) and 2 refined elements (right). The global problem is solved for the degrees of freedom corresponding only to $\hat{\boldsymbol{u}}$ (black dots). Note that faces shared by a refined and a standard element are not refined.

Thus, the considered approximation spaces for the components of the primal variables $\boldsymbol{u}$, $\boldsymbol{J}$, d and the traces $\hat{\boldsymbol{u}}$, $\hat{d}$ are defined as

$$\begin{aligned}\mathcal{V}^h_{\text{ref}}(\Omega) &= \{v \in L^2(\Omega) : v|_{K_i} \in \mathcal{P}^p(K_i) \text{ for } i \in E_{\text{std}},\ v|_{K_i} \in \mathcal{P}^p_{\text{ref}}(K_i) \text{ for } i \in E_{\text{ref}}\},\\ \Lambda^h_{\text{ref}}(\Gamma) &= \{\hat{v} \in L^2(\Gamma) : \hat{v}|_{\Gamma_f} \in \mathcal{P}^p(\Gamma_f) \text{ for } f \in F_{\text{std}},\ \hat{v}|_{\Gamma_f} \in \mathcal{P}^p_{\text{ref}}(\Gamma_f) \text{ for } f \in F_{\text{ref}}\},\end{aligned} \tag{2.16}$$

where E_{std} and E_{ref} are the sets of standard and refined elements, F_{std} and F_{ref} are the sets of standard and refined faces, and the refined polynomial spaces are

$$\begin{aligned}\mathcal{P}^p_{\text{ref}}(K_i) &= \{v \in L^2(K_i) : v \in \mathcal{P}^p(K_{i,j}) \text{ for } j = 1...m^2\},\\ \mathcal{P}^p_{\text{ref}}(\Gamma_f) &= \{\hat{v} \in L^2(\Gamma_f) : \hat{v} \in \mathcal{P}^p(\Gamma_{f,j}) \text{ for } j = 1...m\}.\end{aligned} \tag{2.17}$$

From the implementation point of view, we define a reference element for each type of element: standard and refined. Standard elements are mapped to the standard reference element as usual. The elements selected to be refined are mapped to the refined reference element, which is actually the one divided in m^2 uniform subelements. This strategy extremely reduces the number of cases in the implementation.

Inside refined elements, we impose continuity of the solution between subelements in weak form. Keeping an HDG philosophy, we consider the inner skeleton in the element, namely

$$\mathcal{I}_i = \bigcup_{j=1}^{m^2} \partial K_{i,j} \setminus \partial K_i, \tag{2.18}$$

and define $\tilde{\boldsymbol{u}}$ and $\tilde{d}$ as the inner traces of the displacements $\boldsymbol{u}$ and the damage d, respectively, inside the element, see Figure 2.2. The local problem in refined elements is consequently modified using the refined local spaces for volume variables, side trace variables and interior trace variables, and accounting for the weak imposition of continuity between subelements. The local problems for standard elements and the global problems are the same as in standard HDG, accounting for the richer space in refined faces in the global problem.

Notice that our approach is equivalent to non-conformal h-refinement in standard HDG. We choose to state the formulation with a refined reference element in order to maintain the same structure of the code and to reduce the conditionals in the implementation to the minimum. Also, the resulting global system has less degrees of freedom, since the ones corresponding to inner traces are not incorporated into the system.

Remark 4 (Continuous vs discontinuous approximation in refined elements)**.** An alternative option would be to consider a piecewise polynomial continuous approximation in refined elements. However, with a mixed formulation as the ones in the local problems, it would require inner stabilization in the element, depending on a stabilization parameter whose tuning may not be straightforward, see Cervera et al. [2010]. The considered discontinuous subelement-by-subelement approximation inside refined elements provides a stable approximation for any positive value of the parameter τ, with additional degrees of freedom only at element-level computations.

In this section, we first formulate the local problem for refined elements for both the equilibrium and the damage equations. Then, we give some implementation details and show the convergence plots of the formulations for an analytical solution. To simplify the notation, throughout the section we denote as $\hat{K}_i$ the union of subelements $K_{i,j}$ and as $\partial\hat{K}_i$ the union of exterior faces of subelements.

2.2.1 Local problem for the equilibrium equation for refined elements

For the equilibrium equation, the strong from for the local problem for a refined element K_i is

$$\begin{cases} \boldsymbol{\nabla}\cdot\boldsymbol{\sigma}(\boldsymbol{J},d)=\mathbf{0} & \text{in } \hat{K}_i, \quad (2.19a)\\ \boldsymbol{J}-\boldsymbol{\nabla}\boldsymbol{u}=\mathbf{0} & \text{in } \hat{K}_i, \quad (2.19b)\\ [\![\boldsymbol{\sigma}\cdot\boldsymbol{n}]\!]=\mathbf{0} & \text{on } \mathcal{I}_i, \quad (2.19c)\\ \boldsymbol{u}=\tilde{\boldsymbol{u}}_i & \text{on } \mathcal{I}_i, \quad (2.19d)\\ \boldsymbol{u}=\hat{\boldsymbol{u}} & \text{on } \partial\hat{K}_i. \quad (2.19e) \end{cases}$$

The new variable $\tilde{\boldsymbol{u}}_i$ is the restriction of the displacement field $\boldsymbol{u}$ on the inner skeleton of the element, $\mathcal{I}_i$. The equilibrium equation on the inner skeleton (2.19c) has to be incorporated to the system because we are using a discontinuous approximation for the subelements. Continuity is imposed by the condition (2.19d).

The weak form of the problem reads: given $\hat{\boldsymbol{u}}\in[\Lambda^h_{\text{ref}}(\Gamma)]^{n_{sd}}$, find $\boldsymbol{u}\in[\mathcal{P}^p_{\text{ref}}(K_i)]^{n_{sd}}$,

$\boldsymbol{J} \in [\mathcal{P}^p_{\text{ref}}(K_i)]^{n_{sd}\times n_{sd}}$, $\tilde{\boldsymbol{u}}_i \in \left[\Lambda^h_{\text{ref}}(\mathcal{I}_i)\right]^{n_{sd}}$ such that

$$\begin{aligned}
&\int_{\hat{K}_i} \boldsymbol{v}\cdot(\boldsymbol{\nabla}\cdot\boldsymbol{\sigma}(\boldsymbol{J},d))\ \mathrm{d}V + \int_{\partial\hat{K}_i} \tau\boldsymbol{v}\cdot\Big((\boldsymbol{C}:[(\hat{\boldsymbol{u}}-\boldsymbol{u})\otimes\boldsymbol{n}])\cdot\boldsymbol{n}\Big)\ \mathrm{d}s + \\
&\qquad\qquad + \int_{\mathcal{I}_i} 2\tau\boldsymbol{v}\cdot\Big((\boldsymbol{C}:[(\tilde{\boldsymbol{u}}_i-\{\boldsymbol{u}\})\otimes\boldsymbol{n}])\cdot\boldsymbol{n}\Big)\ \mathrm{d}s = 0,\\
&\int_{\hat{K}_i} \boldsymbol{Q}:\boldsymbol{J}\ \mathrm{d}V + \int_{\hat{K}_i}(\boldsymbol{\nabla}\cdot\boldsymbol{Q})\cdot\boldsymbol{u}\ \mathrm{d}V - \int_{\partial\hat{K}_i}(\boldsymbol{Q}\cdot\boldsymbol{n})\cdot\hat{\boldsymbol{u}}\ \mathrm{d}s - \int_{\mathcal{I}_i}[\![\boldsymbol{Q}\cdot\boldsymbol{n}]\!]\cdot\tilde{\boldsymbol{u}}_i\ \mathrm{d}s = 0,\\
&\int_{\mathcal{I}_i}\tilde{\boldsymbol{v}}\cdot[\![\hat{\boldsymbol{\sigma}}\cdot\boldsymbol{n}]\!]\ \mathrm{d}s = 0,
\end{aligned} \tag{2.20}$$

for all $\boldsymbol{v} \in [\mathcal{P}^p_{\text{ref}}(K_i)]^{n_{sd}}$, for all $\boldsymbol{Q} \in [\mathcal{P}^P_{\text{ref}}(K_i)]^{n_{sd}\times n_{sd}}$, for all $\tilde{\boldsymbol{v}} \in [\Lambda^h_{\text{ref}}(\mathcal{I}_i)]^{n_{sd}}$. The mean operator is defined as $\{\odot\} = \frac{1}{2}\left(\odot_{L_f} + \odot_{R_f}\right)$, with L_f and R_f the left and right subelements sharing the face and $\odot_j$ the value of $\odot$ from subelement $K_{i,j}$.

The weak form is obtained substituting the numerical flux $\hat{\boldsymbol{\sigma}}$ defined in (2.6) in the integrals over $\partial\hat{K}_i$ and $\mathcal{I}_i$. In this case, the discretization of the weak from leads to a system of the form

$$\begin{bmatrix} \boldsymbol{A}^i_{uu} & \boldsymbol{A}^i_{uJ} & \boldsymbol{A}^i_{u\tilde{u}} \\ \boldsymbol{A}^i_{Ju} & \boldsymbol{A}^i_{JJ} & \boldsymbol{A}^i_{J\tilde{u}} \\ \boldsymbol{A}^i_{\tilde{u}u} & \boldsymbol{A}^i_{\tilde{u}J} & \boldsymbol{A}^i_{\tilde{u}\tilde{u}} \end{bmatrix} \begin{bmatrix} \boldsymbol{u}_i \\ \boldsymbol{J}_i \\ \tilde{\boldsymbol{u}}_i \end{bmatrix} = - \begin{bmatrix} \boldsymbol{A}^i_{u\hat{u}} \\ \boldsymbol{A}^i_{J\hat{u}} \\ \boldsymbol{0} \end{bmatrix} \boldsymbol{\Lambda}_i, \tag{2.21}$$

which gives a local solver for $\boldsymbol{u}$ and $\boldsymbol{J}$ in the element K_i with the same structure as (2.8). One can also obtain the local solver for the elemental variable $\tilde{\boldsymbol{u}}_i$. However, it is not used since it is an auxiliary variable in the local problem, not appearing in the global equations.

Eliminating the degrees of freedom corresponding to $\tilde{\boldsymbol{u}}_i$ from the global system clearly decreases the size of the matrix. However, the coupling between the remaining degrees of freedom increases, i.e., there are more non-zero entries per row. In fact, the resulting matrix has the same sparsity pattern as for a p-refinement. If compared to a standard element, the sparsity pattern is the same but with m times more degrees of freedom in each refined face. See an example in Section 2.2.5.

2.2.2 Local problem for the damage equation for refined elements

Defining $\tilde{d}_i$ as the inner trace of the damage d on $\mathcal{I}_i$, the strong form for the local problem for refined elements is

$$\begin{cases} \left(\dfrac{G_C}{l} + 2\mathcal{H}^+\right) d - G_C l \boldsymbol{\nabla}\cdot\boldsymbol{q} = 2\mathcal{H}^+ & \text{in } \hat{K}_i, \\ \boldsymbol{q} - \boldsymbol{\nabla} d = \boldsymbol{0} & \text{in } \hat{K}_i, \\ [\![\boldsymbol{q}\cdot\boldsymbol{n}]\!] = \boldsymbol{0} & \text{on } \mathcal{I}_i, \\ d = \tilde{d}_i & \text{on } \mathcal{I}_i, \\ d = \hat{d} & \text{on } \partial\hat{K}_i. \end{cases} \tag{2.22}$$

The corresponding weak form is: given $\hat{d} \in \Lambda^h_{ref}(\Gamma)$, find $d \in \mathcal{P}^p_{\text{ref}}(K_i)$, $\boldsymbol{q} \in [\mathcal{P}^p_{\text{ref}}(K_i)]^{n_{sd}}$, $\tilde{d}_i \in \Lambda^h_{\text{ref}}(\mathcal{I}_i)$ such that

$$\begin{aligned} &-\int_{\hat{K}_i} G_C l\ v\boldsymbol{\nabla}\cdot\boldsymbol{q}\ \mathrm{d}V - \int_{\partial\hat{K}_i} G_C l\tau\ (\hat{d}-d)v\ \mathrm{d}s - \int_{\mathcal{I}_i} 2G_C l\tau \left(\tilde{d}_i - \{d\}\right) v\ \mathrm{d}s + \\ &\qquad + \int_{\hat{K}_i}\left(\frac{G_C}{l} + 2\mathcal{H}^+\right) vd\ \mathrm{d}V = \int_{\hat{K}_i} v2\mathcal{H}^+\ \mathrm{d}V, \\ &\int_{\hat{K}_i} \boldsymbol{w}\cdot\boldsymbol{q}\ \mathrm{d}V + \int_{\hat{K}_i} (\boldsymbol{\nabla}\cdot\boldsymbol{w})d\ \mathrm{d}V - \int_{\partial\hat{K}_i} \boldsymbol{w}\cdot\boldsymbol{n}\ \hat{d}\ \mathrm{d}s - \int_{\mathcal{I}_i} [\![\boldsymbol{w}\cdot\boldsymbol{n}]\!]\ \tilde{d}_i\ \mathrm{d}s = 0, \\ &\int_{\mathcal{I}_i} \tilde{v}\ [\![\hat{\boldsymbol{q}}\cdot\boldsymbol{n}]\!]\ \mathrm{d}s = 0, \end{aligned} \tag{2.23}$$

for all $v \in \mathcal{P}^p_{\text{ref}}(K_i)$, for all $\boldsymbol{w} \in [\mathcal{P}^p_{\text{ref}}(K_i)]^{n_{sd}}$, for all $\tilde{v} \in \Lambda^h_{\text{ref}}(\mathcal{I}_i)$. The numerical flux prescribed on $\partial\hat{K}_i$ and $\mathcal{I}_i$ is the same as for the standard elements (2.12). The structure for the local solver is also preserved in this case.

Remark 5 (Postprocessed d^* in refined elements)**.** For the postprocess problem to determine the superconvergent solution d^* in refined elements, the computations are done at subelement level. No condition on the inner trace $\mathcal{I}_i$ needs to be added at the formulation, since the problem is solved at each subelement independently.

2.2.3 Refining criterion

The phase-field solution needs more resolution along cracks, where it presents sharp variations. The damage field takes values close to 1 near the crack and values close

to 0 far from the crack, thus we can use the value of the damage field as an indicator of whether an element needs to be refined or not. In particular, we use the value of the postprocessed damage field d^* on the nodes of the element to define the refining criterion. An element K_i is refined if a threshold value d_{ref} is reached, that is,

$$i \in E_{\text{ref}} \quad \text{if} \quad \max_{\boldsymbol{x} \in K_i} d^*(\boldsymbol{x}, t) \geq d_{\text{ref}}. \tag{2.24}$$

Numerically, we have found that a reasonable value for d_{ref} is between 0.1 and 0.2. This will be discussed later in the numerical examples.

The refining criterion is applied at the end of every staggered iteration (in step 4 in Algorithm 2.1) because, since we are modeling brittle fracture, the crack can grow significantly at a single load step.

It is important noting that some elements must be refined from the beginning where crack inception is expected, for instance at the tip of preexisting notches.

Here, coarsening of the discretization in the wake of the crack tip is not considered. As the phase-field solution has sharp variations across the whole crack, resolution is needed not only near the crack tip, but also in the rest of the crack to properly describe its geometry.

2.2.4 Refined elements and faces

To integrate over the refined elements and faces, we use two reference elements with the standard and refined approximation spaces, respectively. In this way, we incorporate all the information of the refinement into the reference element, and most computations and assembly of elemental matrices can be done with the standard element routines. We can use a unique refined reference element because the refinement factor is the same in all refined elements, and it can be computed only once in the preprocess. An alternative is to loop over all subelements of refined elements using the standard reference element.

The refined reference element has all the integration points, nodes and shape functions of the HDG discretization of the submesh. The shape functions associated to a subelement are extended with value 0 to the rest of subelements. The refined reference element also includes inner geometrical information for the computation of integrals and jumps on inner faces, and the assembly to subelements nodal values.

To illustrate the discretization with subelements, Figure 2.3 shows a representation of the nodal basis functions and integration points for a 1D standard reference

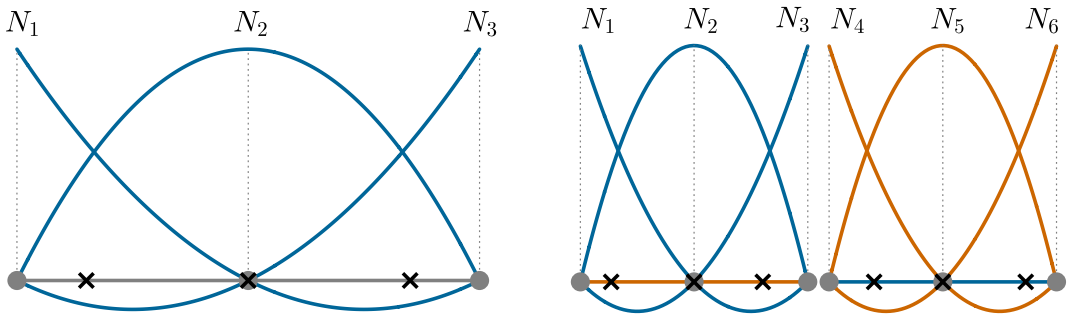

Figure 2.3: Scheme of the discretizations for the standard reference element (left) and for the refined reference element with refinement factor 2 (right) for degree of approximation $p = 2$ in 1D. The nodes of the element are represented by grey dots and the integration points by black crosses. The refined element has 6 elemental basis functions.

element (on the left) and for a refined reference element (on the right). In this example, the refined element is split into 2 subelements, so it has twice as many shape functions and integration points as the standard element. Analogously, the 2D refined elements in Figure 2.2, which are split into 4 subelements, have 4 times the number of shape functions and integration points of the standard element. Shared faces between refined elements and boundary faces are also refined with refined discretization as the one examplified in Figure 2.3.

A refined element can have some refined faces and some standard faces. To avoid dealing with different cases on elemental computations, all faces are integrated as if they were refined faces. Then, before assembly, a projection operator is applied to standard faces, using the fact that the standard space is included in the refined one.

2.2.5 Convergence study

To test the proposed formulation and its implementation, we study the convergence of the numerical solution to a known analytical solution. Since the problem in refined elements is formulated to be equivalent to non-conformal h-refinement with HDG, the expected orders of convergence are the same that are proved for the standard HDG formulations. For a fixed computational mesh, we study the convergence when refining all of its elements for an increasing refinement factor m.

Consider a square domain $\Omega = [0, 1]^2$ with a computational mesh of 10×10 elements. For the equilibrium equation, we set the body force and Dirichlet boundary

conditions on $\partial\Omega$ corresponding to the analytical solution

$$\boldsymbol{u}(x,y) = \begin{pmatrix} \exp\left(0.1\sin(5.1x+6.2y)\right) \\ \exp\left(0.3\cos(4.3x+30.4y)\right) \end{pmatrix},$$

considering a given damage field $d(x,y) = (\sin(x+y)+1)/5$, with material parameters $E = 20$ GPa, $\nu = 0.3$ and numerical parameter $\tau = 100$. For refinement factors $m = 1, 2, 4, 8$, the convergence plots obtained are shown in Figure 2.4, with a slightly better convergence than the expected one: orders of convergence in the L^2 norm are $p+1$ and $p+1/2$ for the displacement field $\boldsymbol{u}$ and its gradient $\boldsymbol{J}$, respectively, if degree of approximation p is used.

For the damage equation, we impose Dirichlet boundary conditions on $\partial\Omega$ and the source function $\mathcal{H}$ corresponding to the solution

$$d(x,y) = \frac{\sin(3x+y)+1}{3},$$

with parameters $G_C = 8.9 \cdot 10^{-5}$ kN/mm, $l = 0.01$ mm, $\tau = 100$. In this case, the expected orders of convergence are $p+1$ for the damage field d and $p+2$ for the postprocessed damage field d^*. Figure 2.5 shows the convergence plots obtained for this equation on the same 10×10 mesh and for refinement factors $m = 2, 4, 8, 16$, again in agreement with the theoretical convergence rates for uniform h-refinement.

Whether to condensate or not the interior traces in refined elements is an implementation decision that does not affect the numerical solution, but it has an important

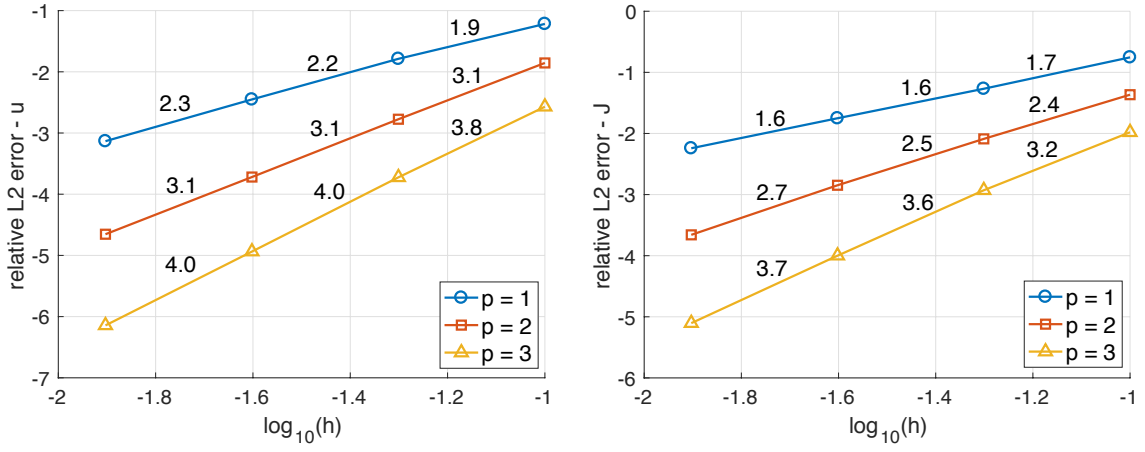

Figure 2.4: *Equilibrium equation.* Convergence plots obtained for a fixed mesh of 10×10 elements when refining its elements, for degrees of approximation $p = 1, 2, 3$, for $\boldsymbol{u}$ (left) and $\boldsymbol{J}$ (right). h is the subelement size and the numbers are the slopes in each segment.

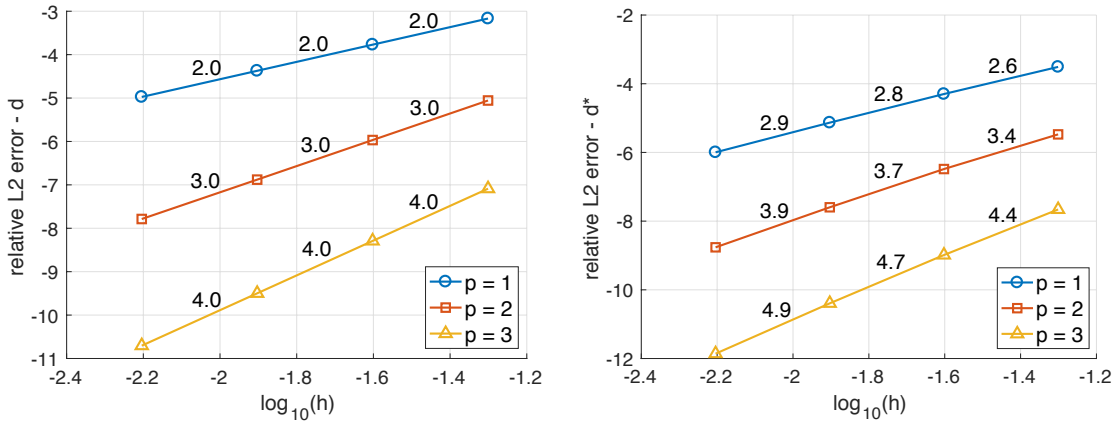

Figure 2.5: *Damage equation.* Convergence plots obtained for a fixed mesh of 10×10 elements when refining its elements, for degrees of approximation $p = 1, 2, 3$, for d (left) and d^* (right). h is the subelement size and the numbers are the slopes in each segment.

effect in the resulting global system of equations. As an example, a mesh with 10×10 elements with refinement factor $m = 8$ and a mesh with $10m \times 10m$ elements without refinement are considered. These discretizations are equivalent in the sense that they lead to the same numerical solution, but the degrees of freedom corresponding to inner traces are not incorporated into the global system in the discretization with refinement. Figure 2.6 shows the sparsity patterns for degree $p = 2$. The matrix for $10m \times 10m$ standard elements (left plot) has size 75 840, and the number of non-zero coefficients per row is 42, when not affected by the boundary. For the matrix corresponding to 10×10 refined elements (right plot) the number of non-zero coefficients per row increases to 336, due to the fact that now each refined face has 8 times more degrees of freedom than a standard face, but the size of the matrix is significantly reduced to 8 640. That is, the condensation of the interior traces leads to more coupling of degrees of freedom, but also to a reduced dimension and number of non-zero entries in the resulting global matrix.

In Figure 2.7, we compare the CPU time needed for the direct solver (\ operator in Matlab) to solve the two systems, for different values of the refinement level m and degree p. The ratio of CPU times between the HDG discretization with refinement and the corresponding standard discretization is below 1 in all cases. That is, condensating the interior trace leads to a saving in CPU time for the direct linear solver.

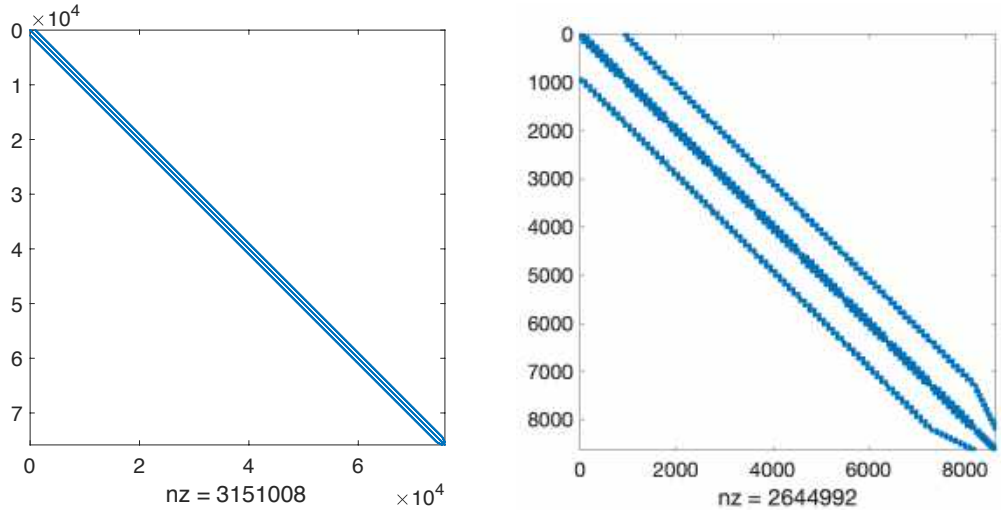

Figure 2.6: *Equilibrium equation.* Sparsity of matrices: (left) standard HDG with 80×80 elements and (right) HDG with a 10×10 elements and refinement factor $m = 8$. Degree of approximation $p = 2$.

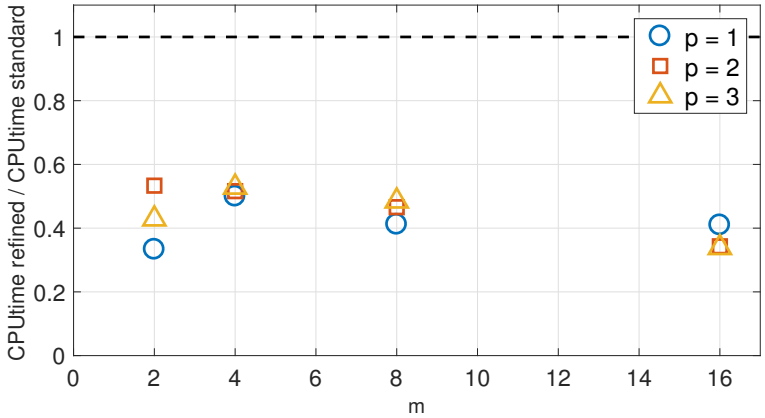

Figure 2.7: *Equilibrium equation.* Comparison of CPU times for the direct solver. CPU time for the HDG discretization with refinement over the CPU time for standard HDG, for meshes with $10m \times 10m$ elements (equivalently 10×10 with refinement factor m in all elements) and degrees of approximation $p = 1, 2, 3$.

2.3 Numerical experiments

In this section, we test the ability of the proposed adaptive strategy to model propagating cracks in four different examples: three well-known benchmark tests in fracture simulation and a new test with crack branching in the quasi-static regime, with no need of material heterogeneities to trigger the bifurcation.

In the equilibrium equation, plane strain conditions are assumed. In all examples,

we iterate over the staggered scheme until convergence is reached with a tolerance of 10^{-2} for the postprocessed damage field d^*. The HDG stabilization parameter, for both the equilibrium and the damage equations, is taken as $\tau = 100$.

In this chapter, the degradation function is taken as $g(d) = (1-d)^2 + \eta$, with $\eta = 10^{-5}$. During the development of the thesis, we have seen that adding a residual stiffness η does not affect the results, but is not necessary in practice. Thus, in the rest of chapters we will assume $\eta = 0$.

2.3.1 Shear test

With this example, we illustrate the robustness of the proposed adaptive strategy and study the influence of the refinement threshold value d_{ref}, this is, the value of damage that triggers the refinement. Results obtained with locally and dynamically refined discretizations are compared to the results of a globally refined mesh.

Consider a square plate, which is pre-cracked at mid-height as shown in Figure 2.8. The plate is fixed on its bottom edge and is subjected to an imposed horizontal displacement on its top edge. Following Ambati et al. [2015], the material parameters are $E = 210$ GPa, $\nu = 0.3$ and $G_C = 2.7 \cdot 10^{-3}$ kN/mm. The length scale parameter is $l = 0.015$ mm. The increment of displacement for the load process is $\Delta u_D = 10^{-4}$ mm. Computations are done with degree $p = 1$, except for the postprocessed damage d^* which is approximated with degree $p + 1 = 2$.

As a reference solution, the domain is discretized with a uniform quadrilateral mesh of 240×240 elements. Three coarser uniform meshes with 48×48, 24×24 and 12×12 elements are also considered with the corresponding refinement factor

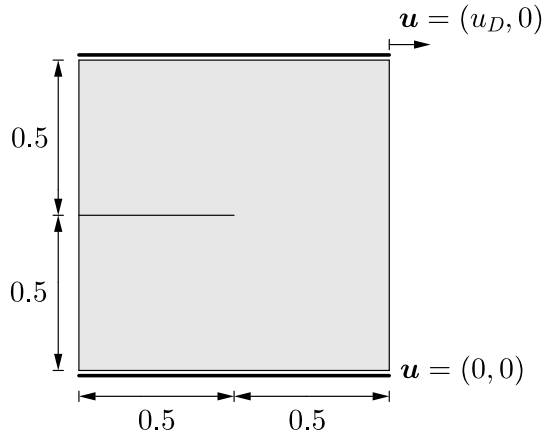

Figure 2.8: *Shear test.* Geometry and boundary conditions. Dimensions in mm.

$m = 5, 10, 20$ so that the characteristic size of the subelements is $h = 1/240$ mm in refined elements for all discretizations. For all discretizations, the four elements around the initial crack tip are refined from the beginning.

We start by discussing the influence of the refinement value d_{ref}. Figure 2.9 shows the load-displacement curves obtained for refinement values $d_{\text{ref}} = 0.1$ and $d_{\text{ref}} = 0.2$. Results obtained with the adaptive strategy are very similar to the reference solution. The peaks appearing in the curves corresponding to the coarsest initial mesh of 12×12 elements coincide with the refinement of elements as the crack propagates, and are interpreted as corrections when spatial resolution is enhanced: the discretization is too coarse in standard elements to properly solve the equilibrium equation with d close to 0, but the adaptive algorithm still provides reasonable results.

Now we consider a discretization with 24×24 elements and refinement factor of 10, with several values $d_{\text{ref}} = 0.1$, 0.2, 0.5 and 0.7. The load-displacement curves are plotted in Figure 2.10. If the refinement value is too high, the corrections once elements become refined are not enough to capture the solution and the curve differs significantly from the reference one. A refinement value d_{ref} between 0.1 and 0.2 provides good results. Moreover, our experience is that in this range of values the refinement is kept local near cracks.

The reduction of degrees of freedom is substantial when considering the adaptive strategy. Table 2.1 depicts the number of degrees of freedom for the global problem of the equilibrium equation for each one of the discretizations and for two different

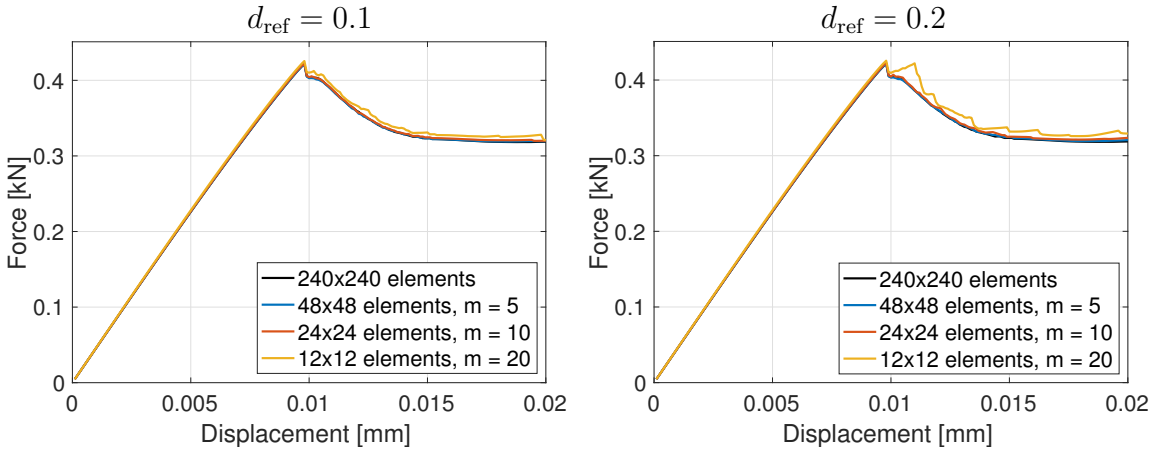

Figure 2.9: *Shear test.* Load-displacement curves for different discretizations and degree of approximation $p = 1$ for refinement values $d_{\text{ref}} = 0.1$ (left) and $d_{\text{ref}} = 0.2$ (right).

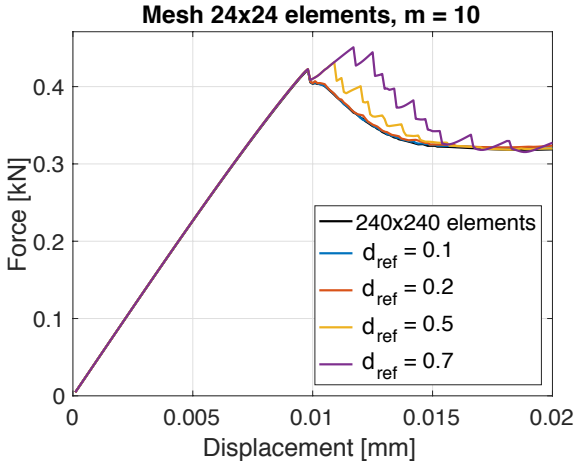

Figure 2.10: *Shear test.* Load-displacement curves for mesh 24×24 with refinement 10×10 and different refinement values. Degree of approximation $p = 1$.

Table 2.1: *Shear test.* Comparison of the number of degrees of freedom (#dof) for different discretizations with linear approximation functions.

Mesh	m	d_{ref}	Initial #dof	Final #dof	%
240×240	–	–	461 280	461 280	100%
48×48	5	0.1	18 608	25 920	5.6%
		0.2	18 608	22 736	4.9%
24×24	10	0.1	4 836	9 480	2.1%
		0.2	4 836	7 572	1.6%
12×12	20	0.1	1 556	4 596	1.0%
		0.2	1 556	3 684	0.8%

refinement values d_{ref}, 0.1 and 0.2. Since we use a uniform mesh in all the domain and the refinement is very local near the crack, less degrees of freedom are needed for coarser initial meshes. For the mesh with 24×24 elements and refinement factor $m = 10$, we obtain accurate results with only $1.6 - 2.1\%$ of the degrees of freedom of the reference discretization. For the coarsest mesh, with 12×12 elements and $m = 20$, the approximation obtained is reasonable given the limitation of the discretization to resolve the mechanical problem, and with only about 1% of the number of degrees of freedom.

Figure 2.11 shows the damage field obtained with these discretizations at three different load steps when a refinement value of $d_{\text{ref}} = 0.2$ is used. The damage path

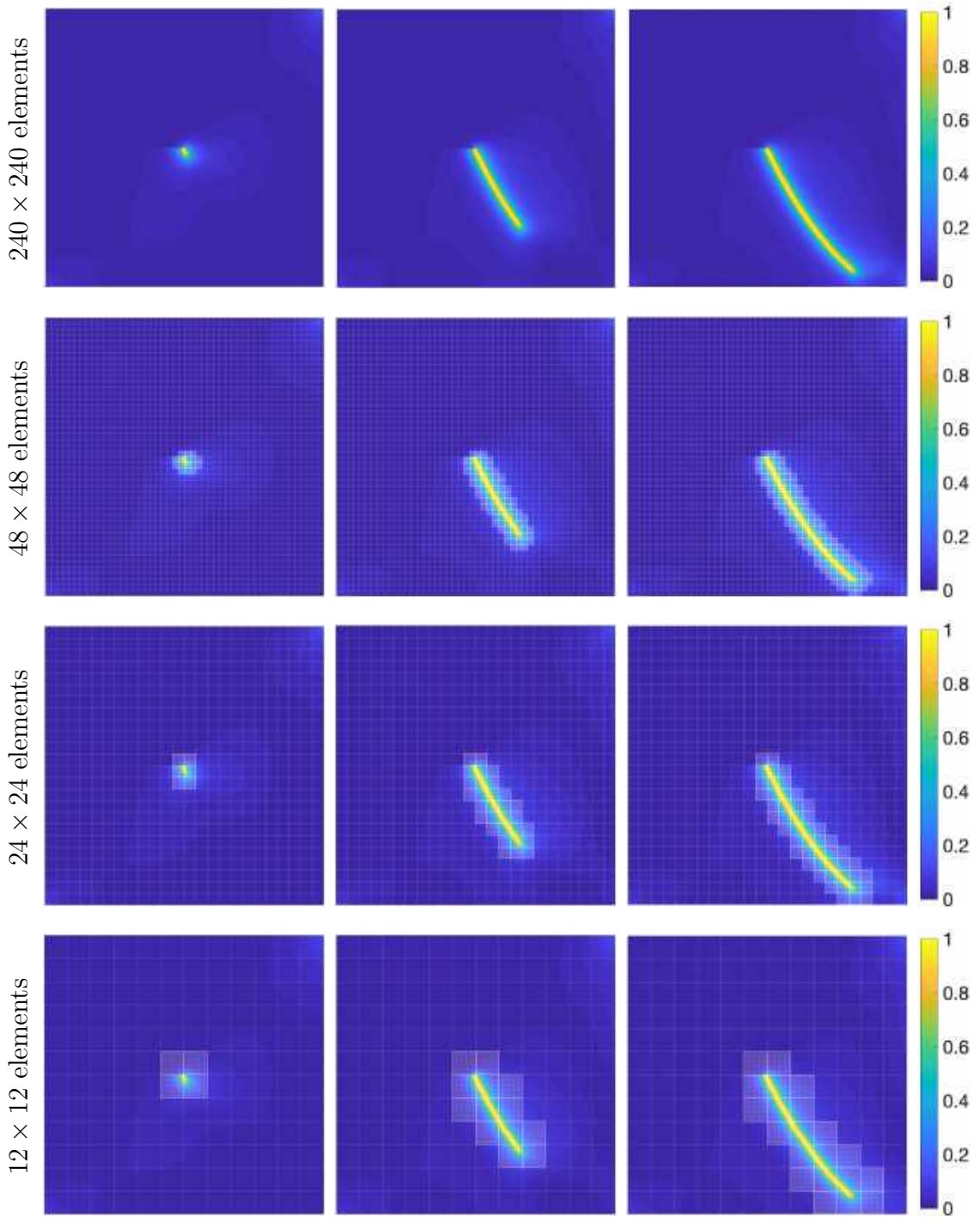

Figure 2.11: *Shear test.* Damage field for various imposed displacements, with degree of approximation $p = 1$ and refinement value $d_{\text{ref}} = 0.2$.

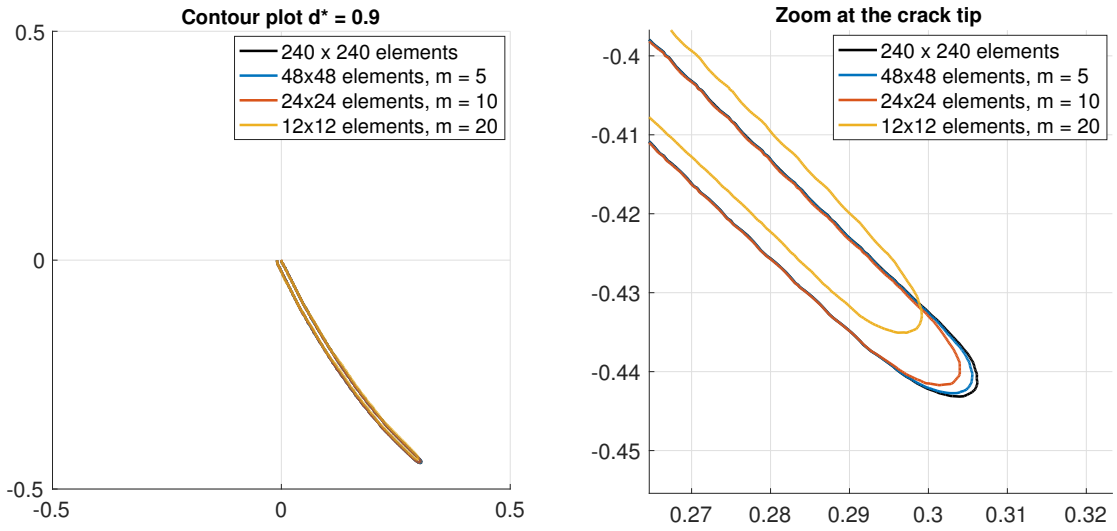

Figure 2.12: *Shear test.* Left: contour plot at $d^* = 0.9$ for the different discretizations at imposed displacement $u_D = 0.020$ mm, with degree of approximation $p = 1$ and refinement value $d_{\text{ref}} = 0.2$. Right: zoom at the crack tip.

obtained with the considered dynamically changing discretizations is esentially the same as the one of the reference solution. This can be seen more clearly in Figure 2.12, where the contour plot corresponding to $d^* = 0.9$ is depicted for the different discretizations, showing an excellent agreement of the crack tip position at the final load step $u_D = 0.02$ mm. We can conclude that refining locally along the crack is enough to capture the solution and that the adaptive strategy is robust with respect to the discretization, as long as elements are refined appropriately to resolve the length scale parameter l.

2.3.2 L-shaped panel test

In this example, we test the performance of the proposed strategy for higher degrees of approximation. Consider an L-shaped plate with geometry and prescribed boundary conditions as shown in Figure 2.13. The same material parameters as in Ambati et al. [2015] are employed, this is, $E = 25.8423$ GPa, $\nu = 0.18$ and $G_C = 8.9 \cdot 10^{-5}$ kN/mm. A length scale parameter $l = 2$ mm and an increment for the imposed displacements of $\Delta u_D = 10^{-3}$ mm are used. The refinement value is $d_{\text{ref}} = 0.1$.

A uniform quadrilateral mesh with mesh size $h = 10$ mm is employed, with three discretizations given by degrees of approximation $p = 1, 2$ and 4. At the beginning, none of the elements are refined. Equivalent discretizations for refined elements are

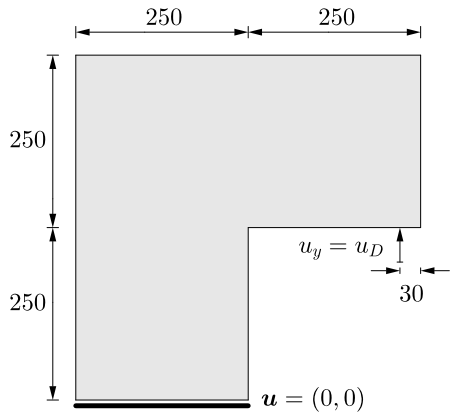

Figure 2.13: *L-shaped test.* Geometry and boundary conditions. Dimensions in mm.

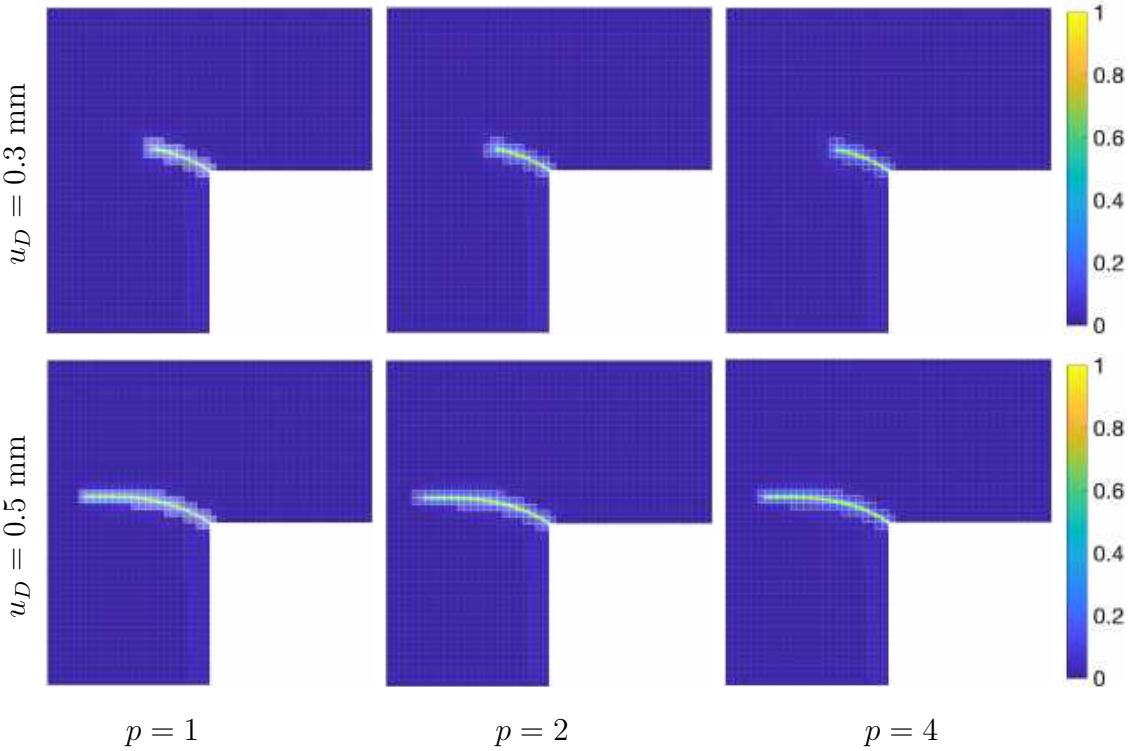

Figure 2.14: *L-shaped test.* Damage field at $u_D = 0.3$ mm and $u_D = 0.5$ mm obtained with degrees of approximation $p = 1, 2, 4$ and corresponding refinement factors $m = 20, 10, 5$, respectively.

used: for the case $p = 1$ the refinement factor is $m = 20$, for $p = 2$ we refine by factor $m = 10$ and for $p = 4$ we refine by factor $m = 5$. Figure 2.14 shows the crack evolution for the different degrees of approximation and the corresponding load-displacement curves are depicted in Figure 2.15.

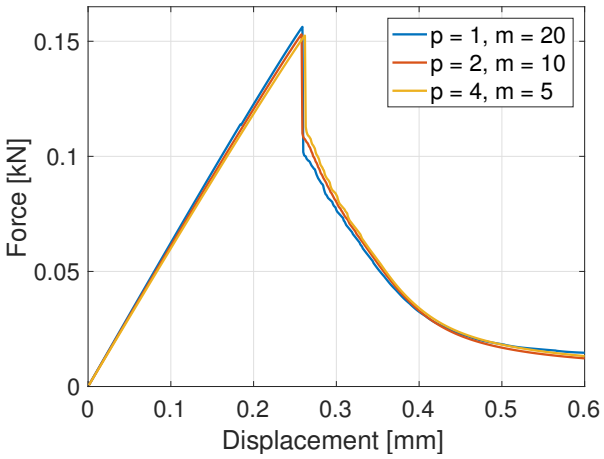

Figure 2.15: *L-shaped test.* Load-displacement curves for degrees of approximation $p = 1$, 2 and 4 with refinement factor m. The refinement value is $d_{\text{ref}} = 0.1$.

The adaptive strategy performs correctly for all cases giving very similar results, showing again the robustness of the proposed strategy and its capability to resolve the crack growth with an automatic adaptation, now with different degrees of approximation. Nonetheless, it is worth mentioning that when using high-order approximations, one must ensure that the refinement is fine enough to properly capture the sharp variation of the phase-field variable in order to avoid oscillations.

2.3.3 Notched plate with a hole

Since the proposed refinement is done in the reference element, the method also works for non-structured meshes. In this example, we consider a domain with a hole to illustrate the performance of the strategy in this scenario.

This test was first proposed by Ambati et al. [2015]. Consider a notched specimen with a non-centered hole as shown in Figure 2.16. The plate is fixed on the lower pin and has imposed vertical displacement on the top pin. The parameters are $E = 6$ GPa, $\nu = 0.22$ and $G_C = 2.28 \cdot 10^{-3}$ kN/mm. The length scale parameter is $l = 0.5$ mm and we use fixed displacement increments of $\Delta u_D = 10^{-2}$ mm.

We consider a non-structured mesh of quadrilaterals, with element size $h \simeq 5$ mm, and degree of approximation $p = 2$, see Figure 2.16. The refinement factor is $m = 20$ and we refine using the threshold value $d_{\text{ref}} = 0.2$. The pre-existing crack is defined by a history variable $\mathcal{H}^+$ as described in Borden et al. [2012], refining the elements that contain it.

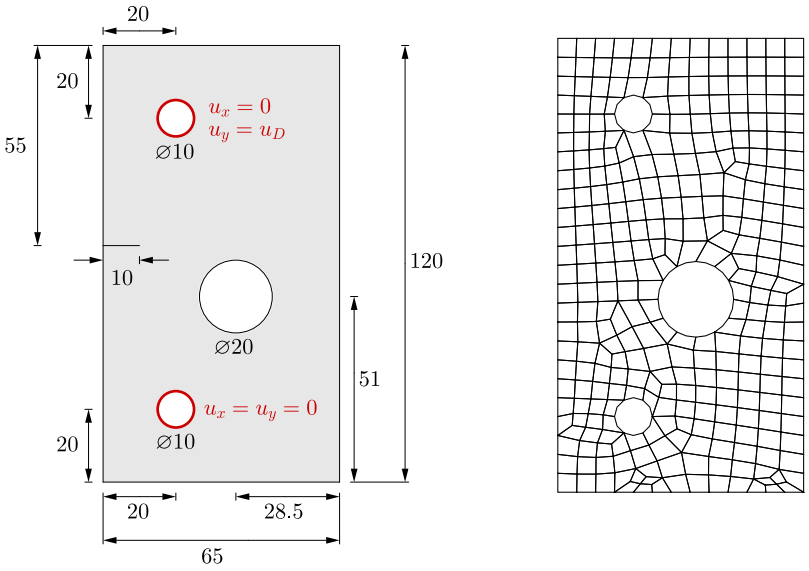

Figure 2.16: *Plate with a hole.* Left: Geometry and boundary conditions. Dimensions in mm. Right: Computational mesh.

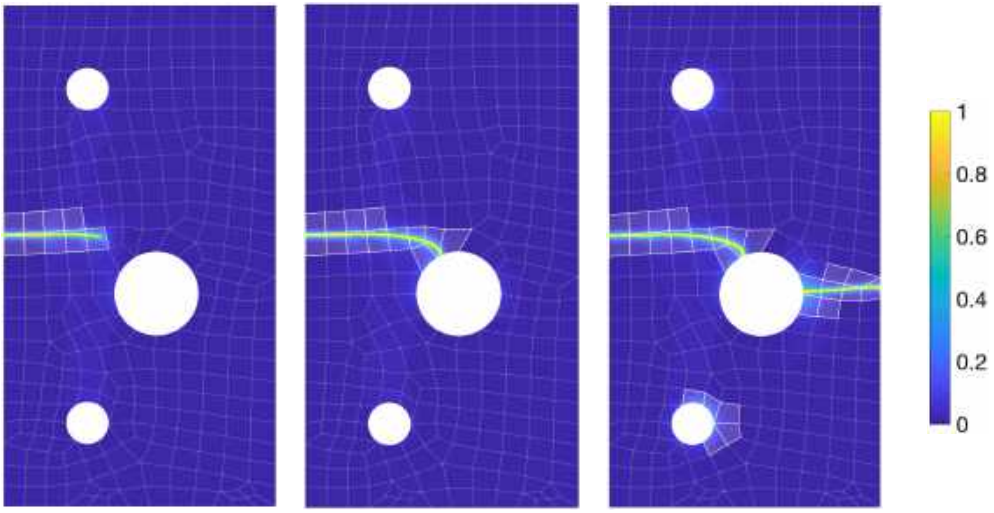

$u_D = 0.31$ mm $u_D = 0.50$ mm $u_D = 1.07$ mm

Figure 2.17: *Plate with a hole.* Damage field at various load steps for degree of approximation $p = 2$, refinement factor $m = 20$ and refinement threshold value $d_{\text{ref}} = 0.2$.

Figure 2.17 shows the damage field obtained at different load steps. As expected, the crack is attracted to the hole and a second crack appears in the other side, while elements along the crack are dynamically refined. Elements surrounding the lower pin are also refined because the threshold refinement value is reached in them.

2.3.4 Branching test

We propose an example of crack branching for quasi-static models of fracture. In contrast with other examples that can be found on the literature, here the branching is caused by the boundary conditions and not by any material heterogeneity. This example illustrates the suitability of the adaptive strategy for complex crack patterns.

Consider a square plate occupying the domain $[-1, 1]^2$ mm^2, with a pre-crack at mid height of length 0.1 mm, see Figure 2.18. The plate is clamped on its right edge and vertical displacements are imposed on the top and bottom edges following a parabolic function, this is, $f(x) = u_D(x-1)^2/8$. The crack is expected to propagate horizontally up to a certain point and then, because of the clamped right edge, it is expected to branch. The branching point is unknown and, moreover, will strongly depend on the material parameters and profile of prescribed displacements. The proposed adaptive strategy enables to consider a uniform computational mesh in all the domain and the discretization will refine accordingly to the crack evolution.

The parameters are $E = 20$ GPa, $\nu = 0.3$, $G_C = 8.9 \cdot 10^{-5}$ kN/mm and $l = 0.0075$ mm. The loading process is governed by an increment of $\Delta u_D = 10^{-4}$ mm. The problem is solved using a uniform quadrilateral mesh of 41×41 elements with refinement factor $m = 15$, linear shape functions and refinement value $d_{\text{ref}} = 0.2$. Again, the initial crack is defined following Borden et al. [2012].

Figure 2.19 shows the damage field obtained at different load steps. The complete evolution of the crack, and of the refinement, can be seen in the YouTube video in

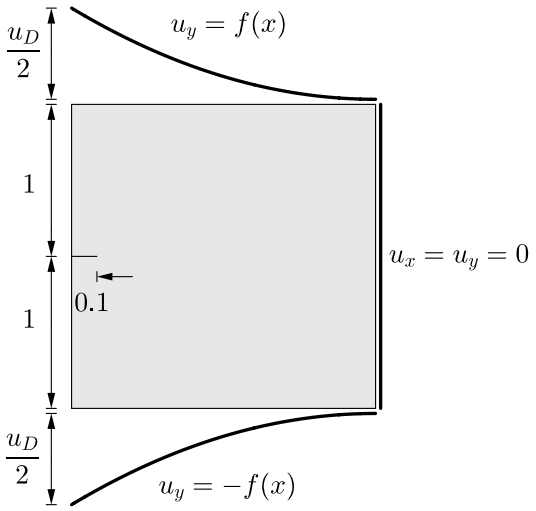

Figure 2.18: *Branching test.* Geometry and boundary conditions. Dimensions in mm.

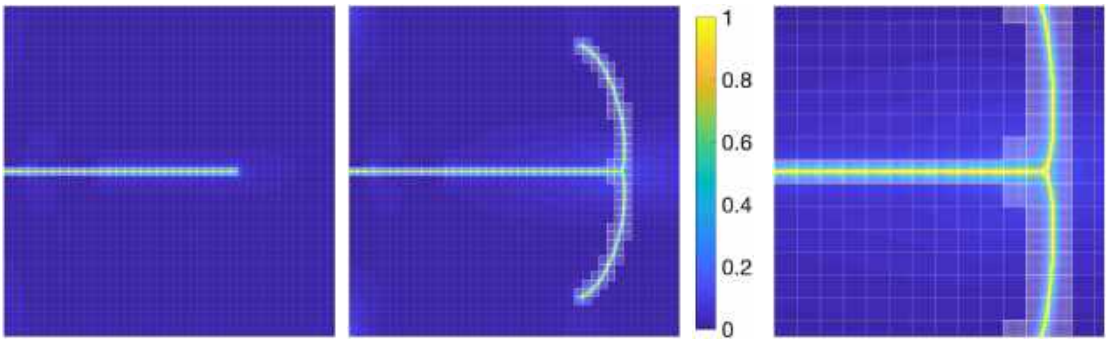

$u_D = 0.03$ mm $u_D = 0.07$ mm $u_D = 0.07$ mm (zoom)

Figure 2.19: *Branching test.* Damage field at two different load steps, and zoom, for degree of approximation $p = 1$ and refinement value $d_{\text{ref}} = 0.2$.

Muixí et al. [2019a]. The adaptive strategy enables to approximate the branching of the crack automatically, with no need of remeshing.

2.4 Conclusions

In this chapter, we present an adaptive phase-field model, with very local and non-conforming refinement. The key ingredient of the proposal is that it is based on the HDG discretization technique, rather than the standard CG method. For our purposes, the most attractive feature of HDG is that approximation functions are discontinuous across elements, and then continuity of the solution is weakly imposed. This handles in a natural way the use of different approximation spaces in adjacent elements. As a result, a coarse mesh can be very locally refined as cracks propagate, with any desired refinement factor m and no special treatment of the transition zone.

An implementation based on a standard and a refined reference element is proposed, keeping the original background mesh fixed during all the simulation and the standard structure of the HDG code.

We illustrate the adaptive strategy in various numerical examples, including a new branching test, with refinement factors up to $m = 20$ and degrees up to $p = 4$. Numerical results demonstrate the accuracy and robustness of the strategy regarding the crack path, load-displacement curves and position of the crack tip. Also, since the refinement is done at the reference element, the method can be used on non-structured background meshes.

Chapter 3

Adaptive refinement based on Nitsche's method[1]

Motivated by the good performance of the HDG adaptive strategy in Chapter 2, we present here an alternative approach based on the more widely used continuous Galerkin (CG) formulation of the FEM.

The feature of HDG that we exploit in the adaptive strategy is the imposition of continuity in weak form between elements; the formulation itself handles the non-conformal approximations between elements of different type. However, HDG has a higher computational cost and a more involved implementation than CG. Here, we develop an alternative strategy, which can be easily integrated into a CG code for the phase-field equations.

The computational mesh is partitioned into standard and refined regions. In each region, we use a continuous FEM formulation with the corresponding space of approximation, standard or refined. Then, on the interface between regions, continuity is imposed in weak form to deal with the non-conformal discretizations via Nitsche's method.

The new methodology maintains the strong points of our previous HDG proposal. In particular, only two types of elements are considered, standard and refined, by exploiting the fact that the refinement factor needed is known beforehand from the length-scale parameter l of the model. The background mesh is fixed during all

[1]This chapter is based on Muixí et al. [2020a].

the simulation and nested refined elements are automatically located along cracks. Continuity between elements of different type is also imposed in weak form to obtain very local refinements along cracks without dealing with hanging nodes, and a damage threshold is used as simple indicator to trigger the refinement.

Nevertheless, the new approach also presents various key differences with respect to the previous one. First of all, it is based on the widespread CG formulation, rather than in a more sophisticated HDG formulation. Continuity between standard and refined regions is then imposed in weak form by means of Nitsche's method, rather than via HDG fluxes.

Nitsche's method, first proposed by Nitsche [1971], is a well-established approach in the literature to impose boundary conditions in weak form, see Fernández-Méndez and Huerta [2004], and to enforce continuity between regions with nonmatching discretizations, see for instance Becker et al. [2010] and La Spina et al. [2020]. The method is an alternative to the use of Lagrange multipliers without additional unknowns. In Nitsche's method, the weak form of the problem is modified, introducing a scalar constant parameter whose value has to be appropiately chosen to ensure coercivity of the bilinear form. In fact, this parameter acts as a stabilization parameter and, differently from what happens in penalty methods, moderate values of order $\mathcal{O}(h^{-1})$, with h the element size, provide accuracy and optimal convergence.

The chapter is organized as follows. In Section 3.1, we describe the proposed refinement strategy, also commenting on the implementation. Then, in Section 3.2, we derive the formulation of Nitche's method for the phase-field equations. Numerical experiments to test the performance and robustness of the strategy can be found in Section 3.3, including branching and coalescence in 2D and a fully 3D example. Conclusions are in Section 3.4.

3.1 Adaptive refinement strategy

The key ingredients for the dynamically h-refined discretization presented in this chapter are:

i. the partition of the mesh into standard and refined regions, through the definition of two types of elements with different approximation spaces, *standard* and *refined*, which are mapped into a fixed background mesh,

ii. a fixed refinement factor in refined elements, which is known a priori depending on the length-scale l of the model,

iii. continuous FEM approximations in the standard and refined regions, and

iv. the weak imposition of continuity on the interface between refined and standard elements by means of Nitsche's method.

This section aims to give a complete description of the strategy, regarding also the implementation.

In principle, the approach is also applicable to p and hp-adaptivity. However, these options are not considered here since the sharp variations of the solution may cause oscillations when using a high degree p for the approximation.

3.1.1 The refinement process

Again, we consider two types of reference element: standard and refined. Standard elements are mapped to the standard reference element, whose space of approximation is the space of polynomials up to degree p, $\mathcal{P}^p$, as usual in a finite element approximation. Refined elements are mapped to the refined reference element, whose space of approximation is h-refined with a uniform submesh with $m^{n_{sd}}$ subelements, now with a continuous FE approximation between subelements. The refinement factor m is such that the resulting discretization is able to resolve the length-scale parameter l of the phase-field model, and can be chosen by following the expression in (2.15).

The computational mesh describes the geometry and is fixed during all the simulation. Elements along cracks are refined, while the rest of the elements of the mesh are assumed as standard. As the simulation evolves and cracks propagate, more elements become refined. This strategy leads to a nonconformal discretization and special treatment on the interface between the two types of element is needed.

The proposed discretization is equivalent to a nonconformal h-refinement. The implementation with a refined reference element is chosen here for convenience, since it reduces the cases to consider to the minimum, and allows keeping the initial mesh as background mesh in the whole computation. It is worth noting that this particular refinement strategy is suited for crack tracking problems with phase-field models because the required element size in refined elements is known a priori, depending only on the length-scale l. It would not be applicable to adaptive refinement in other contexts.

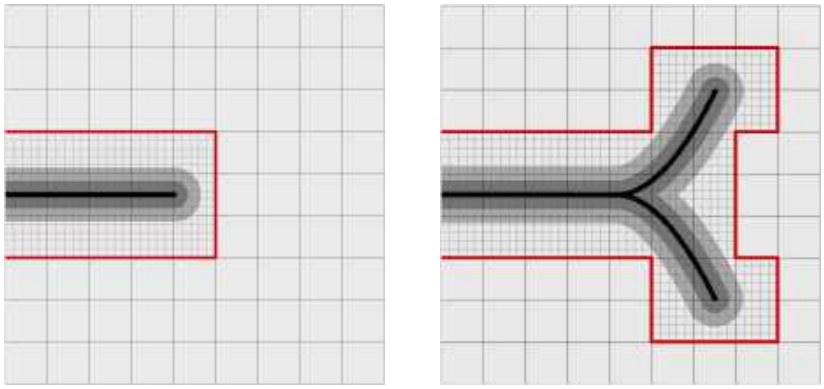

Figure 3.1: Scheme of the discretization in two consecutive steps, with h-refined elements along the crack and standard elements in the rest of the domain. The interface on which continuity is imposed in weak form is in red.

Figure 3.1 illustrates an approximation in two consecutive load steps. The discretization is h-refined in a narrow band containing the crack; considering only two types of element results in a very local refinement, with no spreading of the refined zone. On the interface Γ between standard and refined elements (in red in the figure), one needs to impose continuity of the solution.

With the aim of retaining very local refinements, our choice is to impose continuity on the interface in weak form. In the case of imposing continuity in strong form, one would have to deal with the hanging nodes of the nonconformal approximation. Finding the relations between nodes for an arbitrary refinement factor m may be cumbersome in practice, with several cases to implement, specially in 3D.

In this work, we use Nitsche's method to weakly impose continuity. This method keeps the original size of the system, this is, it does not introduce extra variables. The formulation and some details of the method are presented in Section 3.2.

Refining criterion. The criterion to trigger the refinement of elements is analogous to the one explained in Section 2.2.3. That is, at every staggered iteration, elements with damage field d reaching a fixed threshold value, d_{ref}, at one of their nodes are added to the refined region.

Here, we do not consider derefinement of elements because a fine discretization is needed along the whole crack to ensure accuracy of the solution. Coarsening the discretization is considered in Chapter 4, where cracks are introduced as a strong discontinuity with an XFEM approximation in the wake of crack tips.

3.1.2 Refined reference element

We define two reference elements, one for each type of element: standard and refined. Elements in the computational mesh are then mapped to the corresponding reference element depending on its type. In this way, the integration and the assembly for all elements can be done as usual. This is a viable option in this case because the refinement factor m is fixed in refined elements. Therefore, the geometrical information of the h-refinement inside these elements is computed only once in the preprocess.

The refined reference element considers the full approximation space for each subelement, with a continuous approximation between subelements. Figure 3.2 shows the discretization for a refined reference element in 1D, with degree of approximation $p = 2$ and refinement factor $m = 2$. The refined element is divided into two subelements. Thus, it has 5 nodes and 5 shape functions. The reference element has all the integration points of the subelements.

Refining the reference element enables to use the strategy for nonstructured meshes without any additional consideration.

3.1.3 Geometrical information and update of the refined zone

During all the simulation, information for the integration on elements and on the interface Γ needs to be accordingly updated to account for the new refined elements.

We keep the background mesh (X, T) fixed, with X the nodal coordinates matrix and T the connectivity matrix. The original mesh describes the geometry of the

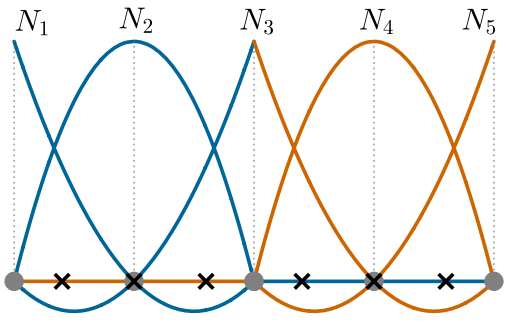

Figure 3.2: Refined reference element in 1D, for degree $p = 2$ and refinement factor $m = 2$. Nodes are represented by grey nodes and integration points, by black crosses. The element has 5 shape functions.

domain during all the process. The information about the refinement includes a mesh for the refined part of the domain, $(X_{\text{ref}}, T_{\text{ref}})$, and a list of faces on the interface Γ, for which continuity is to be imposed by Nitsche's method.

The refined mesh $(X_{\text{ref}}, T_{\text{ref}})$ is created with mappings of the refined reference element to the physical elements in the refined zone. Every time an element is refined, its subelements are added to $(X_{\text{ref}}, T_{\text{ref}})$. This refined mesh is defined only for the assembly, using the connectivity matrix T_{ref} to ensure continuity between adjacent refined elements. The numerical integration and basis functions are computed just using the integration points and basis functions in the refined reference element. Note that the isoparametric transformation can be defined using physical nodes in the background mesh (X, T).

The implementation of Nitsche's method requires computing integrals on the interface between refined and nonrefined zones, Γ. To do so, as a preprocess, interior faces of the mesh (X, T) are numbered and for all of them we store the number of the elements sharing the face and the local number of the face in each element, i.e., we save four integers per face. Then, during the computation, a list of the faces on the interface Γ is updated at every iteration, accounting for the new refined elements.

3.2 Nitsche's formulation

In this section, we state the formulation of Nitsche's method for the equilibrium and the damage equations. Recall that, within the staggered scheme used to solve the phase-field system, the two formulations are independent.

For the equilibrium equation we use the formulation for linear elasticity, accounting for the damage field in the stress-strain constitutive equation. For the damage equation, we add the reaction term to the formulation for the Laplace problem. The original formulations for Nitsche's method applied to interface problems can be found in Hansbo [2005].

Here, Nitsche's method is used to weakly impose continuity between subdomains with different spaces of approximation, standard and refined. Throughout the section, we denote these subdomains as Ω_1 and Ω_2, satisfying $\bar{\Omega} = \overline{\Omega_1} \cup \overline{\Omega_2}$, $\Omega_1 \cap \Omega_2 = \emptyset$. We define the interface where continuity is to be imposed as $\Gamma = \partial\Omega_1 \cap \partial\Omega_2$, as sketched in Figure 3.3.

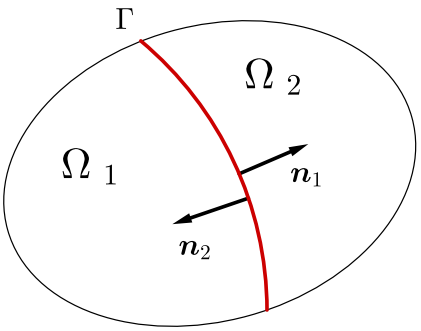

Figure 3.3: Adjacent domains Ω_1 and Ω_2, with different approximation spaces in each one of them. Continuity is imposed by Nitsche's method on Γ (in red).

We define the functional space

$$\mathcal{V}(\Omega) = \{v \in L^2(\Omega) : v|_{\Omega_i} \in \mathcal{H}^1(\Omega_i), \text{ for } i = 1, 2\},$$

including discontinuous functions across Γ.

Throughout the section, the mean and jump operators are defined as $\{\odot\} = \frac{1}{2}(\odot_1 + \odot_2)$ and $[\![\odot]\!] = \odot_1 \boldsymbol{n}_1 + \odot_2 \boldsymbol{n}_2 = (\odot_1 - \odot_2)\boldsymbol{n}_1$, respectively, with $\boldsymbol{n}_1$, $\boldsymbol{n}_2$ the unit exterior normals to Ω_1, Ω_2. Lower indices 1 and 2 on functions indicate their values on Γ from Ω_1 and Ω_2, respectively.

3.2.1 Equilibrium equation

The equilibrium equation in (1.14a) is rewriten in the broken domain Ω as

$$\begin{cases} \boldsymbol{\nabla} \cdot \boldsymbol{\sigma}(\boldsymbol{u}, d) = \boldsymbol{0} & \text{in } \Omega = \Omega_1 \cup \Omega_2 \quad (3.1a) \\ [\![\boldsymbol{u} \otimes \boldsymbol{n}]\!] = \boldsymbol{0} & \text{on } \Gamma, \quad (3.1b) \\ [\![\boldsymbol{\sigma}(\boldsymbol{u}, d) \cdot \boldsymbol{n}]\!] = \boldsymbol{0} & \text{on } \Gamma, \quad (3.1c) \\ \boldsymbol{u} = \boldsymbol{u}_D & \text{on } \Gamma_D, \quad (3.1d) \\ \boldsymbol{\sigma}(\boldsymbol{u}, d) \cdot \boldsymbol{n} = \boldsymbol{t}_N & \text{on } \Gamma_N. \quad (3.1e) \end{cases}$$

Equation (3.1a) imposes equilibrium and is complemented with the usual boundary conditions (3.1d) and (3.1e). Transmission conditions on Γ have to be added to the system to ensure continuity of displacements, (3.1b), and equilibrium of tractions, (3.1c), on the interface between the two subdomains. Since the equilibrium equation is solved for a given damage field d in the staggered approach, the dependence of stress σ on d is not explicitly shown in what follows.

The strategy to derive the formulation consists in writing the standard finite element weak form for each one of the subdomains, summing them, and then adding the necessary integrals to impose the extra conditions on Γ and assure symmetry and coercivity of the bilinear form, while keeping the consistency of the formulation.

Considering the weak form in Ω_1 and Ω_2, separately, and summing them, we obtain that $\boldsymbol{u}$ has to satisfy

$$\int_\Omega \boldsymbol{\nabla v} : \boldsymbol{\sigma}(\boldsymbol{u}) \, \mathrm{d}V - \int_\Gamma (\boldsymbol{v}_1 \cdot \boldsymbol{\sigma}(\boldsymbol{u_1}) \cdot \boldsymbol{n}_1 + \boldsymbol{v}_2 \cdot \boldsymbol{\sigma}(\boldsymbol{u_2}) \cdot \boldsymbol{n}_2) \, \mathrm{d}s - \int_{\Gamma_N} \boldsymbol{v} \cdot \boldsymbol{t}_N \, \mathrm{d}s = 0, \tag{3.2}$$

for all $\boldsymbol{v} \in [\mathcal{V}(\Omega)]^{n_{sd}}$ such that $\boldsymbol{v} = \boldsymbol{0}$ on Γ_D.

To impose condition (3.1c), we arrange the second integral in (3.2) by using the algebraic identity

$$\boldsymbol{a}_1 \cdot \boldsymbol{b}_1 \cdot \boldsymbol{n}_1 + \boldsymbol{a}_2 \cdot \boldsymbol{b}_2 \cdot \boldsymbol{n}_2 = \{\boldsymbol{a}\} \cdot [\![\boldsymbol{b} \cdot \boldsymbol{n}]\!] + [\![\boldsymbol{a} \otimes \boldsymbol{n}]\!] : \{\boldsymbol{b}\}, \tag{3.3}$$

which can be easily proved with the definitions of the operators. Thus, using (3.3) and the equilibrium of tractions on Γ (3.1c), equation (3.2) becomes

$$\int_\Omega \boldsymbol{\nabla v} : \boldsymbol{\sigma}(\boldsymbol{u}) \, \mathrm{d}V - \int_\Gamma [\![\boldsymbol{v} \otimes \boldsymbol{n}]\!] : \{\boldsymbol{\sigma}(\boldsymbol{u})\} \, \mathrm{d}s - \int_{\Gamma_N} \boldsymbol{v} \cdot \boldsymbol{t}_N \, \mathrm{d}s = 0. \tag{3.4}$$

At this step, the resulting bilinear form is neither symmetric nor coercive. Two consistent integrals, i.e. null integrals due to continuity (3.1b), are added to remedy these issues, leading to the weak form: find $\boldsymbol{u} \in [\mathcal{V}(\Omega)]^{n_{sd}}$ such that $\boldsymbol{u} = \boldsymbol{u}_D$ on Γ_D and

$$\begin{aligned} \int_\Omega \boldsymbol{\nabla v} : \boldsymbol{\sigma}(\boldsymbol{u}) \, \mathrm{d}V - \int_\Gamma [\![\boldsymbol{v} \otimes \boldsymbol{n}]\!] : \{\boldsymbol{\sigma}(\boldsymbol{u})\} \, \mathrm{d}s - \int_\Gamma \{\boldsymbol{\sigma}(\boldsymbol{v})\} : [\![\boldsymbol{u} \otimes \boldsymbol{n}]\!] \, \mathrm{d}s + \\ + \beta_{\mathrm{E}} \int_\Gamma [\![\boldsymbol{u} \otimes \boldsymbol{n}]\!] : [\![\boldsymbol{v} \otimes \boldsymbol{n}]\!] \, \mathrm{d}s - \int_{\Gamma_N} \boldsymbol{v} \cdot \boldsymbol{t}_N \, \mathrm{d}s = 0, \end{aligned} \tag{3.5}$$

for all $\boldsymbol{v} \in [\mathcal{V}(\Omega)]^{n_{sd}}$ such that $\boldsymbol{v} = \boldsymbol{0}$ on Γ_D, with β_{E} a positive scalar constant. The third integral in (3.5) makes the functional symmetric and imposes condition (3.1b). The fourth integral ensures coercivity of the bilinear form for β_{E} large enough, leading to a positive definite matrix in the discrete linear system.

Let us consider now a finite element mesh with elements $\{K_i\}_{i=1}^{n_{el}}$ satisfying (2.1), which is split into standard elements, in Ω_1, and refined elements, in Ω_2. Then, the discrete space for each component of the solution is

$$\begin{aligned} \mathcal{V}^h(\Omega) = \{v \in \mathcal{V}(\Omega) : v|_{K_i} \in P^p(K_i) \text{ if } K_i \subseteq \Omega_1, \\ v|_{K_i} \in P^p_{\mathrm{ref}}(K_i) \text{ if } K_i \subseteq \Omega_2\}, \end{aligned}$$

where $\mathcal{P}^p$ is the space of polynomials up to degree p and

$$\mathcal{P}^p_{\text{ref}}(K_i) = \{v \in \mathcal{H}^1(K_i) : v|_{K_{ij}} \in \mathcal{P}^p(K_{ij}),\ j = 1...m^{n_{sd}}\},$$

with K_{ij} the subelements from the h-refinement of K_i. That is, a p-th degree standard approximation is considered in Ω_1 and a continuous p-th degree refined approximation based on subelements is considered in the regions containing the crack, Ω_2.

The stability of the formulation depends on the value of β_{E}. To obtain optimal orders of convergence (p+1 in L^2 norm for approximations of degree p), this parameter can be taken of the form

$$\beta_{\text{E}} = \alpha_{\text{E}} E (h/m)^{-1}, \tag{3.6}$$

with E the Young's modulus and h the element size in the background mesh. Taking into account this relation, the parameter that we tune is α_{E}.

It is well-known that the formulation is very robust in terms of the Nitsche's parameter. In practice, moderate values for α_{E} are enough to ensure stability of the solution and there is a wide interval of proper values. When its value is not large enough, solutions are clearly wrong and the unstabilities can be appreciated at plain sight. Going to the other extreme, for values of α_{E} which are much larger than the minimum value providing coercivity, the matrix becomes ill-conditioned, see Fernández-Méndez and Huerta [2004].

Griebel and Schweitzer [2003] propose to approximate the lower bound of Nitsche's parameter by solving an eigenvalue problem. Annavarapu et al. [2012] show that a careful selection of this parameter is required in interfacial problems involving large material heterogeneities or small cut elements. This is not the case in this work, where the Nitsche's method is applied to glue nonconformal approximations. In fact, in our experience, experimentally tuning the parameter is feasible, as shown in Section 3.2.4.

Notice that imposing continuity on the interface by Nitsche's method, the dimension of the resulting system does not increase.

Classical penalty methods are simpler to derive and implement, but they are based on a non-consistent weak form and need much larger parameters, of order $\mathcal{O}\left(h^{-(p+1)}\right)$, for optimal convergence. This leads to very large penalty parameters and ill-conditioning of the matrix, or inaccurate results, see also Fernández-Méndez and Huerta [2004].

3.2.2 Damage equation

The Nitsche formulation for the damage equation is obtained analogously to the equilibrium one. In this case, we rewrite equation (1.14b) as

$$\begin{cases} -G_C l \Delta d + \left(\dfrac{G_C}{l} + 2\mathcal{H}^+ \right) d = 2\mathcal{H}^+ & \text{in } \Omega = \Omega_1 \cup \Omega_2, \quad (3.7a) \\ [\![d\boldsymbol{n}]\!] = \boldsymbol{0} & \text{on } \Gamma, \quad (3.7b) \\ [\![\boldsymbol{\nabla} d \cdot \boldsymbol{n}]\!] = 0 & \text{on } \Gamma, \quad (3.7c) \\ \boldsymbol{\nabla} d \cdot \boldsymbol{n} = 0 & \text{on } \partial\Omega. \quad (3.7d) \end{cases}$$

Again, conditions in (3.7b) and (3.7c) impose continuity of the damage field and its normal derivative on the interface Γ.

The corresponding weak form reads: find $d \in \mathcal{V}(\Omega)$, such that

$$\begin{aligned} \int_\Omega \left(\frac{G_C}{l} + 2\mathcal{H}^+ \right) v d \, \mathrm{d}V + \int_\Omega G_C l \boldsymbol{\nabla} v \cdot \boldsymbol{\nabla} d \, \mathrm{d}V - \int_\Gamma G_C l [\![v\boldsymbol{n}]\!] \cdot \{ \boldsymbol{\nabla} d \} \, \mathrm{d}s - \\ - \int_\Gamma G_C l [\![d\boldsymbol{n}]\!] \cdot \{ \boldsymbol{\nabla} v \} \, \mathrm{d}s + \beta_\mathrm{D} \int_\Gamma [\![d\boldsymbol{n}]\!] \cdot [\![v\boldsymbol{n}]\!] \, \mathrm{d}s = \int_\Omega v 2\mathcal{H}^+ \, \mathrm{d}V, \end{aligned} \quad (3.8)$$

for all $v \in \mathcal{V}(\Omega)$ and with β_D a sufficiently large scalar parameter. To obtain optimal convergence, the Nitsche's parameter can be taken as

$$\beta_\mathrm{D} = \alpha_\mathrm{D} G_C l (h/m)^{-1}, \quad (3.9)$$

with α_D to be tuned or determined from an eigenvalue problem as proposed by Griebel and Schweitzer [2003].

3.2.3 Convergence of the formulation

We study the convergence of the previous formulations with respect to an analytical solution, both in 2D and 3D. In all cases, the Nitsche's parameter is $\alpha = 100$. In the convergence plots, h refers to the element size of the background mesh and the numbers correspond to the slope in each segment.

Convergence in 2D. Consider the domain $\Omega = [0, 1]^2$, with a refined approximation in elements in $[0, 0.5] \times [0, 1]$, with refinement factor $m = 4$, and a standard approximation in elements in $[0.5, 1] \times [0, 1]$. Continuity on $\Gamma = \{x = 0.5\} \cap \Omega$ is

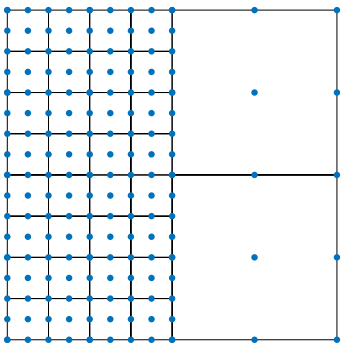

Figure 3.4: *Convergence in 2D.* Coarsest discretization in Ω for degree $p = 2$ and refinement factor $m = 4$. Blue dots indicate the nodes.

imposed using Nitsche's method. We study the convergence when refining the background mesh, maintaining m fixed. Figure 3.4 shows the coarsest discretization for degree $p = 2$.

For the equilibrium equation, we set the source term and Dirichlet boundary conditions on $\partial\Omega$ such that the analytical solution is

$$\boldsymbol{u}(x, y) = \begin{pmatrix} \sin(3x + y) \\ \cos(x + 3y) \end{pmatrix}, \tag{3.10}$$

with $d(x, y) = \dfrac{\sin(x + y) + 1}{5}$. The parameters are $E = 20$ GPa and $\nu = 0.18$. Figure 3.5 (left) shows the convergence plot in this case for degrees of approximation p, in agreement with the theoretical orders.

For the damage equation, the boundary conditions and the source term $\mathcal{H}^+$ are set accordingly to the analytical solution

$$d(x, y) = \frac{\sin(3x + y) + 1}{3},$$

with $G_C = 2.7 \cdot 10^{-3}$ kN/mm and $l = 0.01$ mm. Convergence plots are depicted in Figure 3.5 (right), again exhibiting optimal orders of convergence.

Convergence in 3D. Analogously, we now consider the domain $\Omega = [0, 1]^3$, which is discretized with refined elements for $\{x < 0.5\}$ and with standard elements for $\{x > 0.5\}$. Thus, $\Gamma = \{x = 0.5\} \cap \Omega$. The refinement factor is $m = 4$.

For the equilibrium equation, the analytical solution is

$$\boldsymbol{u}(x, y, z) = \begin{pmatrix} \sin(3y + z) \\ \sin(x + 3z) \\ x^6 + 2 \end{pmatrix},$$

with $d(x,y) = \dfrac{\sin(x+y+z)+1}{5}$, $E = 20$ GPa and $\nu = 0.18$. The expected orders of convergence are obtained, as can be seen in Figure 3.6 (left).

For the damage equation, we study the convergence to the solution

$$d(x,y,z) = \frac{\sin(3x+2y+z)+1}{3},$$

with $G_C = 2.7 \cdot 10^{-3}$ kN/mm and $l = 0.01$ mm. Results are displayed in Figure 3.6 (right), showing optimal convergence.

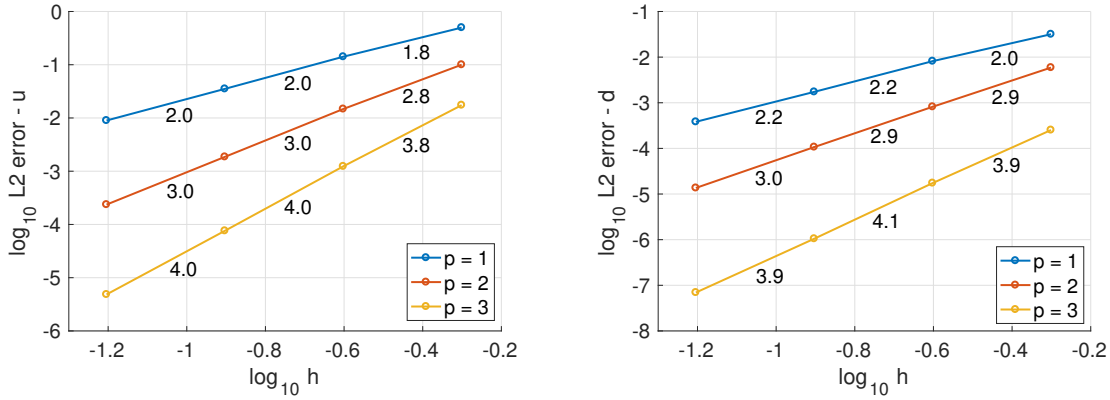

Figure 3.5: *Convergence in 2D.* Convergence plot for the displacement $\boldsymbol{u}$ (on the left) and for the damage d (on the right), for degrees $p = 1, 2, 3$ and Nitsche's parameters $\alpha_{\mathrm{E}} = 100$ and $\alpha_{\mathrm{D}} = 100$, respectively.

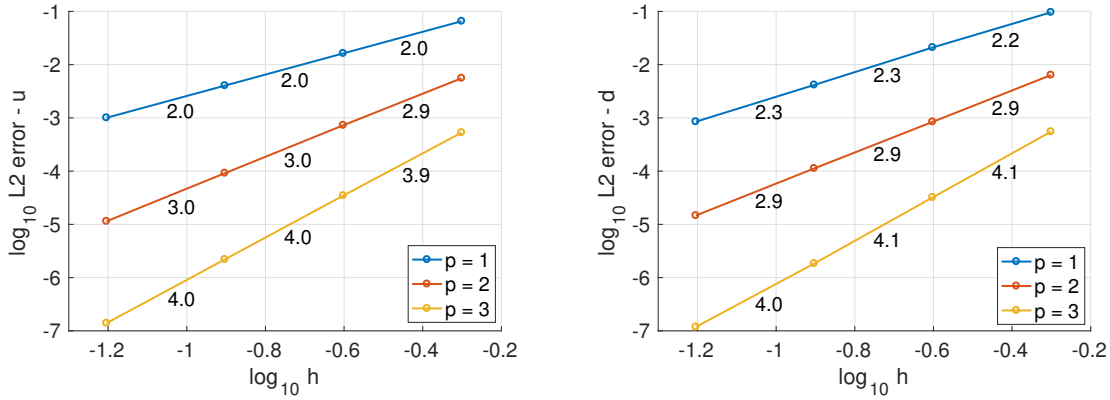

Figure 3.6: *Convergence in 3D.* Convergence plot for the displacement $\boldsymbol{u}$ (on the left) and for the damage d (on the right), for degrees $p = 1, 2, 3$ and Nitsche's parameters $\alpha_{\mathrm{E}} = 100$ and $\alpha_{\mathrm{D}} = 100$, respectively.

3.2.4 Choice of Nitsche's parameter

The effect of parameter α in the Nitsche's formulations is explored next. The good behavior of the method with respect to this parameter enables to easily choose a proper value. We focus on the equilibrium equation in 2D. However, the conclusions are extendable to other cases.

Assume the parameters and the analytical solution for the convergence test in (3.10). The domain is discretized with the third mesh, with element size $h = 0.125$, refining elements in $\{x < 0.5\}$ with refinement factor $m = 4$. Figure 3.7 shows the variations in L^2 error for values of $\alpha_{\mathrm{E}} \in [10^{-2}, 10^{3}]$, for degrees $p = 1, 2, 3$.

For all degrees, we observe that there is a critical value $\alpha^{p}_{\mathrm{min}}$ such that the solution is stable for any $\alpha > \alpha^{p}_{\mathrm{min}}$. Moreover, the plots also show that for $\alpha > \alpha^{p}_{\mathrm{min}}$ the accuracy does not depend on the particular value of α, exhibiting a very robust behavior on the parameter. On the other hand, values of α below this critical value provide solutions that are clearly wrong just by visual inspection, making the tuning of α an easy task. Note that the critical value increases with the degree of approximation. As a safe value, we take $\alpha = 100$ in all simulations.

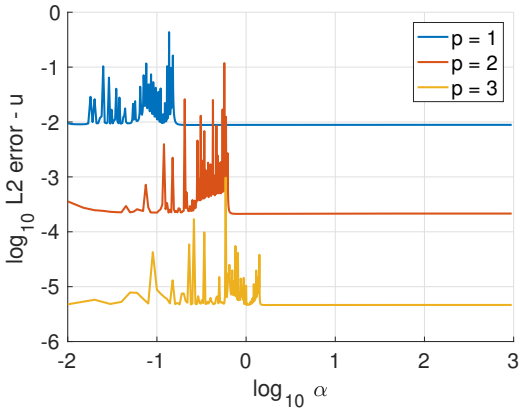

Figure 3.7: *Equilibrium equation in 2D.* Error of the formulation for different values of Nitsche's parameter α_{E}.

3.3 Numerical experiments

In this section, we present several experiments to validate the performance of the proposed strategy, both in 2D and 3D. The goal of these examples is to show the robustness of the methodology to capture complex crack patterns with a coarse and

fixed background mesh during all the simulation, while the discretization is dynamically refined along cracks.

In all two-dimensional examples, plane strain conditions are assumed for the equilibrium equation. The restoring of stiffness under compression in equation (1.14c) is only necessary for the branching test in Subsection 3.3.3. In the other examples, the degradation function is $g(d) = (1-d)^2$ in the whole domain. Preexisting cracks which are described as smeared damage bands are introduced by an initial history field variable, $\mathcal{H}_0^+$, following Borden et al. [2012]. The tolerance for convergence of the damage field d in the staggered scheme is fixed to 10^{-2}. The parameters in the Nitsche's formulation for both equations are $\alpha_{\mathrm{E}} = \alpha_{\mathrm{D}} = 100$.

3.3.1 Shear test

For this test, the configuration of the domain and the material parameters are taken as in Section 2.3.1, following Ambati et al. [2015]. The length-scale parameter is $l = 0.015$ mm. The loading process takes increments $\Delta u_D = 10^{-4}$ mm and the degree of approximation is $p = 1$.

First, we compare the solution obtained applying the refinement strategy with a reference solution computed on a globally refined mesh. The problem is solved on uniform quadrilateral background meshes with 48×48, 24×24 and 12×12 elements, with respective refinement factors $m = 5, 10$ and 20. The reference solution is computed on a mesh with 240×240 elements. Note that all discretizations have the same element size along the crack. The four elements surrounding the initial crack tip are refined in the preprocess for all discretizations.

Figure 3.8 shows the damage field at three load steps for the discretizations with initial meshes of 48×48 and 24×24 elements, for refinement value $d_{\mathrm{ref}} = 0.2$. Refined elements are highlighted with white edges. As the crack propagates, a narrow band of elements along the crack is refined.

The agreement between the reference solution, using a globally refined mesh, and the considered discretizations with automatic refinement can be seen in the contour plots in Figure 3.9. The corresponding load-displacement curves are plotted in Figure 3.10. For the mesh with 12×12 elements, the crack path obtained differs from the other ones. This can be explained by the inaccuracy of the background mesh to resolve the mechanical problem in the nonrefined region. The resulting crack path for the reference mesh is very similar to those for the 48×48 and the 24×24 meshes.

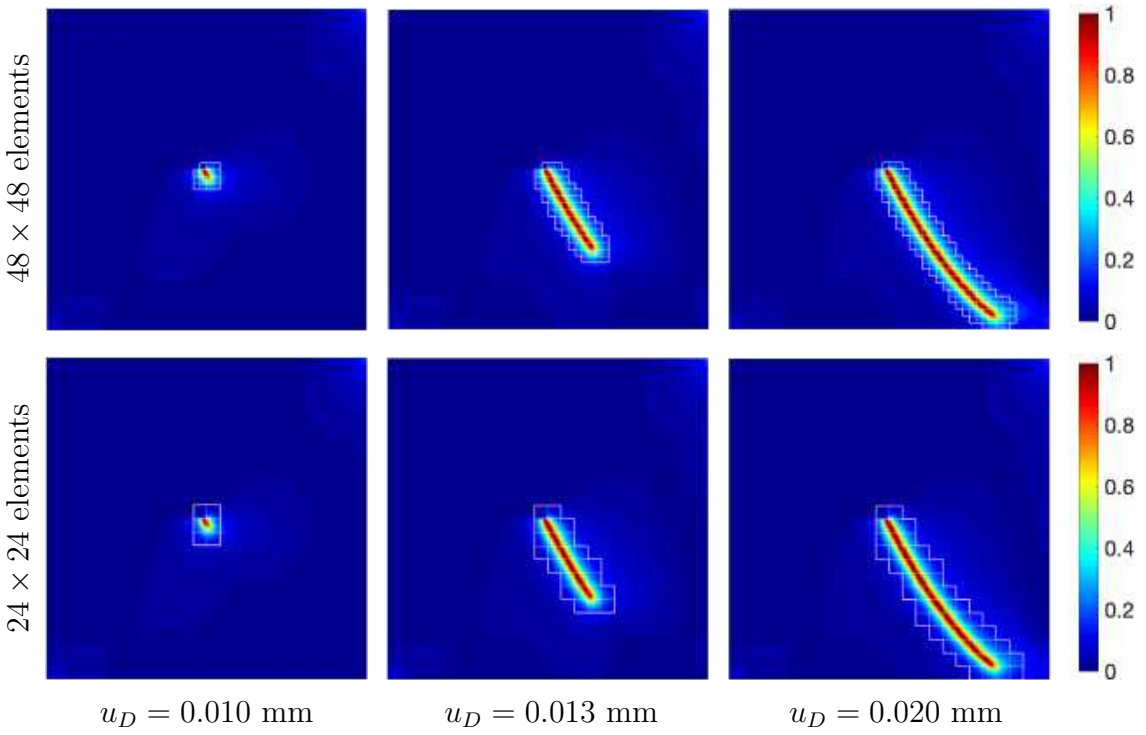

Figure 3.8: *Shear test.* Damage field at imposed displacements u_D, for degree $p = 1$ and refinement value $d_{\text{ref}} = 0.2$.

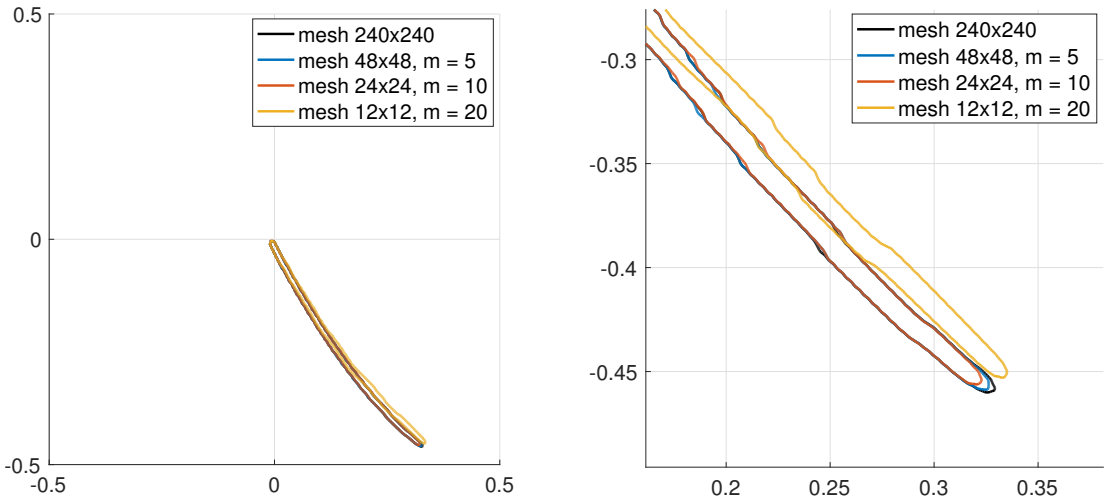

Figure 3.9: *Shear test.* Contour plot for damage value $d = 0.9$, at imposed displacement $u_D = 0.020$ mm with refinement value $d_{\text{ref}} = 0.2$. Zoom at the crack tip on the right.

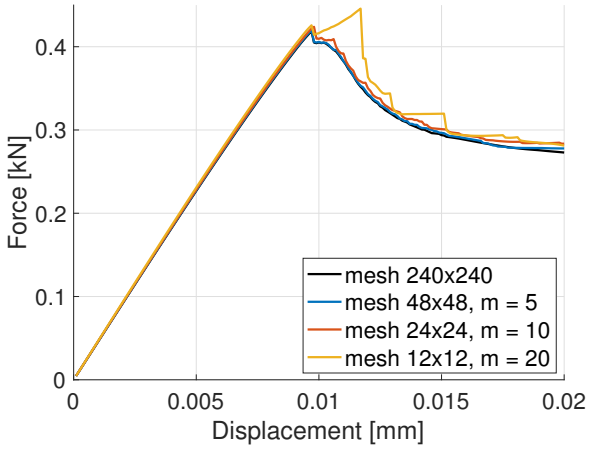

Figure 3.10: *Shear test.* Load-displacement curve, for degree of approximation $p = 1$ and refinement value $d_{\text{ref}} = 0.2$.

We can observe again, now in a CG framework, that a very local refinement along cracks is enough to capture the solution. This example demonstrates the robustness of the strategy to automatically adapt the discretization. Also, the refinement criterion based on the value of d performs as expected.

Now, we study the influence of the refinement factor d_{ref}, this is, the threshold value activating the refinement of elements. Consider the discretization with 24×24 elements and refinement factor $m = 10$. For refinement values $d_{\text{ref}} = 0.1, 0.2, 0.5$ and 0.7, we plot the load-displacement curves in Figure 3.11. The kinks coincide with the refinement of elements, this is, they are corrections once the accuracy of the discretization increases. According to the results, a value for d_{ref} between 0.1 and 0.2 gives accurate results, with a narrow band of refinement along the crack.

The saving in degrees of freedom for adaptive discretizations is also remarkable. Table 3.1 lists the number of degrees of freedom for each one of the discretizations at the beginning and at the end of the simulation, for refinement values $d_{\text{ref}} = 0.1$ and 0.2. With the proposed strategy, we are able to obtain accurate results with about $10 - 15\%$ of degrees of freedom of the globally refined mesh. Notice that for the coarser mesh, with 12×12 elements, the percentage of degrees of freedom is higher than for the other two adaptive discretizations. This is due to obtaining a wider refined zone in the mesh. Depending on the accuracy needed, one has to find a compromise between the background mesh, the refinement factor m and the refinement value d_{ref} to attain a feasible computational cost.

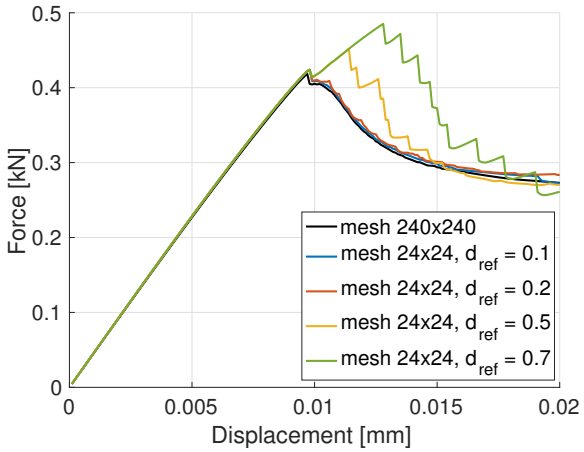

Figure 3.11: *Shear test.* Load-displacement curve for refinement factors d_{ref}. Mesh with 24×24 elements, refinement factor $m = 10$ and degree $p = 1$.

Table 3.1: *Shear test.* Degrees of freedom of the equilibrium problem for the various discretizations

Mesh	m	d_{ref}	Initial #dof	Final #dof	%
240×240	–	–	115 438	115 438	100
48×48	5	0.1	4 904	17 626	15.3
		0.2	4 904	12 804	11.1
24×24	10	0.1	2 074	17 108	14.8
		0.2	2 074	11 738	10.2
12×12	20	0.1	3 698	22 350	19.4
		0.2	3 698	16 722	14.5

3.3.2 Notched plate with a hole

This test was proposed by Ambati et al. [2015]. The set-up and the material parameters are detailed in Section 2.3.3. With this example, we want to test the performance of our adaptivity approach for a nonstructured mesh.

We use $l = 0.5$ mm, and take load increments of $\Delta u_D = 10^{-3}$ mm. We consider a quadrilateral mesh with element size $h \simeq 5$ mm, necessarily nonstructured to fit the geometry of the specimen, with degree of approximation $p = 4$ and refinement factor $m = 10$. Recall that the geometry of the domain is described by this background mesh during all the simulation. Elements containing the initial crack are refined from the beginning. Then, refinement is triggered by threshold value $d_{\text{ref}} = 0.2$.

Figure 3.12 displays the crack pattern for some load steps and Figure 3.13, the

corresponding load-displacement curve. The solution agrees with the adaptive HDG solution in Section 2.3.3. The crack horizontally propagates down to the hole and develops on the other side as elements are accordingly refined. As can be clearly observed in the load-displacement curve, these propagations are quite abrupt as expected in brittle fracture. This behavior corroborates the need for applying the refinement criterion at every staggered iteration. Again, the obtained results manifest the good performance of the strategy, here for a higher degree of approximation and a more complex scenario.

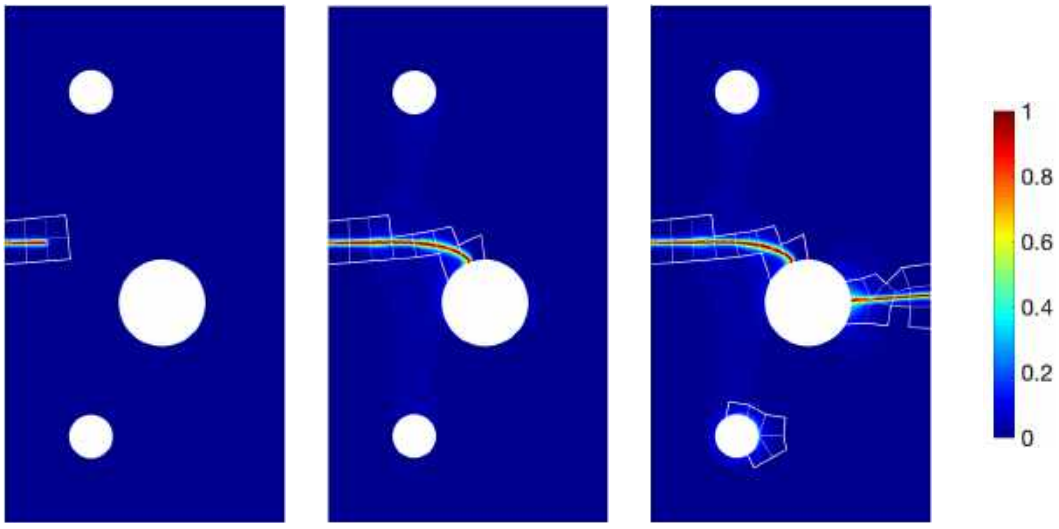

$u_D = 0$ mm $u_D = 0.4$ mm $u_D = 1.05$ mm

Figure 3.12: *Plate with a hole.* Damage field at imposed displacements u_D. Nonstructured mesh with element size $h \simeq 5$ mm, degree of approximation $p = 4$ and refinement factor $m = 10$.

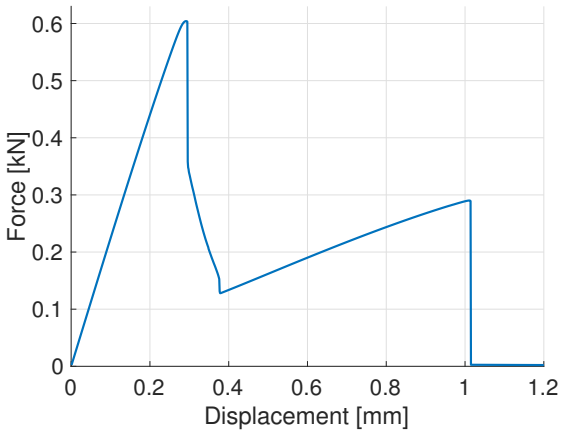

Figure 3.13: *Plate with a hole.* Load-displacement curve, for degree of approximation $p = 4$ and refinement factor $m = 10$.

3.3.3 Branching test

In order to test the ability of the strategy to properly capture cracks that bifurcate, we revisit the branching test proposed in Section 2.3.4. It offers a setting for crack branching in the quasi-static regime, with no heterogeneities in the material, thanks to imposed vertical displacements on the top and bottom edges of the piece following a parabolic function.

The numerical length-scale parameter is $l = 0.01$ mm and the refinement value is $d_{\text{ref}} = 0.2$. The loading process takes increments $\Delta u_D = 5 \cdot 10^{-5}$ mm. The specimen is discretized into a quadrilateral uniform mesh of 45×45 elements and refinement factor $m = 15$, with degree of approximation $p = 1$.

As depicted in Figure 3.14, the initial crack propagates horizontally and branches before reaching the right edge. The load-displacement curve is in Figure 3.15. Due to the bending caused by the imposed displacements, the damage field reaches the refinement value d_{ref} in elements on the left corners of the domain. The adaptive strategy enables to capture the branching maintaining the symmetry of the solution.

With this example, we can illustrate the role of the hybrid condition in equation (1.14c) of the model. If elastic stiffness is not restored under compression, we observe interpenetration of faces near the branching point when branches propagate. In Figure 3.16 we plot the deformed mesh at load step $u_D = 0.075$ mm in two cases: taking $g(d) = (1-d)^2$ in all the domain, and restoring $g(d)$ to 1 in compressed regions as stated in (1.14c). Although we obtain crack branching in both cases, a slight interpenetration of faces can be observed if the hybrid condition is not implemented.

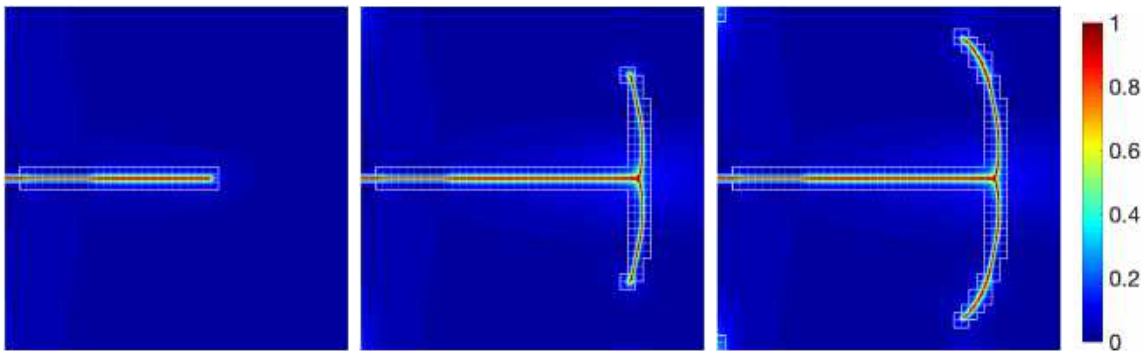

$u_D = 0.02$ mm $\qquad$ $u_D = 0.059$ mm $\qquad$ $u_D = 0.095$ mm

Figure 3.14: *Branching test.* Damage field at different load steps. Degree of approximation $p = 1$ and refinement factor $m = 15$.

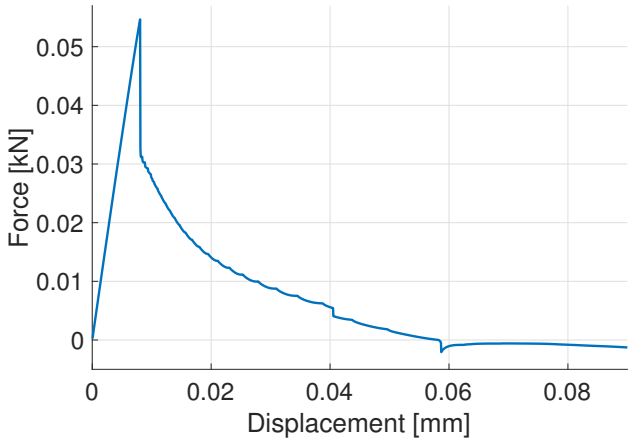

Figure 3.15: *Branching test.* Load-displacement curve, for degree $p = 1$ into a 45×45 mesh with refinement factor $m = 15$.

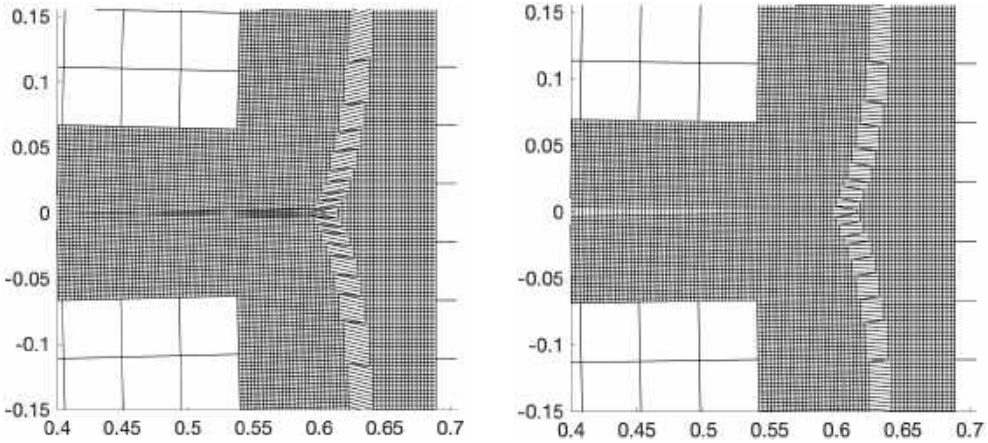

Without hybrid condition With hybrid condition

Figure 3.16: *Branching test.* Zoom of the deformed discretization at the branching point, with and without imposing the hybrid condition in equation (1.14c), at load step $u_D = 0.075$ mm for a mesh with 45×45 elements, $m = 15$ and $p = 1$.

3.3.4 Multiple cracks test

This test is inspired by the multiple-cracked plate test by Budyn et al. [2004]. It exemplifies a case for which an automatic refinement of the discretization is crucial.

We consider a square plate occupying the domain $[0, 2]^2$ mm^2, with six pre-existing cracks, loaded with prescribed displacements as shown in Figure 3.17. The tips of the initial cracks are reported in Table 3.2. The parameters are $E = 20$ GPa, $\nu = 0.3$, $G_C = 10^{-3}$ kN/mm and $l = 0.012$ mm, with applied increments of $\Delta u_D = 5 \cdot 10^{-5}$

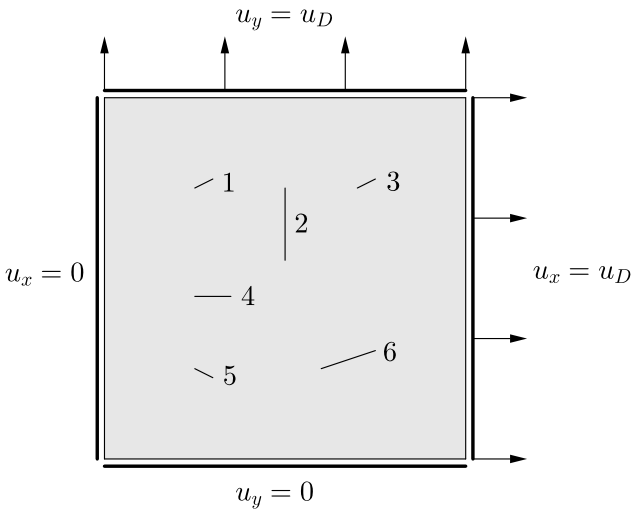

Figure 3.17: *Multiple cracks test.* Domain and boundary conditions.

Table 3.2: *Multiple cracks test.* Tip coordinates for the initial cracks in the domain $[0, 2]^2$ mm^2.

Crack	P_1 (mm)	P_2 (mm)
1	$(0.5, 1.5)$	$(0.6, 1.55)$
2	$(1, 1.1)$	$(1, 1.5)$
3	$(1.4, 1.5)$	$(1.5, 1.55)$
4	$(0.5, 0.9)$	$(0.7, 0.9)$
5	$(0.5, 0.5)$	$(0.6, 0.45)$
6	$(1.2, 0.5)$	$(1.5, 0.6)$

mm. We use a uniform mesh of 40×40 elements, with degree of approximation $p = 2$, refinement factor $m = 10$ and $d_{\text{ref}} = 0.2$.

In this case, cracks propagate coalescing between them. Applying the proposed strategy, we are able to capture crack propagation until the piece has broken into four independent pieces. Figure 3.18 shows the evolution of the crack pattern for some imposed displacements; each one of them corresponds to an abrupt growth of one of the cracks. The respective load-displacement curves, for both the horizontal and the vertical loads, F_x and F_y, are in Figure 3.19. Notice that all abrupt propagations coincide with a force drop in the load force. The piece loses the horizontal stiffness once a vertical crack crosses the whole plate, at $u_D = 0.015$ mm. The vertical stiffness is also lost at the end of the process, when the piece is completely broken apart. The complete evolution of the cracks propagation and of the automatic refinement can be seen in the YouTube video in Muixí et al. [2019b].

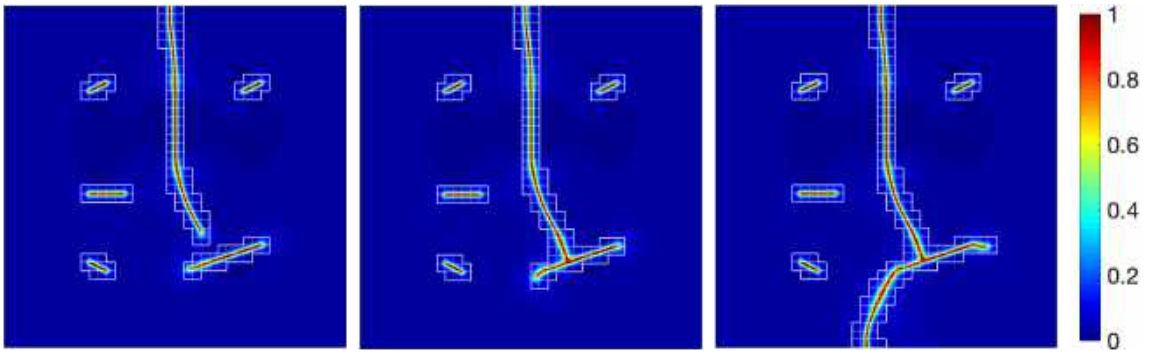

$u_D = 0.0125$ mm $u_D = 0.0137$ mm $u_D = 0.0150$ mm

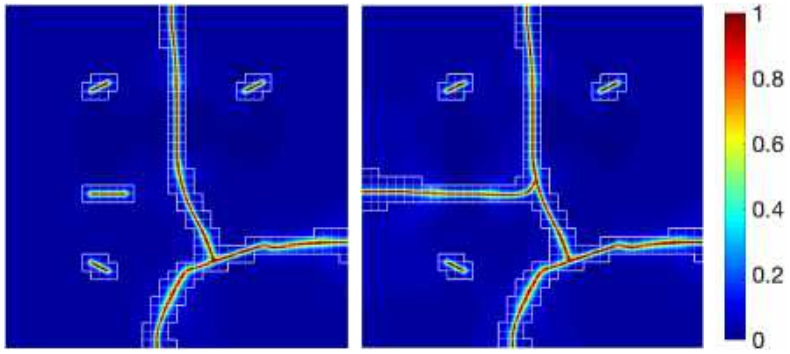

$u_D = 0.0195$ mm $u_D = 0.0271$ mm

Figure 3.18: *Multiple cracks test.* Damage field at different load steps. Degree of approximation $p = 2$, refinement factor $m = 10$ and $d_{\text{ref}} = 0.2$ on a 45×45 quadrilateral mesh.

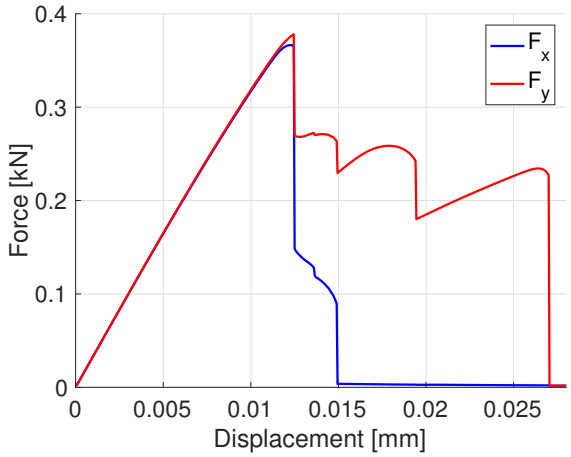

Figure 3.19: *Multiple cracks test.* Load-displacement curve. Degree $p = 2$, $m = 10$ and $d_{\text{ref}} = 0.2$ on a 45×45 quadrilateral mesh. F_x and F_y denote the horizontal and the vertical loads, respectively.

This example highlights the reliability of the strategy for cases in which the refined zones are scattered in the domain. The union of refined groups of elements and the corresponding rearrangement of interface faces, where Nitsche's method is applied, properly capture the fracture process.

3.3.5 Twisting crack in a 3D beam

Finally, we test the performance of the strategy for a 3D setting. Consider a beam with square section $\Omega = [0, 125] \times [0, 25] \times [0, 25]$ mm^3 as shown in Figure 3.20. The piece has two inclined notches with opposite angles, on faces $\{y = 0 \text{ mm}\}$ and $\{y = 25 \text{ mm}\}$. The beam is clamped on $\{x = 0 \text{ mm}\}$ and has imposed displacements in the x direction on the face $\{x = 125 \text{ mm}\}$. Because of the orientation of the notches, this example cannot be reduced to a 2D approximate configuration.

The parameters are $E = 32$ GPa, $\nu = 0.25$, $G_C = 1.6 \cdot 10^{-4}$ kN/mm and $l = 2$ mm. The loading process takes increments $\Delta u_D = 5 \cdot 10^{-4}$ mm.

We consider a uniform mesh of hexahedra with element size $h = 5$ mm. The degree of approximation is $p = 2$ and the refinement factor is $m = 5$. Refinement is activated with threshold value $d_{\text{ref}} = 0.2$. We model the initial notches as damage bands and refine the elements containing them in the preprocess.

The resulting damage field is shown in Figure 3.21. Inital cracks coalesce, with

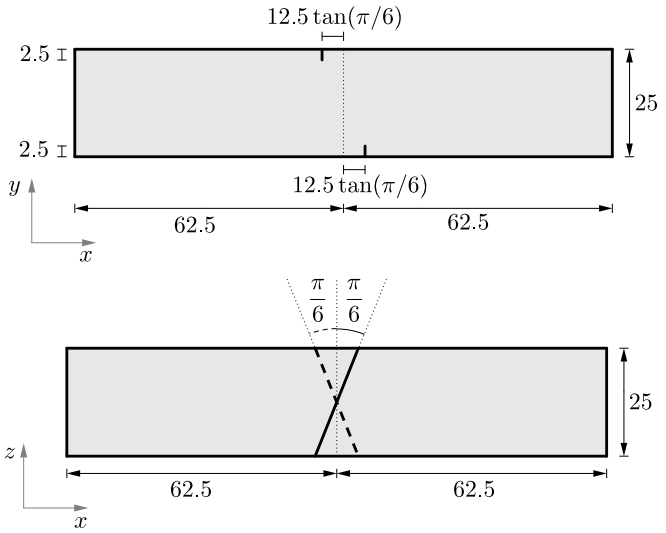

Figure 3.20: *Twisting crack test.* Geometry seen from the plane $\{z = 0\}$ and from $\{y = 25\}$. Continuous line indicatess the notch on $\{y = 25\}$ and the dashed line, the notch on $\{y = 0\}$. Dimensions in mm, angles in rad.

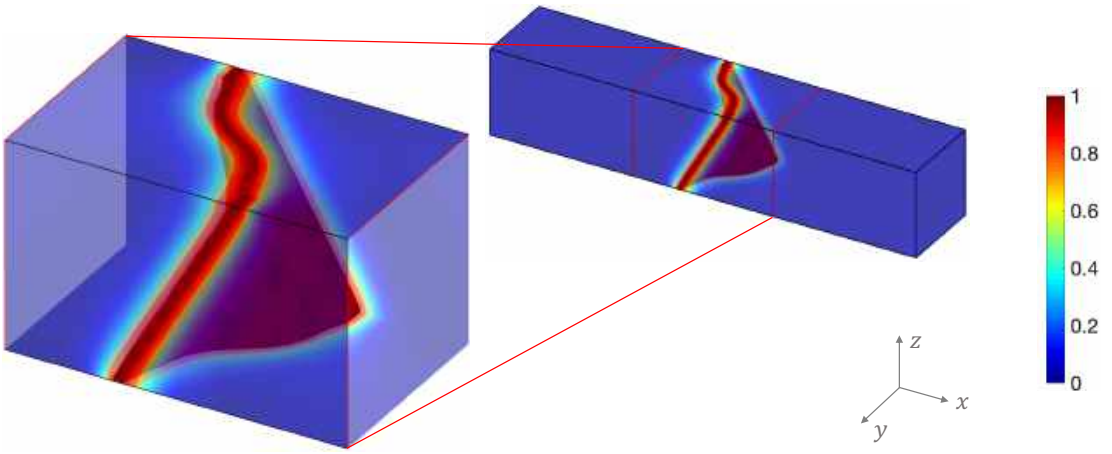

Figure 3.21: *Twisting crack test.* Crack path obtained at imposed displacement $u_D = 0.066$ mm. The piece is discretized into a hexahedral mesh with $h = 5$ mm, degree $p = 2$, refinement factor $m = 5$ and $d_{\text{ref}} = 0.2$.

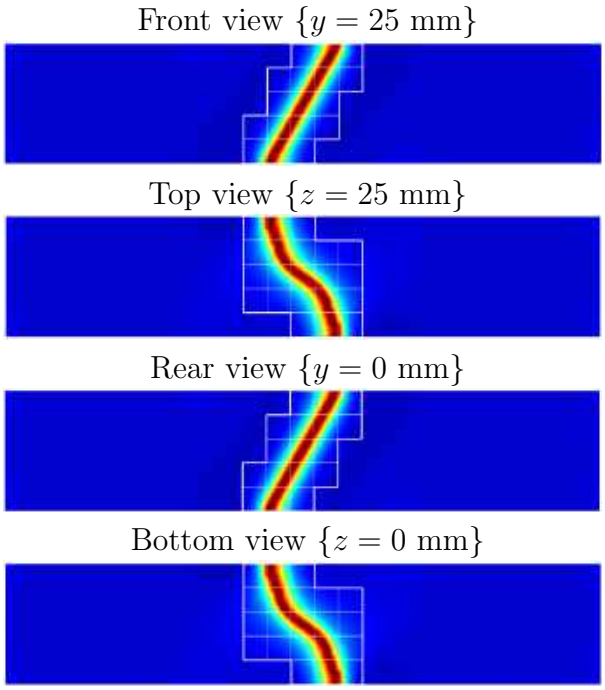

Figure 3.22: *Twisting crack test.* Crack path seen from the exterior faces of the piece for $u_D = 0.066$ mm. Degree $p = 2$ and refinement value $d_{\text{ref}} = 0.2$.

a twisting to match the opposite inclinations of the notches. In Figure 3.22 we plot the crack path as seen from the exterior faces of the beam. We observe the expected symmetry with respect of rotations of the piece around the x-axis. The mesh is refined in a narrow band containing the crack. The load-displacement curve is in Figure 3.23

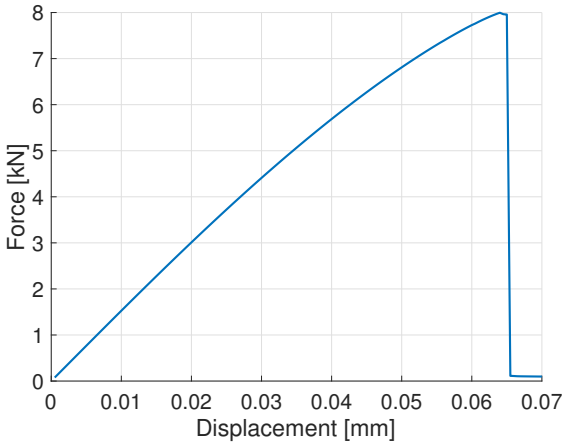

Figure 3.23: *Twisting crack test.* Load-displacement curve, for a uniform mesh with $h = 5$ mm and degree $p = 2$, refinement factor $m = 5$ and refinement value $d_{\text{ref}} = 0.2$.

and indicates that the specimen is completely broken at a single load step.

This example illustrates the ability of the strategy to simulate cracks also in 3D, where more computational resources are needed and adaptivity is a key part of the procedure.

3.4 Conclusions

In this chapter, a novel adaptive refinement strategy for phase-field models of brittle fracture has been presented. A partition of the mesh in standard and refined elements is updated at every iteration of the staggered scheme. In each region (standard and refined), we use a classical CG approximation. Then, on the interface between regions, continuity between different discretization spaces is imposed in weak form by means of Nitsche's method. Weak continuity implies that there are no hanging nodes nor transition elements. The discretization is automatically refined in narrow bands along cracks and shows no refinement spreading.

Regarding the choice of the Nitsche's parameter, the formulation is stable for a wide range of values. A lower bound of this parameter may be rigorously obtained by solving an eigenvalue problem. However, according to our experience, finding a suitable value by numerical experimentation is rather straightforward.

The accuracy and robustness of the strategy has been illustrated through several numerical examples, both in 2D and 3D. The method has been tested for complex

scenarios, such as crack branching and coalescence, for high orders of approximation and for refinement factors up to $m = 20$. In all the cases, the analysis is successfully carried out without any a priori information about the crack path required for the definition of the background mesh.

The strategy can be easily added to an existing finite element code for phase-field and can be analogously applied to other phase-field models of fracture.

If compared to the adaptive strategy based on HDG proposed in Chapter 2, the two options are robust and lead to a very local refinement. However, the new approach has a lower computational cost, becoming more suitable for demanding simulations, such as 3D tests. Thus, the CG strategy is our choice for the next chapter, in which the adaptive refinement is combined with XFEM.

Chapter 4

A combined XFEM phase-field computational model[1]

The adaptive strategies for phase-field models proposed in Chapters 2 and 3 are two robust alternatives for locally refining the discretization as cracks propagate. The adaptive refinement presents an important reduction of the computational cost when compared to a uniform refinement in the whole domain. However, the cost can be further reduced by derefining the elements in the wake of crack tips, where crack paths do not change, by replacing the diffuse cracks by sharp cracks, via an XFEM coarser discretization.

In this chapter, XFEM and the adaptive phase-field model based on Nitsche's method from Chapter 3 are combined in a new method that has the computational efficiency of XFEM, and also the ability of phase-field models to handle crack evolution. The presented methodology is stated, coded and tested in 2D and 3D.

Phase-field is used in small subdomains around crack tips, where the discretization is uniformly h-refined to capture the solution, and the discontinuous model is used in the rest of the domain. Crack-tip subdomains move with the crack tips in a fully automatic process. Nitsche's method handles the very local and non-conformal refinement for any refinement factor. The critical issues are the gluing of the two representations of cracks (sharp and diffuse) on the interface between subdomains, and the location of sharp cracks within the diffuse bands.

[1]This chapter is based on Muixí et al. [2020b].

The combined computational model could also be formulated within the HDG adaptive strategy in Chapter 2. Indeed, it is possible to enrich the HDG discretization to represent sharp discontinuities with an XFEM philosophy, as proposed in the eXtended HDG method by Gürkan et al. [2017]. Here, we focus on the adaptivity based on Nitsche's method because it is formulated in a continuous FEM setting, with a simpler structure of the code and a lower computational cost.

Section 4.1 describes the idea behind the combined computational model. In Section 4.2 we give the FE formulation, together with some implementation details. Sections 4.3, 4.4 and 4.5 are devoted to the evolution of the crack-tip subdomains and the transition to fracture as cracks propagate. In Section 4.6, we present some representative numerical examples in 2D and a fully 3D test to show the capabilities of the strategy. The chapter is closed with the conclusions in Section 4.7.

4.1 The concept: sharp cracks with phase-field crack tips

A novel computational model combining a phase-field model and an XFEM discontinuous approach is proposed. The phase-field equations are solved in small subdomains around crack tips, Ω_{tips}, and the discontinuous model is used in the rest of the domain, Ω_{xfem}. The corresponding diffuse and sharp definitions of cracks are not overlapped and we denote by Γ the interface between subdomains, this is,

$$\overline{\Omega} = \overline{\Omega_{\text{tips}}} \cup \overline{\Omega_{\text{xfem}}},\ \Omega_{\text{tips}} \cap \Omega_{\text{xfem}} = \emptyset,\ \Gamma = \overline{\Omega_{\text{tips}}} \cap \overline{\Omega_{\text{xfem}}}.$$

The model overcomes the limitations of both approaches. The phase-field model drives the crack propagation and deals with branching and merging of cracks, whereas the crack is explicitly described in almost all the domain by a sharp discontinuity. Thus, the high spatial resolution needed around crack paths in standard phase-field models is now only necessary in small neighborhoods of the crack tips, with the consequent important saving in computational cost.

The partition of the domain is based on the computational mesh. Crack-tip subdomains Ω_{tips} are defined as the set of elements close to crack tips and tips of notches in the domain, where crack growth is expected. The rest of elements are Ω_{xfem}. The initial definition of Ω_{tips} is crucial to detect crack inception, since the damage field is solved only in this part of the domain.

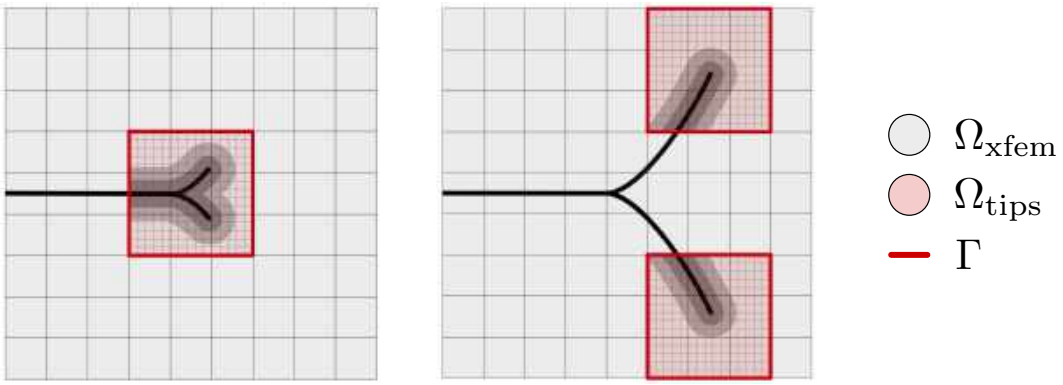

Figure 4.1: Scheme of a discretization in two consecutive load steps. In Ω_{tips}, elements are uniformly h-refined and cracks are represented by diffuse bands. The FE discretization in Ω_{xfem} is the one corresponding to the initial mesh, with an XFEM Heaviside enrichment to introduce sharp cracks, represented with black line. The interface Γ is depicted in red.

As crack tips advance during the computation, the domains Ω_{tips} and Ω_{xfem} are repeatedly updated, refining elements in the nose of the cracks and derefining elements in their wake. When derefining, diffuse cracks are replaced by XFEM sharp traction-free cracks.

Following the concept in Chapter 3, elements in Ω_{tips} are automatically identified and uniformly refined to properly approximate the phase-field solution, now only around crack tips. The refinement is based on a refined reference element, keeping the original background mesh during the whole computation.

Figure 4.1 illustrates the discretizations for two consecutive load steps. The elements in Ω_{tips} are h-refined with a uniform submesh with $m^{n_{sd}}$ subelements. The refinement factor m is chosen a priori depending on the length-scale parameter l of the phase-field model. As the crack evolves, the small subdomains move with the crack tips and the diffuse band becomes a sharp discontinuity in the wake of the crack.

The main challenge is gluing the two models on the interface Γ, with different discretizations and representations of cracks on each side.

For the equilibrium equation, continuity of the displacement is imposed in weak form by means of Nitsche's method. The Nitsche's formulationis the one considered in Section 3.2, but now with an XFEM enriched approximation in Ω_{xfem}. In addition, when imposing continuity, a small portion of the interface around the intersections with the crack is discarded.

Numerical experiments show that unrealistic displacement fields are obtained if the continuity is enforced on the whole interface Γ. The reason is that the description of the crack on both sides of the interface is different. From Ω_{xfem} the crack is sharp and the material retains all the stiffness, whereas on Ω_{tips} we have a smooth representation of the crack with a material degradation given by $g(d)$, leading to almost fully damaged material close to the crack path. Thus, for parts of Γ which are crossed by cracks, the difference of stiffness between the two subdomains is quite significant.

Continuity is then enforced on a slightly cropped interface defined as

$$\widehat{\Gamma} = \{\boldsymbol{x} \in \Gamma : d(\boldsymbol{x}) < 0.9\}. \tag{4.1}$$

Figure 4.2 illustrates the concept. A simple test comparing the results obtained imposing continuity on Γ and on the cropped interface, $\widehat{\Gamma}$, is presented in Section 4.6.1.

It is worth noting that imposing continuity in weak form, by means of Nitsche's method, handles the non-conformal approximations in a natural way. That is, refined discretizations are directly attached to non-refined discretizations, with a standard finite element approximation or with XFEM enrichment. No transition elements are required, avoiding the spreading of the refinement or the enrichment, and without having to deal with hanging nodes.

The other important issue for gluing the computational models is setting proper boundary conditions for the damage variable d, since we solve for it only in Ω_{tips}. In standard phase-field models, the boundary conditions for the damage equation are

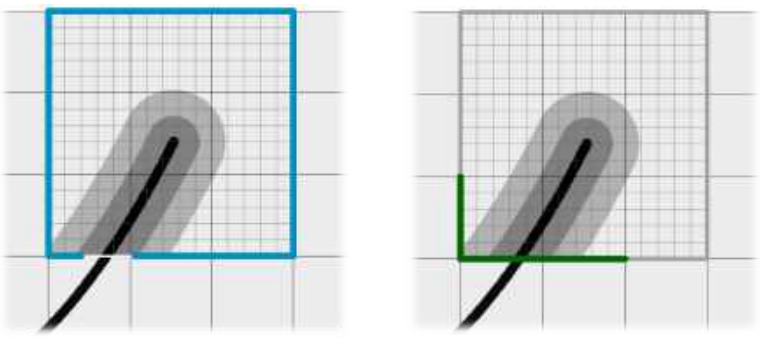

Figure 4.2: Continuity of displacements is imposed in weak form on the interface $\widehat{\Gamma}$, in blue (left). Cracks do not necessarily intersect Γ perpendicularly; Dirichlet boundary conditions for the damage field d are imposed on Γ_D^d, i.e. on the side intersected by the crack and on the adjacent sides, in green (right).

usually taken as homogeneous Neumann on $\partial\Omega$. However, we cannot assume that cracks intersect the interface Γ with perpendicularity. With this in mind, Dirichlet boundary conditions are imposed on the faces that have been crossed by a crack. More precisely, the Dirichlet boundary, Γ_D^d, consists of the element sides (in 2D, faces in 3D) on Γ that are cut by the crack, i.e. with $d > 0.95$ at some node, together with their neighboring faces on Γ. See an example in Figure 4.2 (right). When transitioning elements intersected by the crack from Ω_{tips} to Ω_{xfem}, the damage field on Γ_D^d is saved to be used as Dirichlet value for the damage equation. That is, the damage is assumed to be frozen in the wake of crack tips. On the rest of the boundary, $\partial\Omega_{\text{tips}} \setminus \Gamma_D^d$, homogeneous Neumann conditions are imposed not to favor any direction of crack growth.

4.2 Finite element formulation

In this section, we present the formulation, commenting also on some implementation details. In the equilibrium equation, the discretization has to account for discontinuous displacements across cracks in Ω_{xfem}. Also, continuity of displacements between Ω_{tips} and Ω_{xfem} has to be handled by the formulation. On the other hand, the damage equation is solved with the standard finite element method with refined approximation in Ω_{tips}.

4.2.1 Equilibrium equation: Nitsche's method

The equilibrium equation is solved in Ω, with different non-conformal approximations for the displacement field in the partition given by Ω_{tips} and Ω_{xfem}. Thus, the displacement is assumed to be in the space $[\mathcal{V}(\Omega)]^{n_{sd}}$ with

$$\mathcal{V}(\Omega) = \left\{ v \in L^2(\Omega) : \; v|_{\Omega_{\text{tips}}} \in H^1(\Omega_{\text{tips}}), v|_{\Omega_{\text{xfem}}} \in H^1(\Omega_{\text{xfem}} \backslash \Gamma_c) \right\},$$

which includes functions that are discontinuous across the interface Γ, and across the sharp crack Γ_c; the second one, handled by the XFEM enrichment.

Our choice to weakly impose continuity on the interface Γ is Nitsche's method, following the formulation in Section 3.2. The differences here are just the approximation spaces to be glued, now including sharp cracks via XFEM in the nonrefined regions, and the imposition of continuity on the cropped interface $\hat{\Gamma}$.

In this case, the weak form reads: find $\boldsymbol{u} \in [\mathcal{V}(\Omega)]^{n_{sd}}$ such that $\boldsymbol{u} = \boldsymbol{u}_D$ on Γ_D and

$$\begin{aligned} &\int_\Omega \boldsymbol{\nabla v} : \boldsymbol{\sigma}(\boldsymbol{u}) \, \mathrm{d}V - \int_{\widehat{\Gamma}} [\![\boldsymbol{v} \otimes \boldsymbol{n}]\!] : \{\boldsymbol{\sigma}(\boldsymbol{u})\} \, \mathrm{d}s - \int_{\widehat{\Gamma}} \{\boldsymbol{\sigma}(\boldsymbol{v})\} : [\![\boldsymbol{u} \otimes \boldsymbol{n}]\!] \, \mathrm{d}s + \\ &+ \beta_{\mathrm{E}} \int_{\widehat{\Gamma}} [\![\boldsymbol{u} \otimes \boldsymbol{n}]\!] : [\![\boldsymbol{v} \otimes \boldsymbol{n}]\!] \, \mathrm{d}s - \int_{\Gamma_N} \boldsymbol{v} \cdot \boldsymbol{t}_N \, \mathrm{d}s = 0, \end{aligned} \tag{4.2}$$

for all $\boldsymbol{v} \in [\mathcal{V}(\Omega)]^{n_{sd}}$ such that $\boldsymbol{v} = \boldsymbol{0}$ on Γ_D, where β_{E} is the Nitsche's stabilization parameter, and $\widehat{\Gamma}$ is almost the whole interface Γ, discarding small portions around the intersections with the cracks, as defined in (4.1) and illustrated in Figure 4.2.

Even though it has been omitted for simplicity, note that the stress tensor $\boldsymbol{\sigma}$ in (4.2) depends also on the damage field d in Ω_{tips}.

Recall that the stability of the formulation depends on the value of β_{E}, which is again taken as (3.6). The formulation is very robust with respect to the parameter and the value of α_{E} can be easily tuned by numerical experimentation, as studied in Section 3.2.4.

4.2.2 Spaces of approximation: XFEM and refined

The computation is based on a fixed background mesh during the whole simulation, with elements $\{K_i\}_{i=1}^{n_{el}}$ satisfying (2.1). As cracks evolve, in every load step and iteration of the staggered scheme, the elements in the background mesh are identified as refined, i.e. in Ω_{tips}, if they are close to crack tips or tips of initial notches, or in Ω_{xfem}, otherwise.

In Ω_{xfem}, the XFEM approximation is based on a standard finite element space, that is

$$\mathcal{V}^h(\Omega_{\mathrm{xfem}}) = \{v \in \mathcal{H}^1(\Omega_{\mathrm{xfem}}) : v|_{K_i} \in \mathcal{P}^p \text{ for } K_i \subseteq \Omega_{\mathrm{xfem}}\},$$

with nodal basis $\{N_i\}_{i \in I_{\mathrm{xfem}}}$, where I_{xfem} is the set of the indices of the nodes in Ω_{xfem} and $\mathcal{P}^p$ is the space of polynomials up to degree p. The XFEM approximation space in Ω_{xfem} in the case of a unique crack is then

$$\mathcal{V}^h_{\mathrm{xfem}} = < N_i >_{i \in I_{\mathrm{x}}} \otimes < HN_i >_{i \in I_{\mathrm{enr}}},$$

where I_{enr} is the set of indices of enriched nodes, i.e. the nodes of the elements which are cut by the crack, and H is the Heaviside function taking, for instance, values 1 and -1 on each side of the crack. In the presence of branching or several cracks, the

approximation is enriched with additional Heaviside functions

$$\mathcal{V}^h_{\text{xfem}} =< N_i >_{i\in I_{\text{x}}} \otimes < H^1 N_i >_{i\in I^1_{\text{enr}}} \otimes \ldots \otimes < H^{n_{\text{cracks}}} N_i >_{i\in I^{n_{\text{cracks}}}_{\text{enr}}},$$

where n_{cracks} is the total number of crack branches, see Moës et al. [1999]. Here, no asymptotic tip enrichment is necessary since Ω_{xfem} does not contain crack tips.

A proper numerical quadrature must be defined in the elements intersected by the crack to account for the discontinuity of the XFEM approximation. That is, a numerical quadrature must be defined in each portion of cut elements, see for instance Marco et al. [2015] and Gürkan et al. [2016].

On other hand, in Ω_{tips}, a uniformly h-refined discretization is considered to capture the sharp variation of the phase-field solution. These elements are mapped into a uniformly refined reference element, as described in Section 3.1. The resulting approximation space is equivalent to a standard finite element approximation on a finer mesh, non-conformal on the interface Γ. Again, the refinement factor m is known from the beginning, and can be taken using the parameters of the problem as defined in (2.15). The approximation space in Ω_{tips} is then defined as

$$\mathcal{V}^h_{\text{tips}} = \{v \in H^1(\Omega_{\text{tips}}) \ : \ v|_{K_i} \in \mathcal{P}^p_{\text{ref}}(K_i) \text{ for } K_i \subseteq \Omega_{\text{tips}}\},$$

where $\mathcal{P}^p_{\text{ref}}(K_i)$ is the refined space in each element. The element is sploit into $m^{n_{sd}}$ uniform subelements, and the refined approximation space in the element is

$$\mathcal{P}^p_{\text{ref}}(K_i) = \{v \in \mathcal{H}^1(K_i) : v|_{K_{ij}} \in \mathcal{P}^p(K_{ij}),\ j = 1...m^{n_{sd}}\},$$

with $\{K_{ij}\}_{j=1}^{m^{n_{sd}}}$ denoting the subelements in the element K_i.

Finally, the approximation space to discretize the Nitsche's weak form (4.2) is the combined space

$$\mathcal{V}^h(\Omega) = \{v \in H^1(\Omega) : v|_{\Omega_{\text{xfem}}} \in \mathcal{V}^h_{\text{xfem}},\ v|_{\Omega_{\text{tips}}} \in \mathcal{V}^h_{\text{tips}}\}.$$

4.2.3 Damage equation

The damage equation is solved only in Ω_{tips}, this is, in the small subdomains containing crack tips and tips of notches, where damage evolution is expected. As commented in Section 4.1, and illustrated in Figure 4.2 (right), Dirichlet boundary conditions are imposed on Γ^d_D, defined as a portion of the boundary around the intersection with

cracks. Homogeneous Neumann boundary conditions are imposed on the rest of the boundary.

The weak form is then: find $d \in \mathcal{H}^1(\Omega_{\text{tips}})$ such that $d = d_D$ on Γ_D^d and

$$\int_{\Omega_{\text{tips}}} \left(\frac{G_C}{l} + 2\mathcal{H}^+ \right) v d \, \mathrm{d}V + \int_{\Omega_{\text{tips}}} G_C l \boldsymbol{\nabla} v \cdot \boldsymbol{\nabla} d \, \mathrm{d}V \; = \int_{\Omega_{\text{tips}}} v 2\mathcal{H}^+ \, \mathrm{d}V, \tag{4.3}$$

for all $v \in \mathcal{H}^1(\Omega_{\text{tips}})$ such that $v = 0$ on Γ_D^d.

The value set on the Dirichlet boundary, d_D, is the value saved from the damage solution in previous iterations, assuming that the damage is frozen on the wake of the crack. The weak form is discretized with the refined approximation space $\mathcal{V}^h_{\text{tips}}$.

4.2.4 Staggered scheme

Numerical simulations take an incremental process in load steps. At every load step, the system is solved with a staggered scheme, for which the equations are solved alternately until convergence. For load step n, we iterate over:

i. *Computing the displacement field* $\boldsymbol{u}$ in Ω by solving the weak form (4.2), with the current damage field d in Ω_{tips}, and with boundary data $\boldsymbol{u}_D = \boldsymbol{u}_D^n$ on Γ_D and $\boldsymbol{t}_N = \boldsymbol{t}_N^n$ on Γ_N. Recall that traction-free conditions on the crack are imposed by means of the XFEM enrichment in Ω_{xfem}, and a refined discretization is considered in Ω_{tips}.

ii. Updating the history field $\mathcal{H}^+$ in Ω_{tips}.

iii. *Computing the damage field* d in Ω_{tips} by solving the weak form (4.3).

iv. *Updating the partition*, Ω_{tips} and Ω_{xfem}, and the geometrical description of sharp cracks, as detailed in Sections 4.2.5, 4.3.1 and 4.4.

As a convergence criterion we check if the error of the damage field in the Euclidean norm is lower than a certain tolerance.

Note that crack-tip subdomains are updated at every staggered iteration. Since we are modeling brittle fracture, cracks can significantly grow at a single load step and the phase-field subdomain has to be accordingly modified to allow the propagation.

4.2.5 Geometrical information

The geometry of the domain is defined by the background mesh (X, T), with X the nodal coordinates and T the connectivity matrix. This mesh is kept fixed during all the computation.

In the preprocess, information of the faces is computed from the connectivity matrix. Faces are numbered and, for each one of them, we store the number of the elements sharing the face and the local number of the face in each element. In 3D, the rotation is also stored, that is, which node in the face from the second element corresponds to the first node of the face from the first element. This information on faces is used to compute the integrals over $\hat{\Gamma}$ in the equilibrium weak form (4.2).

Information of the partition $\{\Omega_{\text{tips}}, \Omega_{\text{xfem}}\}$ is given by three vectors storing, respectively, the numbers of the elements in each subdomain and the numbers of the faces composing the interface Γ. Also, we need to save the list of nodes on Γ_D^d and the value of the damage field on these nodes from the previous iteration, to be able to impose the boundary conditions in (4.3). During the computation, information on the partition is updated at every staggered iteration according to the propagation of cracks by applying the criteria in Section 4.3.1.

A geometrical description of sharp cracks in Ω_{xfem} is needed to introduce the discontinuities into the XFEM discretization. Here, we store the crack path together with a nodal vector indicating whether each enriched node is in the left or right side of the crack. Some details on the construction of the sharp crack can be found in Section 4.4.

In addition, to ensure continuity of the approximation in the refined region Ω_{tips}, we define an auxiliary mesh $(X_{\text{ref}}, T_{\text{ref}})$ to facilitate the assembly of refined elements, as done in the adaptive strategy in Chapter 3. Again, this new mesh is constructed by mappings of the refined reference element into the elements in Ω_{tips}, and it is modified as the list of elements in Ω_{tips} is updated. When an element is added to Ω_{tips}, the nodes in the refined element are added to X_{ref}, avoiding repetitions, and the corresponding row is added to T_{ref}. Here, elements can be also supressed from Ω_{tips}. If this is the case, nodes not belonging to other refined elements are removed from X_{ref}, T_{ref} is modified according to the new nodal numbering and the row corresponding to the element is removed. The use of a refined mesh is optional, since the computations are directly done with the refined reference element.

4.3 Update of the partition

The criteria to decide if an element should be in Ω_{tips} or in Ω_{xfem} are based on *i)* the maximum value of the damage reached in the element, and *ii)* the distance to elements containing crack tips (or tips of notches). These criteria are applied at every iteration of the staggered algorithm.

In this section, we describe the criteria and also the algorithm to identify the elements that contain crack tips in 2D. The conversions from a phase-field to a sharp representation of cracks and vice versa are discussed in Sections 4.4 and 4.5.

4.3.1 Refining and switching criteria

The refining criterion is applied to elements in Ω_{xfem} which are adjacent to the interface Γ, in order to decide if they should be transferred to Ω_{tips}. Following the idea in the adaptive strategies in this thesis, see Sections 2.2.3 and 3.1.1, an element is refined if the damage field reaches a threshold value d_{ref} at one of its nodes. Here, since the damage is computed only in Ω_{tips}, an element in Ω_{xfem} is refined if any of its nodes on the interface reaches the threshold value d_{ref} and it is close to some element containing a crack tip, with a threshold distance δ_{ref}. This last consideration ensures that elements in the wake of cracks stay in Ω_{xfem}.

Then, to decide if some of the elements in Ω_{tips} have to switch to the discontinuous approximation, the distance criterion with threshold value δ_{ref} is also applied. More precisely, if the minimum distance of an element to all the elements containing a crack tip (or notch tip) is larger than δ_{ref}, the element is transferred to Ω_{xfem}.

Distances between elements are computed center-to-center. In practice, values of d_{ref} between 0.1 and 0.2 give accurate phase-field approximations with narrow bands of refinement along cracks, and a reasonable value for the distance threshold δ_{ref} is around $10l$.

4.3.2 Identification of elements containing crack tips

Here, we focus on quadrilateral elements in 2D. The logic of the algorithm is easily extendable to triangular elements. As a simplification, we assume a smeared crack can only intersect the same element edge once.

Elements containing crack tips are identified using the number of sides which are intersected by the smeared band and the area of the band inside the element. We

assume a side is intersected if it reaches $d > 0.95$ at some of its integration points. The area of the band is approximated as the sum of the weights of integration points in the element with $d > 0.95$.

First, for all elements in Ω_{tips}, we count how many sides are intersected by the crack. The considered configurations are summarized in Figure 4.3.

In elements with only 1 intersected side, we mark the element as containing a crack tip if the area of the band is larger than a threshold A^*; on the other case, the crack is assumed to be tangent to the side.

For 2 intersected sides, the element contains a crack tip if the two intersected sides are adjacent, the shared node satisfies $d > 0.95$ and the area of the band is larger than A^*. All other cases are discarded.

Elements with 3 o 4 intersected sides do not contain a crack tip.

The algorithm does not cover all possibilities. For instance, crack tips which are almost tangent to an element side may not be correctly identified. Robustness is ensured by saving the elements containing crack tips from the previous iteration. If a crack tip from the previous iteration disappears, i.e. it is not found in the same element and has not moved to a neighboring element, we assume the crack tip has

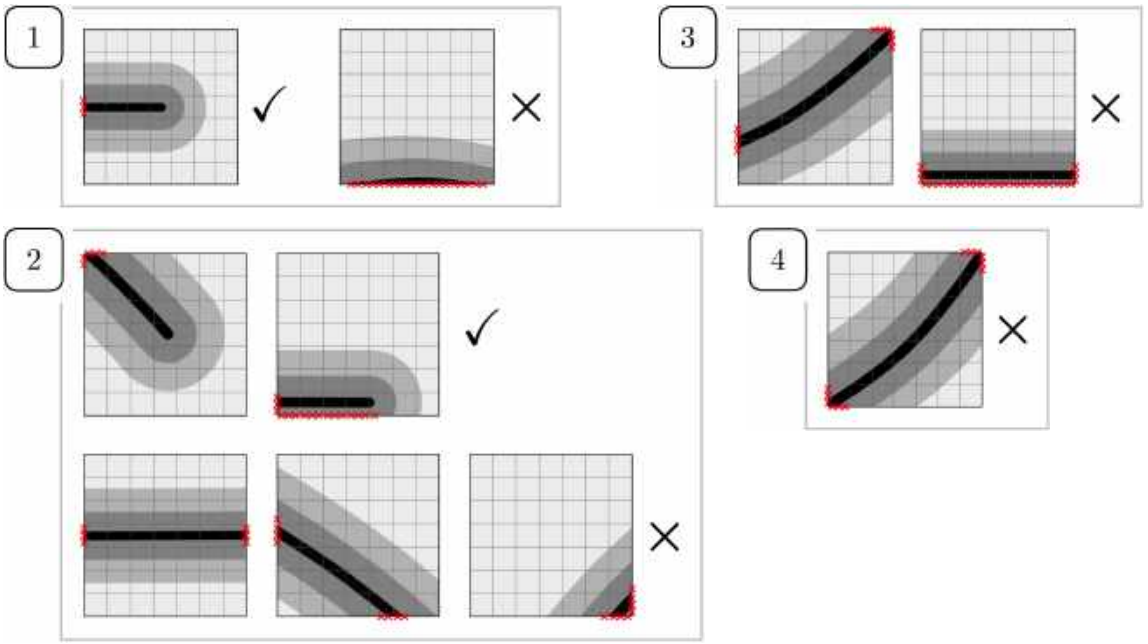

Figure 4.3: Detail of a refined element with possible crack paths. Cases are classified depending on the number of intersected sides. Red crosses indicate integration points on the sides with $d > 0.95$.

advanced to an ambiguous position and consider its previous localization. This is not a problem since the threshold distance in the switching criterion is always taken coarse enough, and propagating cracks leave the ambiguous positions as they evolve in the following iterations.

This simple method is enough for all the 2D examples presented in this paper, taking $A^* = hl/5$. The robust extension of the algorithm to 3D is nontrivial due to the numerous possible cases. Elements containing crack fronts are easily identified for the particular example in Section 4.6.5 since the direction of crack propagation is known.

Other strategies may be explored, for instance, applying the medial-axis algorithm proposed by Tamayo-Mas and Rodríguez-Ferran [2015].

4.4 Transition to discontinuous fracture and definition of the sharp crack geometry

In elements in the wake of crack tips, no variation of crack paths is expected and the phase-field damage band is replaced by a sharp representation. This implies a significant reduction in the computational cost of simulations. The transition is done for fully degraded material, so no additional energetic considerations are needed.

Sharp cracks are defined by the union of elemental contributions. Once a cut element transitions from Ω_{tips} to Ω_{xfem}, the crack path is identified within the phase-field diffuse band and is then added to the existing sharp crack. The process is illustrated in Figure 4.4.

For both 2D and 3D problems, we search for intersections of the diffuse cracks along the edges of the mesh of transitioning elements. In the 1-dimensional searchs, intersections are taken as the middle points of the nodes (in the refined discretization) with $d > 0.98$. In 2D, this leads to piecewise linear cracks, with a segment in each cut element. In the event of crack branching, a proper piecewise representation is considered in the element containing the branching point, as shown in Section 4.6.3. In 3D, crack surfaces are constructed as the tringular facets defined by the intersection points on edges. Note that these facets can have very different sizes. This is not a problem since the surface is used only to define the integration subdomains in the element.

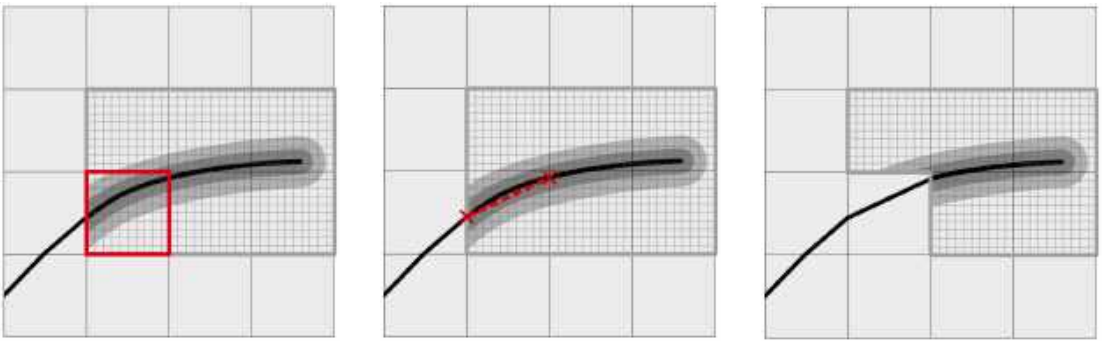

Figure 4.4: Sketch of transition to sharp crack. The diffuse crack is replaced by a sharp crack in the element selected to be derefined, marked with red square. In 2D the crack is composed by linear segments, defined by the intersection of the diffuse crack with the elements sides.

This algorithm is enough to show the capabilities of the strategy. In our numerical examples, it leads to similar results to the ones obtained by a plain phase-field model. More sophisticated techniques can be introduced at this step if more accuracy is needed or crack paths are more challenging, such as a higher-degree curved representation of the crack path in each cut element, given by more than 2 points in 2D as done by Gürkan et al. [2016], the medial-axis algorithm by Tamayo-Mas and Rodríguez-Ferran [2015] or the optimization-based approach in Geelen et al. [2018].

It is important for the different representations along a crack (sharp and diffuse) to match on the interface Γ with enough accuracy, to avoid the creation of unphysical corners. In our experience, level-set representations of the crack in the coarse background mesh are not accurate enough to fulfill this requirement.

Regarding the displacement field, since it is computed in the staggered scheme in Section 4.2.4, there is no need to compute its projection into the new approximation space.

4.5 Refinement of elements and cracks coalescence

When an element in Ω_{xfem} is selected to be refined, nodal values for the damage have to be defined. If the element is refined for the first time, nodal values of the damage can be set to zero except for the nodes on the interface, where the damage is known. If the element is intersected by a sharp crack, the damage field in the element has to

approximate the crack. This is the case in cracks coalescence.

In experiments with merging of cracks, we may have elements cut by a sharp crack which are approached by a phase-field crack tip. In this case, the criteria in Section 4.3.1 lead to refining again the elements, transitioning back to the continuous representation. The coalescence is then handled by the phase-field model. Once the cracks have merged, the elements transition to the discontinuous again with the corresponding update in the involved sharp cracks.

In the current implementation we store the damage field for elements that transition to discontinuous and recover its value in case these elements need to be refined again. Another option would be to construct the damage band from scratch using the sharp representation, for instance, defining the corresponding history field variable, $\mathcal{H}^+$, following Borden et al. [2012].

4.6 Numerical experiments

In this section, we aim to demonstrate the robustness of the proposed approach to efficiently simulate fracture processes. During the computations the background mesh is kept fixed and the discretization is automatically modified to account for the different representations of cracks.

First, a simple test is presented to numerically validate the definition of $\hat{\Gamma}$ to impose continuity of displacements between the subdomains Ω_{tips} and Ω_{xfem}. Then, several benchmark tests are visited, covering a wide range of cases in fracture simulations. Examples in 2D prove the applicability of the strategy to branching and coalescence of cracks. The approach is also applied to a fully 3D setting.

Plane strain conditions are assumed in 2D. In all examples, we solve for degree of approximation $p = 1$. The tolerance for convergence in the staggered scheme is fixed to 10^{-2}. The Nitsche's parameter for the equilibrium equation is $\alpha_E = 100$ and the refinement of elements is triggered by the threshold value $d_{\text{ref}} = 0.2$.

Preexisting cracks in the domain are first introduced as diffuse phase-field bands by solving the damage equation with an initial history field, $\mathcal{H}_0^+$, as described in Borden et al. [2012]. Then, before initializing the simulation, the procedure of transition to discontinuous is applied to replace the diffuse phase-field band by a sharp crack where needed, according to the respective switching criterion.

4.6.1 Test on the continuity of displacements

In this test, we analyse the effect of imposing continuity of displacements on the whole interface Γ and on the cropped interface $\hat{\Gamma}$ (defined in (4.1) as the part of Γ where the material is not significantly degraded) on a simple tension test with a fixed crack.

Consider a square plate in $[-0.4, 0.4] \times [-0.5, 0.5]$ mm^2 with a horizontal crack at midheight crossing the whole piece. The piece is clamped on its bottom face and has imposed displacements $(0, u_D)$ on its top face, with $u_D = 10^{-4}$ mm. The material parameters are $E = 20$ GPa, $\nu = 0.3$ and $G_C = 10^{-4}$ kN/mm.

The crack is represented by a sharp crack for $x < 0$ and by a smeared damage band for $x > 0$, with a length-scale parameter $l = 0.012$ mm. The domain is covered by a uniform quadrilateral mesh with 12×15 elements and Ω_{tips} is taken as $\{x \geq 0, |y| \leq 0.075 \text{ mm}\}$. The rest of the domain is Ω_{xfem}. Elements are refined with a uniform submesh of refinement factor $m = 15$. See the discretization in Figure 4.5.

Figure 4.6 shows the vertical displacement field u_y when the equilibrium equation is solved imposing continuity of displacements on $\hat{\Gamma}$. As expected, the upper half moves rigidly, with a *constant* vertical displacement equal to u_D, whereas the lower half does not move and has zero vertical displacement. In Ω_{xfem} we obtain the expected discontinuity and in Ω_{tips} the displacement is continuous and abruptly varies between these two values.

We repeat the experiment imposing continuity on the whole interface Γ. The vertical displacements exhibit an unrealistic pattern near the gluing of the two representations of the crack, due to the different material stifnesses, see Figure 4.6.

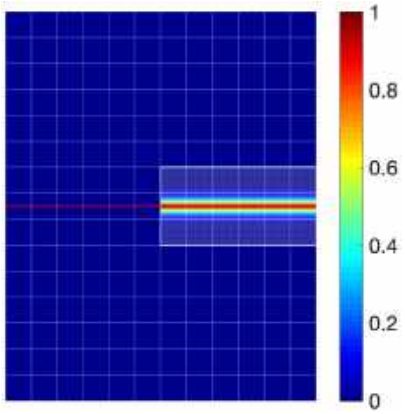

Figure 4.5: *Test on continuity.* Initial discretization and approximation of the crack.

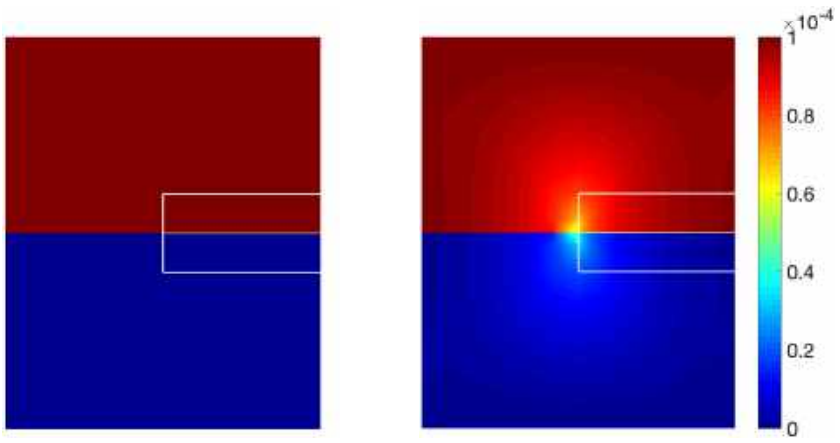

Continuity on $\hat{\Gamma}$ Continuity on Γ

Figure 4.6: *Test on continuity.* Vertical displacement field u_y imposing continuity on $\hat{\Gamma}$ and on Γ.

Consequently, continuity will be imposed on $\hat{\Gamma}$ in all examples.

4.6.2 L-shaped panel test

Consider an L-shaped panel with boundary conditions and material parameters as described in Section 2.3.2. The phase-field length-scale parameter is $l = 2.5$ mm and the load process takes displacement increments of $\Delta u_D = 10^{-3}$ mm.

The background mesh is a uniform quadrilateral mesh with element size $h = 10$ mm, and elements in Ω_{tips} are refined with refinement factor $m = 20$. The subdomain Ω_{tips} initially consists of the 3 elements in the corner of the piece, where crack inception is expected. The distance of derefinement in the switching criterion is taken as $\delta_{\text{ref}} = 2h$. Recall that a correct initial definition of Ω_{tips}, including crack tips and notches of the domain, is essential since the damage field is computed only in this part of the domain.

As a reference solution, we run the simulation with a plain phase-field model with adaptivity, following the refinement strategy in Chapter 3. The equations of the hybrid phase-field model are solved in the whole domain. Elements along cracks are dynamically refined, but no transition to a sharp representation is considered. Thus, more elements become refined as the crack propagates. On the contrary, in the newly proposed approach, only elements near the crack tip are refined. Thus, the size of Ω_{tips} does not increase constantly. Elements which are far enough from the crack tip transition to an XFEM coarser representation, and the damage band is replaced by

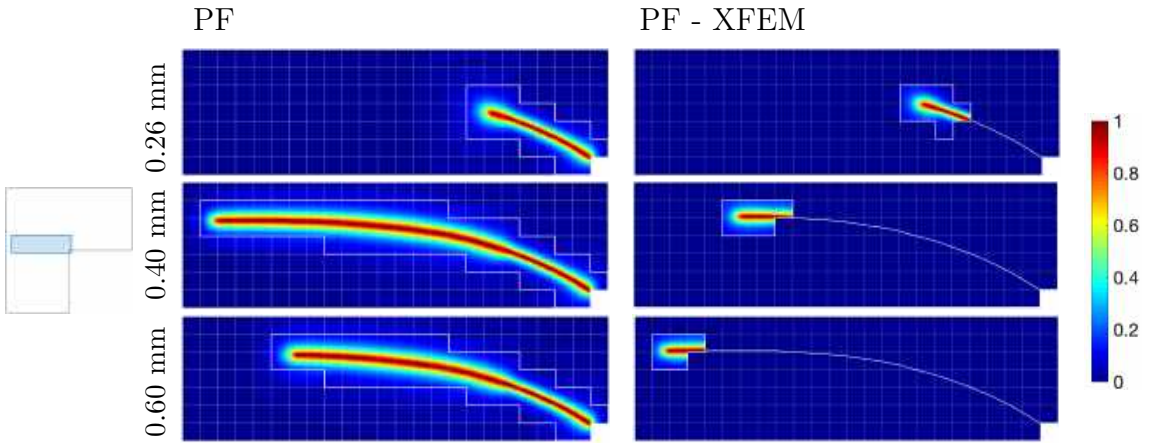

Figure 4.7: *L-shaped test.* Damage field at different load steps for PF and PF-XFEM. The sharp crack in PF-XFEM is plotted in white. Zoom into $[-230, 10] \times [-10, 60]$ mm^2.

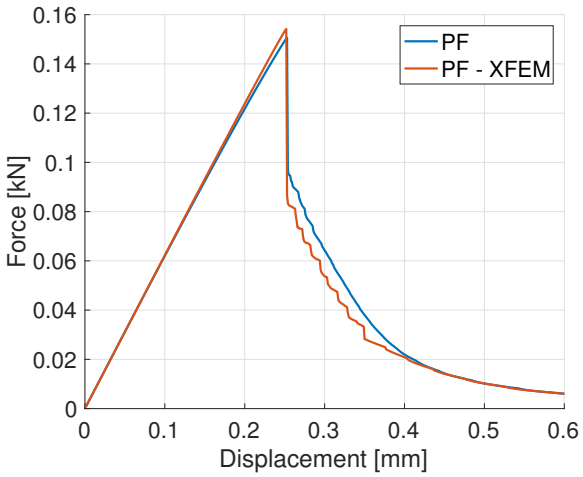

Figure 4.8: *L-shaped test.* Load-displacement curve for PF and PF-XFEM.

a sharp crack. Remeshing is avoided in both cases. In what follows, we abbreviate these approaches by PF and PF-XFEM, respectively.

The crack path obtained with the two strategies at different load steps is depicted in Figure 4.7. We obtain similar results, with a slightly faster propagation for PF-XFEM at load step $u_D = 0.26$ mm. This can be explained by the spurious transmission of forces across phase-field cracks, while sharp cracks are completely traction-free. In both cases, the discretization is updated according to crack growth.

The slightly faster propagation when introducing sharp cracks is also observed in the load-displacement curves in Figure 4.8. After the peak, when the crack starts

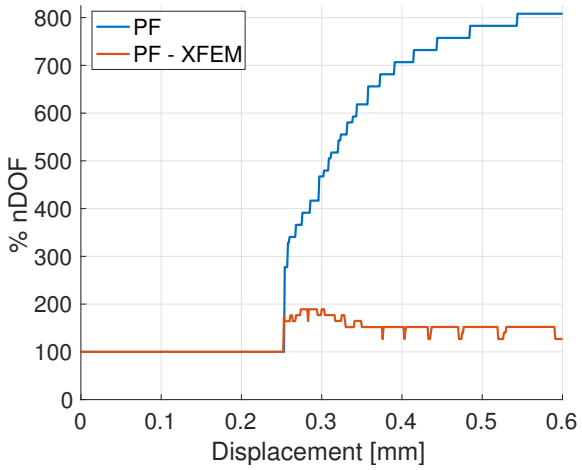

Figure 4.9: *L-shaped test.* Evolution of nDOF in the equilibrium equation for PF and PF-XFEM. The percentage is computed with respect to the nDOF of the initial discretization.

propagating, we observe a steeper descent of the curve, meaning the crack is slightly longer. As the simulations evolve, the difference between approaches diminishes. In the PF curve, we observe the characteristic loss of stiffness prior to the peak of these models; solving the damage equation in the whole domain with the quadratic degradation function $g(d) = (1-d)^2$ propagates the damage, softening the piece in the simulation. In PF-XFEM the behavior of the material before cracking is closer to linear elasticity because the damage is computed only in small subdomains.

For PF-XFEM, Ω_{tips} takes a very small part of the domain. This leads to a reduction of the number of degrees of freedom (nDOF) for the equilibrium equation. The reduction is substantial even though in PF the mesh is refined only in a narrow band containing the crack. Figure 4.9 shows the evolution of nDOF with respect to its initial value. For PF, the number increases up to 800%, while for PF-XFEM nDOF the value increases only up to 150%.

4.6.3 Branching test

The configuration and the material parameters of the test are detailed in Section 2.3.4. This example is revisited here to test the capability of the strategy to reproduce bifurcations, as well as to handle multiple disconnected subdomains in Ω_{tips}.

We take $l = 0.01$ mm and load increments of $\Delta u_D = 5 \cdot 10^{-5}$ mm. The domain is discretized into a uniform quadrilateral mesh of 45×45 elements. Elements are refined

with refinement factor $m = 15$. The threshold distance in the switching criterion is taken as $\delta_{\text{ref}} = 3h$. The initial Ω_{tips} consists of the elements containing the preexisting crack and the rest of the domain is part of Ω_{xfem}.

The obtained crack at different stages is shown in Figure 4.10. The crack propagates horizontally and then branches abruptly, maintaining the symmetry of the solution in the whole simulation. When the branching occurs, we start having two crack tips and Ω_{tips} contains the elements near both of them. In Ω_{xfem} we have two separate sharp cracks, each one of them contributing to the XFEM discretization with an independent Heaviside function.

The evolution of the crack at the load step when it branches, $u_D = 0.05195$ mm, is plotted in Figure 4.11 at some illustrative staggered iterations. The existing sharp crack is updated with the contribution of one of the branches and the other branch defines the new sharp crack. If the branching point is interior to the element, the representation of the crack is piecewise linear and contains the point, i.e. it is defined by a Y-shaped approximation, as can be seen in the third plot of Figure 4.11.

As reported in Sections 2.3.4 and 3.3.3, we observe a slight interpenetration of the crack faces near the branching point. In the phase-field model, interpenetration is prevented by the definition of $g(d)$ in (1.14c), but when transitioning to the XFEM representation the crack faces intersect as shown in Figure 4.12. This issue can be tackled by implementing contact conditions into the XFEM discretization, see for instance the approaches by Kim et al. [2007] and Giner et al. [2009].

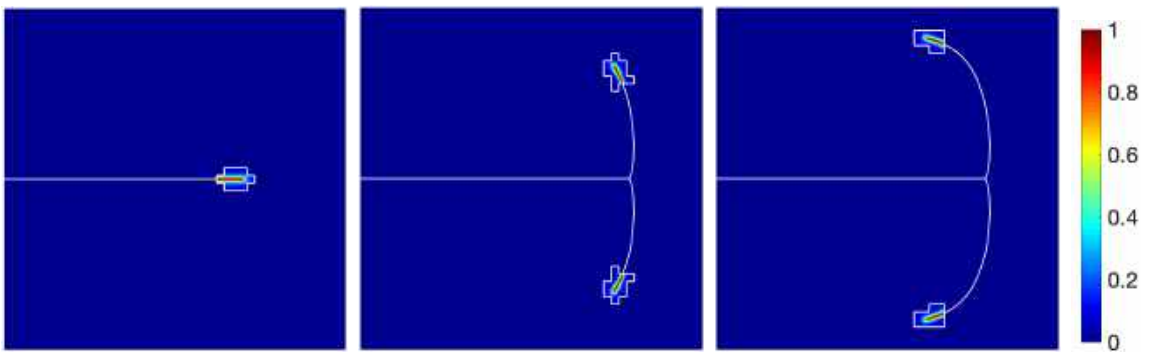

$u_D = 0.030$ mm $\quad$ $u_D = 0.055$ mm $\quad$ $u_D = 0.080$ mm

Figure 4.10: *Branching test.* Evolution of the crack at different load steps. The sharp crack is plotted in white.

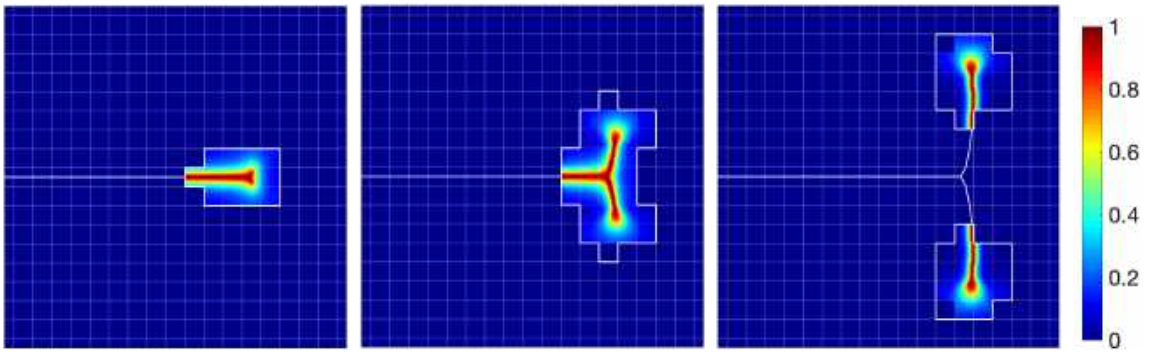

$s = 0$ $s = 20$ $s = 40$

Figure 4.11: *Branching test.* Detail of the crack path at some staggered iterations for imposed displacement $u_D = 0.05195$ mm, taking a zoom into $[0, 0.8] \times [-0.4, 0.4]$ mm^2.

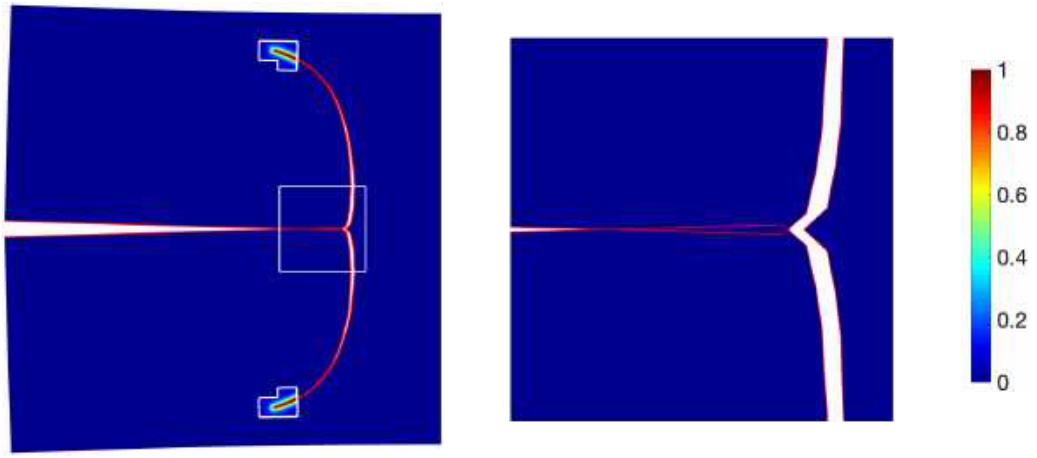

Figure 4.12: *Branching test.* Deformed piece at imposed displacement $u_D = 0.08$ mm. Crack faces, highlighted in red, show a slight interpenetration, taking a zoom into $[0.25, 0.65] \times [-0.2, 0.2]$ mm^2.

4.6.4 Multiple cracks test

This example exhibits the robustness of the proposed strategy to simulate coalescence of cracks. The setting and the parameters are described in Section 3.3.4. Here, the length-scale parameter is $l = 0.012$ mm and we take increments of $\Delta u_D = 5 \cdot 10^{-5}$ mm. The background mesh is a uniform quadrilateral mesh with 47×47 elements and the refinement factor is $m = 17$. The distance to switch to discontinuous is $\delta_{\text{ref}} = 3h$.

The obtained crack pattern is plotted in Figure 4.13. The initial cracks propagate, coalescing between them, until the piece is broken into 4 independent pieces. There are two mergings of cracks in the process. Since cracks grow abruptly, we need to plot

the crack at staggered iterations to see the detail of how coalescence is handled by the method. Figure 4.14 shows some representative staggered iterations for imposed displacement $u_D = 0.262$ mm. In the figure, we can see how the sharp crack in the right is replaced by its diffuse representation as the crack tip approaches and the cut elements are refined. Then, after the merging has occured, all the elements in this subdomain of Ω_{tips} transition back to Ω_{xfem}.

Now, we compare the results with the ones obtained by a PF approach. The final partition of the piece for both approaches is shown in Figure 4.15. The damage field corresponds to the PF simulation, and the final sharp crack for PF-XFEM is plotted in black. The crack patterns are very similar also in this more complex scenario. The corresponding load-displacement curves for the horizontal and vertical loads, F_x and F_y, in Figure 4.16, again indicate a loss of stiffness for PF in the precracking regime and a steeper descent of the curves for PF-XFEM. The evolution of nDOF is plotted in Figure 4.17, showing a substantial decrease in nDOF. For PF-XFEM we observe a reduction of nDOF as crack tips disappear, while in PF the nDOF always increases.

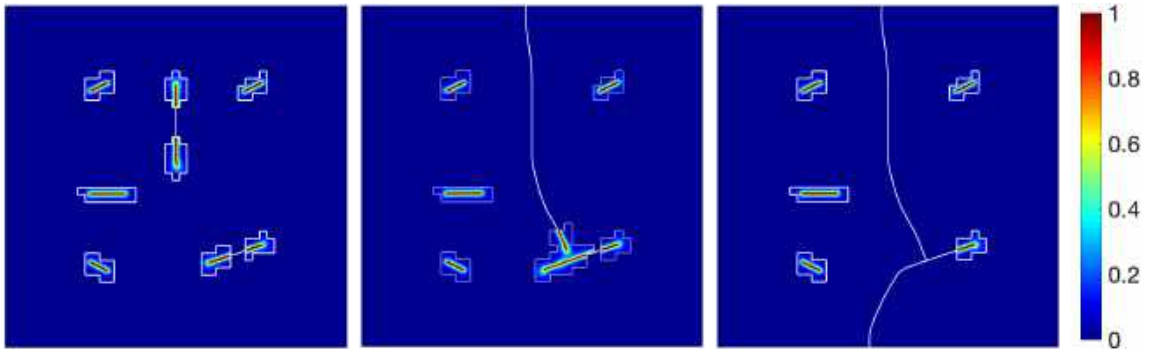

$u_D = 0.0120$ mm $u_D = 0.0125$ mm $u_D = 0.0130$ mm

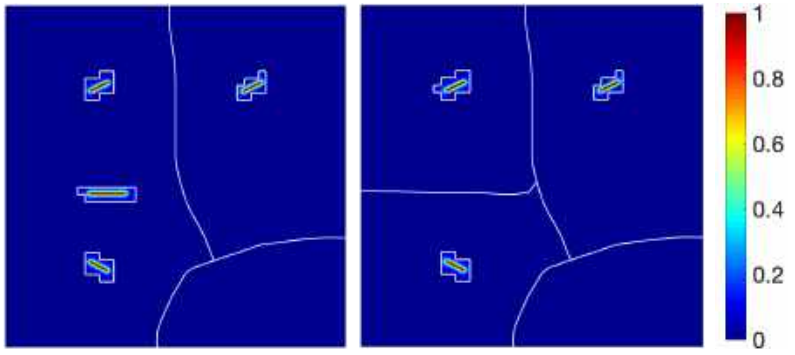

$u_D = 0.019$ mm $u_D = 0.027$ mm

Figure 4.13: *Multiple cracks test.* Damage field at several imposed displacements.

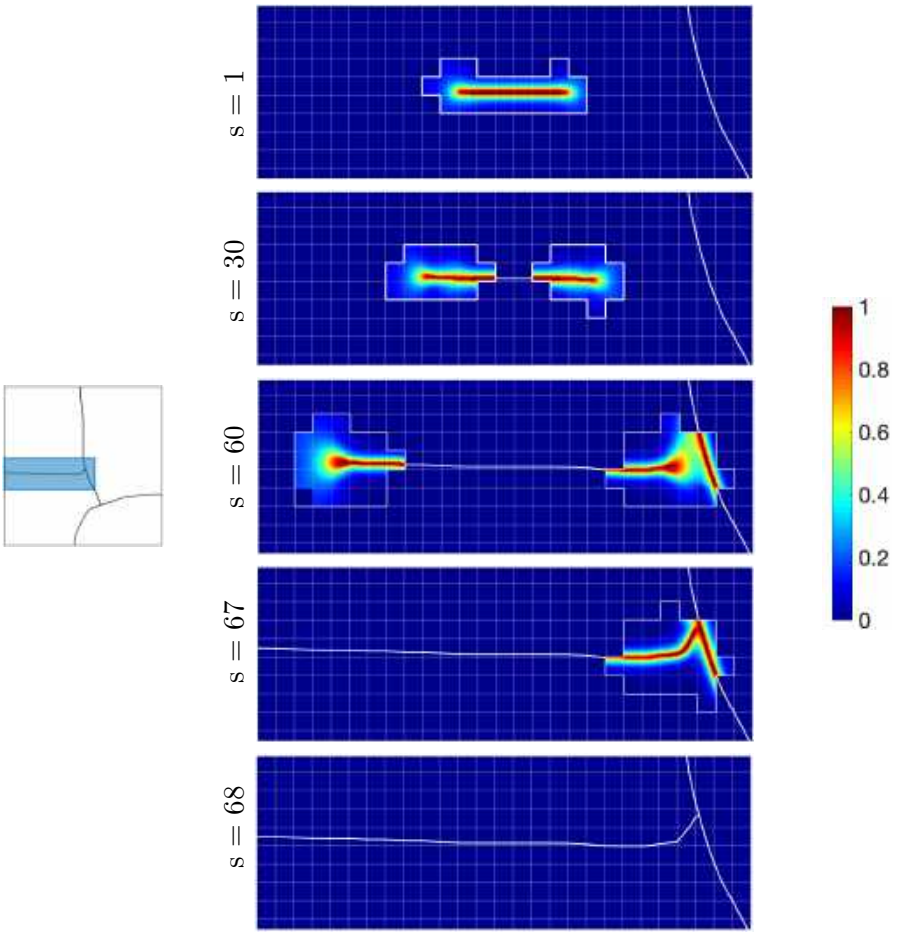

Figure 4.14: *Multiple cracks test.* Crack pattern at different staggered iterations for imposed displacement $u_D = 0.262$ mm. Zoom into $[0, 1.15] \times [0.7, 1.1]$ mm^2.

4.6.5 Twisting crack in a 3D beam

In this example we test the performance of the method in the fully 3D example proposed in Section 3.3.5. The length parameter is $l = 2$ mm and the load steps take increments $\Delta u_D = 5 \cdot 10^{-4}$ mm. We use a uniform hexahedral mesh with element size $h = 3.125$ mm and refinement factor $m = 7$. The distance in the switching criterion is $\delta_{\text{ref}} = 2h$. The initial notches are modeled by diffuse cracks and Ω_{tips} is the union of elements that contain them.

In this case, the initial cracks coalesce, completely splitting the beam at a single load step, as can be seen in the load-displacement curve in Figure 4.18. Figure 4.19 shows the final geometry at load step $u_D = 0.0645$ mm. The sharp crack is a twisted surface to match the initial notches, defined by triangular facets. Considering a sharp representation of the crack enables to completely separate the two resulting pieces.

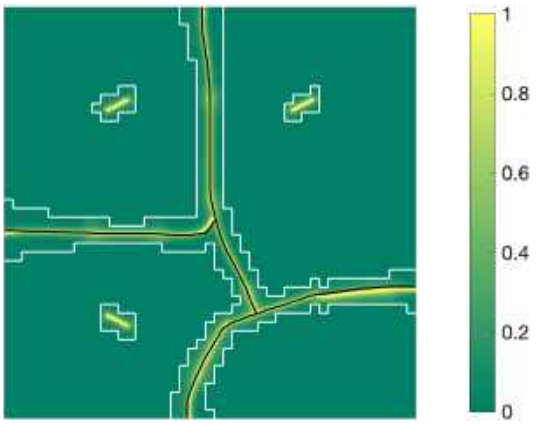

Figure 4.15: *Multiple cracks test.* Comparison with the PF solution.

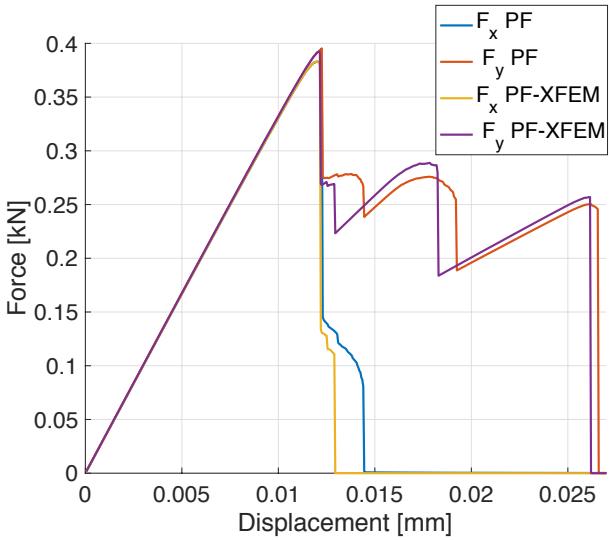

Figure 4.16: *Multiple cracks test.* Load-displacement curve.

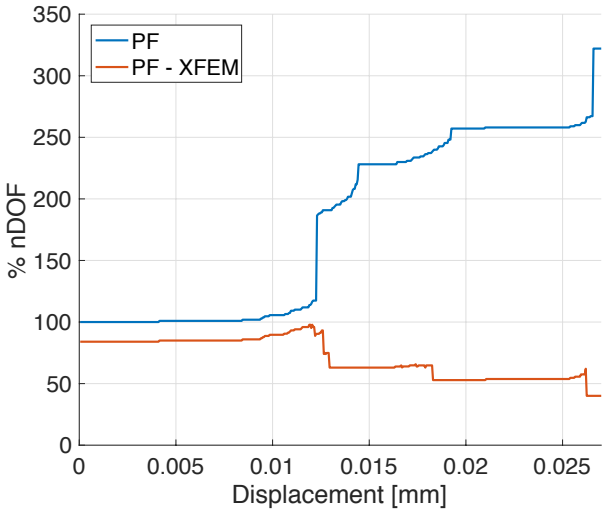

Figure 4.17: *Multiple cracks test.* Evolution of the number of degrees of freedom.

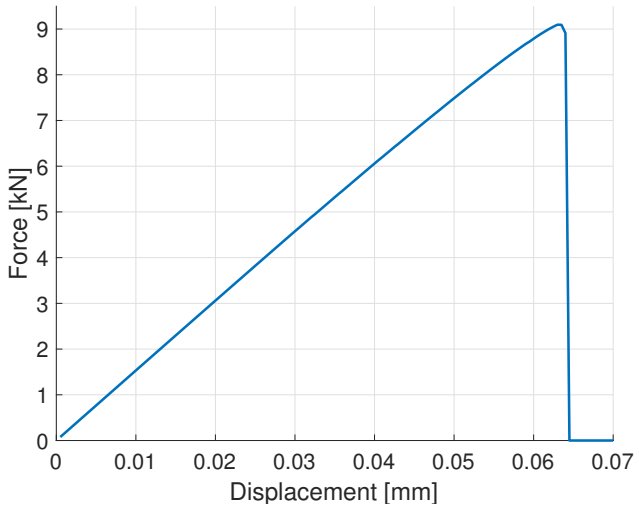

Figure 4.18: *Twisting test.* Load-displacement curve. The piece completely breaks at $u_D = 0.0645$ mm.

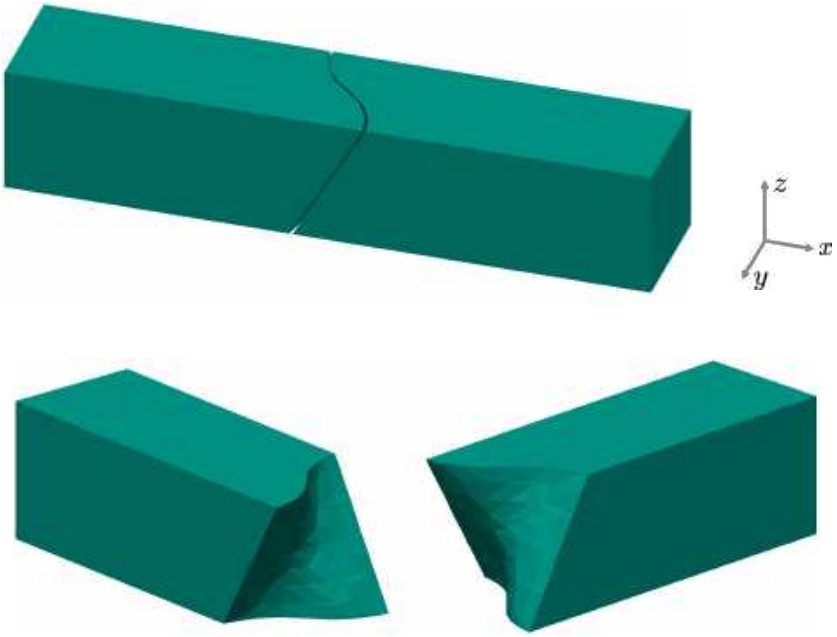

Figure 4.19: *Twisting test.* Geometry of the piece at imposed displacement $u_D = 0.0645$ mm. The initial beam breaks into two independent and symmetric halves.

4.7 Conclusions

We propose a novel method to simulate fracture which is based on combining a phase-field model in small subdomains around crack tips, Ω_{tips}, and a discontinuous model in the rest of the domain, Ω_{xfem}. The approach overcomes the limitations of

both continuous and discontinuous models. Propagation is described by the phase-field solution in Ω_{tips}, while an XFEM approximation explicitly describes the crack opening and enables to use a coarser discretization in almost the whole domain. In all examples, a correct definition of the initial partition in Ω_{tips} and Ω_{xfem} is crucial to detect crack inception.

Computationally, the same background mesh is used during the whole simulation. Refined elements are nested in Ω_{tips} to capture the phase-field solution and the sharp cracks are introduced via XFEM. The discretization is automatically updated as cracks propagate and remeshing is avoided. Nitche's method is used to impose continuity of displacements in weak form to mantain a very local refinement with no transitioning elements.

The robustness of the strategy has been proved in 2D and 3D, including scenarios with branching and coalescence. The obtained results are comparable to the ones from a plain phase-field approach, but with an important reduction in the number of degrees of freedom. Also, the response of the pieces in the linear elastic regime is more realistic and transmission of forces across cracks is prevented. The methodology is an efficient alternative for fracture simulation.

Chapter 5

Conclusions and future work

5.1 Summary

The main contributions presented in this thesis are:

1. **An HDG formulation for phase-field models with adaptivity**, proposed in Chapter 2 and Muixí et al. [2020c].

   The strategy considers two types of elements, standard and refined, in an HDG formulation of the problem. In refined elements, the space of approximation is uniformly h-refined with a fixed refinement factor. The HDG method imposes continuity between elements in weak form, and therefore handles the non-conformal approximations in a straightforward manner. The proposed implementation, with a refined reference element, enables to keep the structure of the HDG code for phase-field models and to maintain the same background mesh during all the simulation.

   The robustness of the method is tested in 2D for low and high-order degrees of approximation and refinement factors up to $m = 20$, also accounting for non-structured meshes.

   This proposal overcomes previous adaptive approaches in the literature by offering an extremely local refinement, without dealing with hanging nodes nor additional unknown fields. However, HDG has a higher computational cost and a more involved implementation than the continuous FEM. This motivates the

alternative adaptivity approach based on a standard FEM formulation with Nitsche's method, which is discussed next.

2. **An adaptive strategy for phase-field models in a continuous FEM setting by means of Nitsche's method**, proposed in Chapter 3 and Muixí et al. [2020a].

   The mesh is partitioned into refined and standard regions. In each region, we use a continuous FEM approximation and, then, on the interface between regions, continuity is imposed in weak form with Nitsche's method. The Nitsche's method introduces a scalar parameter in the formulation, that can be easily tuned by numerical experimentation. Also in this strategy, our proposal for the implementation is based on a refined reference element, simplifying the incorporation of the refinement process in a working FEM code for phase-field models.

   The strategy has the same advantages as the previous HDG proposal, thanks to the element-by-element refinement, the weak imposition of continuity between elements of different type and the robustness of Nitsche's method, but here with a lower computational cost. The faster simulations have encouraged the extension of the strategy to 3D.

3. **A combined XFEM phase-field computational model for crack growth**, proposed in Chapter 4 and Muixí et al. [2020b].

   The combined model inherits the advantages of both the phase-field and the discontinuous models: the phase-field model drives the propagation in small subdomains around crack tips, while the discontinuous model enables to use an XFEM coarser approximation elsewhere. The refinement is only needed in the small crack-tip subdomains, leading to a further reduction of the computational cost, which may be crucial for very demanding simulations.

   Differently to other combined XFEM phase-field approaches in the literature, diffuse and sharp representations of cracks are not overlapped; we avoid dealing with crack-tip enrichment in the XFEM discretization and iterating between a global and a local problem around crack-tips. The two models are glued by imposing continuity in weak form for the displacement field, only on a cropped part of the interface between regions, and by the definition of convenient boundary conditions for the damage field in the small subdomains.

From a practical point of view, transitioning to a sharp representation of cracks complicates the implementation of the strategy, since the method requires a careful selection of all the ingredients to ensure accuracy. Namely, we need to approximate the position of crack tips in order to define the small subdomains, and locate sharp cracks within the phase-field bands. Also, the strategy relies on a robust implementation of XFEM, accounting for the integration in cut elements.

On the other hand, the combined model gives an explicit definition of cracks in almost the whole domain, which may be exploited in some applications, and leads to more efficient simulations.

Thus, practitioners may choose the fully adaptive phase-field approach or the combined method depending on the particular application, the available XFEM libraries, or if the save in CPU time is worth the non-negligible implementation effort.

Alongside the above-mentioned major novelties, there are some additional contributions which are also worth mentioning. These are:

4. **The first HDG formulation for phase-field models of fracture**, presented in Section 2.1. The method has ben tested by numerical comparison with the usual FEM formulation in Appendix A. The results obtained with HDG are more accurate, if the same mesh and degree of approximation are used, but at the price of a higher computational cost. The formulation establishes a suitable setting for adaptivity.

5. **A new branching test in the quasi-static regime**, proposed in Section 2.3.4. Differently from other tests in the literature, no heterogeneities in the material are needed. Instead, the branching is caused by applying carefully designed boundary conditions on the piece.

6. **The first extension to 3D of a combined XFEM phase-field computational model** in Chapter 4, which is facilitated by the robustness and the efficiency of the methodology.

5.2 Publications and conferences

The developments in this thesis have led to the following articles:

a) A. Muixí, S. Fernández-Méndez, A. Rodríguez-Ferran. *A hybridizable discontinuous Galerkin phase-field model for brittle fracture.* Reports@SCM, 4(1):31–42, 2018.

b) A. Muixí, A. Rodríguez-Ferran, S. Fernández-Méndez. *A Hybridizable Discontinuous Galerkin phase-field model for brittle fracture with adaptive refinement.* International Journal for Numerical Methods in Engineering, 121(6):1147–1169, 2020.

c) A. Muixí, S. Fernández-Méndez, A. Rodríguez-Ferran. *Adaptive refinement for phase-field models of brittle fracture based on Nitsche's method.* Computational Mechanics, 66:69–85, 2020.

d) A. Muixí, O. Marco, A. Rodríguez-Ferran, S. Fernández-Méndez. *A combined XFEM phase-field computational model for crack growth without remeshing.* Submitted, 2020.

Also, some of the work has been already presented in international conferences:

- CFRAC 2019: *A Hybridizable Discontinuous Galerkin phase-field model for brittle fracture with adaptive refinement.* **A. Muixí**, S. Fernández-Méndez, A. Rodríguez-Ferran. VI International Conference on Computational Modeling of Fracture and Failure of Materials and Structures, Braunschweig, Germany.

- USNCCM 2019: *A Hybridizable Discontinuous Galerkin phase-field model: adaptivity and continuous-discontinuous transition.* A. Muixí, S. Fernández-Méndez, **A. Rodríguez-Ferran**. 15th US National Congress on Computational Mechanics, Austin (Texas), USA.

5.3 Future work

The work presented in this dissertation opens some research lines for the future, to be dealt with in order to expand the applicability of the strategies. Our suggestions are:

- **Exploiting the strategies for different phase-field models of fracture.**

  In this work, all simulations are done using the quasi-static hybrid model by Ambati et al. [2015] with the tension-compression splitting by Miehe et al. [2010a,b]. However, the adaptive strategies for phase-field models, proposed in Chapters 2 and 3, and the combined XFEM phase-field model, proposed in Chapter 4, are based on common features of all phase-field models for fracture. In particular, we use that the refinement factor is known a priori and that the damage field is a natural indicator to trigger the refinement. Thus, all the presented methodologies can be directly applied to other phase-field models in the literature, also for dynamic fracture.

  The robustness of the strategies makes them suitable to study the behavior of different models or materials, with no need to adapt the computational mesh to the possible crack paths. Also, the combined XFEM phase-field model presented in Chapter 4 could be adapted to model crack-surface physics, for instance, in fluid-driven cracks.

- **Improving the transition from phase-field cracks to sharp cracks in the combined XFEM phase-field computational model.**

  In the wake of crack tips, we locate sharp cracks within the diffuse phase-field bands and introduce them into the discretization by XFEM, as described in Chapter 4. We use a piecewise linear approximation of the sharp crack and the original XFEM discretization by Moës et al. [1999]. Although these choices are enough to demonstrate the capabilities of the approach, they clearly limit the accuracy of the results for coarse background meshes.

  The sharp crack representation can be enhanced by defining a high-degree curve in each cut element, given by more than two points. This is specially important if the solution is approximated with high order. In this line, an idea to be explored is the use of the medial-axis approach by Tamayo-Mas and Rodríguez-Ferran [2015] to locate the sharp crack. Furthermore, the considered XFEM discretization can be improved by accounting for contact conditions, as in Kim et al. [2007] and Giner et al. [2009], in order to avoid interpenetration of faces under compression and obtain physical results.

- **Accounting for voids or inclusions in the domain with a nonfitted mesh.**

  Voids or inclusions can be introduced into the discretization through a level-set representation of interfaces and a modified quadrature in elements cut by a level set, following an XFEM approach, see Fries and Belytschko [2010] and Gürkan et al. [2017]. This would simplify the mesh generation, since the background mesh would not be required to fit the boundary. This is specially useful for pieces with complex geometries.

- **Extending the adaptive strategies to phase-field models in multi-physics problems.**

  Phase-field variables are used to model evolving interfaces with complex geometries in many fields. For instance, they are used to approximate vesicle membranes, see Du et al. [2004], and interfaces between immiscible fluids, see Zhao et al. [2016]. Also in these applications, strategies for dynamically updating the refinement are crucial and the refinement factor needed is known beforehand. Thus, the methods in this thesis could be adapted to these frameworks.

- **Optimizing and parallelizing the code.**

  Even though our approaches reduce the computational cost associated to the spatial discretization, simulations are still demanding because many staggered iterations are needed to converge at every load step. Thus, the developed codes should be further optimized to run large-scale, three-dimensional simulations.

Bibliography

M. Ambati, T. Gerasimov, and L. De Lorenzis. A review on phase-field models of brittle fracture and a new fast hybrid formulation. *Comput Mech*, 55:383–405, 2015.

H. Amor, J. J. Marigo, and C. Maurini. Regularized formulation of the variational brittle fracture with unilateral contact: Numerical experiments. *J Mech Phys Solids*, 57(8):1209–1229, 2009.

C. Annavarapu, M. Hautefeuille, and J. Dolbow. A robust Nitsche's formulation for interface problems. *Comput Methods Appl Mech Eng*, 225–228:44–54, 2012.

P. Areias, T. Rabczuk, and M. Msekh. Phase-field analysis of finite-strain plates and shells including element subdivision. *Comput Methods Appl Mech Eng*, 312: 322–350, 2016.

I. Babuška and J. Melenk. The partition of unity method. *Int J Numer Methods Eng*, 40(4):727–758, 1997.

E. Béchet, H. Minnebo, N. Moës, and B. Burgardt. Improved implementation and robustness study of the X-FEM for stress analysis around cracks. *Int J Numer Methods Eng*, 64(8):1033–1056, 2005.

R. Becker, P. Hansbo, and R. Stenberg. A finite element method for domain decomposition with non-matching grids. *ESAIM: Math Model Numer Anal*, 37(2): 209–225, 2010.

T. Belytschko and T. Black. Elastic crack growth in finite element with minimal remeshing. *Int J Numer Methods Eng*, 45(5):601–620, 1999.

M. J. Borden, C. V. Verhoosel, M. A. Scott, T. J. R. Hughes, and C. M. Landis. A phase-field description of dynamic brittle fracture. *Comput Methods Appl Mech Eng*, 217-220:77–95, 2012.

B. Bourdin, G. A. Francfort, and J. J. Marigo. Numerical experiments in revisited brittle fracture. *J Mech Phys Solids*, 48(4):797–826, 2000.

B. Bourdin, G. A. Francfort, and J. J. Marigo. The variational approach to fracture. *J Elast*, 91:5–148, 2008.

É. Budyn, G. Zi, N. Moës, and T. Belytschko. A method for multiple crack growth in brittle materials without remeshing. *Int J Numer Methods Eng*, 61(10):1741–1770, 2004.

S. Burke, C. Ortner, and E. Süli. An Adaptive Finite Element Approximation of a Variational Model of Brittle Fracture. *SIAM J Numer Anal*, 48(3):980–1012, 2010.

M. Cervera, M. Chiumenti, and R. Codina. Mixed stabilized finite element methods in nonlinear solid mechanics Part I: Formulation. *Comput Methods Appl Mech Eng*, 199(37):2559–2570, 2010.

K. J. Chang. On the maximum strain criterion – a new approach to the angled crack problem. *Eng Fract Mech*, 14(1):107–124, 1981.

B. Cockburn, J. Gopalakrishnan, and R. Lazarov. Unified hybridization of discontinuous Galerkin, mixed and continuous Galerkin methods for second order elliptic problems. *SIAM J Numer Anal*, 47(2):1319–1365, 2009.

B. Cockburn, W. Qiu, and K. Shi. Conditions for superconvergence of HDG methods for second-order elliptic problems. *Math Comp*, 81(279):1327–1353, 2012.

Q. Du, C. Liu, and X. Wang. A phase field approach in the numerical study of the elastic bending energy for vesicle membranes. *J Comput Phys*, 198(2):450–468, 2004.

C. A. Duarte, D. Kim, and I. Babuška. A Global-Local Approach for the Construction of Enrichment Functions for the Generalized FEM and Its Application to Three-Dimensional Cracks. In *Leitão V.M.A., Alves C.J.S., Armando Duarte C. (eds) Advances in Meshfree Techniques. Computational Methods in Applied Sciences, vol 5. Springer, Dordrecht*, pages 1–26, 2007.

F. Erdogan and G. C. Sih. On the crack extension in plates under plane loading and transverse shear. *J Basic Eng*, 85(4):519–525, 1963.

S. Fernández-Méndez and A. Huerta. Imposing essential boundary conditions in mesh-free methods. *Comput Methods Appl Mech Eng*, 193(12-14):1257–1275, 2004.

G. A. Francfort and J. J. Marigo. Revisiting brittle fracture as an energy minimization problem. *J Mech Phys Solids*, 46(8):1319–1342, 1998.

F. Freddi and G. Royer-Carfagni. Regularized variational theories of fracture: A unified approach. *J Mech Phys Solids*, 58(8):1154–1174, 2010.

T. Fries and T. Belytschko. The extended/generalized finite element method: An overview of the method and its applications. *Int J Numer Methods Eng*, 84(3): 253–304, 2010.

G. Fu, B. Cockburn, and H. Stolarski. Analysis of an HDG method for linear elasticity. *Int J Numer Methods Eng*, 102(3–4):551–575, 2015.

R. Geelen, Y. Liu, J. Dolbow, and A. Rodríguez-Ferran. An optimization-based phase-field method for continuous-discontinuous crack propagation. *Int J Numer Methods Eng*, 116(1):1–20, 2018.

R. Geelen, Y. Liu, T. Hu, M. Tupek, and J. Dolbow. A phase-field formulation for dynamic cohesive fracture. *Comput Methods Appl Mech Eng*, 348:680–711, 2019.

R. Geelen, J. Plews, M. Tupek, and J. Dolbow. An extended/generalized phase-field finite element method for crack growth with global-local enrichment. *Int J Numer Methods Eng*, 121(11):2534–2557, 2020.

T. Gerasimov and L. De Lorenzis. A line search monolithic approach for phase-field computing of brittle fracture. *Comput Methods Appl Mech Eng*, 312:276–303, 2016.

E. Giner, M. Tur, J. Tarancón, and F. Fuenmayor. Crack face contact in X-FEM using a segment-to-segment approach. *Int J Numer Methods Eng*, 82(11):1424–1449, 2009.

G. Giorgiani, D. Modesto, S. Fernández-Méndez, and A. Huerta. High-order continuous and discontinuous Galerkin methods for wave problems. *Int J Numer Methods Fluids*, 73(10):883–903, 2013.

B. Giovanardi, A. Scotti, and L. Formaggia. A hybrid XFEM-Phase field (*Xfield*) method for crack propagation in brittle elastic materials. *Comput Methods Appl Mech Eng*, 320:396–420, 2017.

M. Griebel and M. A. Schweitzer. A Particle-Partition of Unity Method. Part V: Boundary Conditions. In *Stefan Hildebrandt and Hermann Karcher (eds) Geometric Analysis and Nonlinear Partial Differential Equations, Springer, Berlin*, pages 519–542, 2003.

C. Gürkan, E. Sala-Lardies, M. Kronbichler, and S. Fernández-Méndez. eXtended Hybridizable Discontinous Galerkin (X-HDG) for void problems. *J Sci Comput*, 66:1313–1333, 2016.

C. Gürkan, M. Kronbichler, and S. Fernández-Méndez. eXtended Hybridizable Discontinuous Galerkin with Heaviside enrichment for heat bimaterial problems. *J Sci Comput*, 72:542–567, 2017.

P. Hansbo. Nitsche's method for interface problems in computational mechanics. *GAMM-Mitteilungen*, 28(2):183–206, 2005.

T. Heister, M. F. Wheeler, and T. Wick. A primal-dual active set method and predictor-corrector mesh adaptivity for computing fracture propagation using a phase-field approach. *Comput Methods Appl Mech Eng*, 290:466–495, 2015.

P. Hennig, S. Müller, and M. Kästner. Bézier extraction and adaptive refinement of truncated hierarchical NURBS. *Comput Methods Appl Mech Eng*, 305:316–339, 2016.

P. Hennig, M. Ambati, L. De Lorenzis, and M. Kästner. Projection and transfer operators in adaptive isogeometric analysis with hierarchical B-splines. *Comput Methods Appl Mech Eng*, 334:313–336, 2018.

T. Y. Hou and X. H. Wu. A Multiscale Finite Element Method for Elliptic Problems in Composite Materials and Porous Media. *J Comput Phys*, 134(1):169–189, 1997.

T. Y. Kim, J. Dolbow, and T. Laursen. A mortared finite element method for frictional contact on arbitrary interfaces. *Comput Mech*, 39:223–235, 2007.

R. M. Kirby, S. J. Sherwin, and B. Cockburn. To CG or to HDG: A Comparative Study. *J Sci Comput*, 51:183–212, 2012.

M. Kronbichler, K. Kormann, and W. Wall. Fast matrix-free evaluation of hybridizable discontinuous Galerkin operators. *Lecture Notes in Computational Science and Engineering*, 126:581–589, 2019.

A. La Spina, M. Giacomini, and A. Huerta. Hybrid coupling of CG and HDG discretizations based on Nitsche's method. *Comput Mech*, 65:311–330, 2020.

P. Laborde, J. Pommier, Y. Renard, and M. Salaün. High-order extended finite element method for cracked domains. *Int J Numer Methods Eng*, 64(3):354–381, 2005.

S. Lee, M. F. Wheeler, and T. Wick. Pressure and fluid-driven fracture propagation in porous media using an adaptive finite element phase field model. *Comput Methods Appl Mech Eng*, 305:111–132, 2016.

Y.-S. Lo, M. J. Borden, K. Ravi-Chandar, and C. M. Landis. A phase-field model for fatigue crack growth. *J Mech Phys Solids*, 132:103684, 2019.

O. Marco, R. Sevilla, Y. Zhang, J. J. Ródenas, and M. Tur. Exact 3D boundary representation in finite element analysis based on Cartesian grids independent of the geometry. *Int J Numer Methods Eng*, 103(6):445–468, 2015.

J. Melenk and I. Babuška. The partition of unity finite element method: Basic theory and applications. *Comput Methods Appl Mech Eng*, 139(1):289–314, 1996.

C. Miehe, M. Hofacker, and F. Welschinger. A phase-field model for rate-independent crack propagation: robust algorithmic implementation based on operator splits. *Comput Methods Appl Mech Eng*, 199(45):2765–2778, 2010a.

C. Miehe, F. Welschinger, and M. Hofacker. Thermodynamically consistent phase-field models of fracture: variational principles and multi-field FE implementations. *Int J Numer Methods Eng*, 83(10):1273–1311, 2010b.

N. Moës, J. Dolbow, and T. Belytschko. A finite element method for crack growth without remeshing. *Int J Numer Methods Eng*, 46(1):131–150, 1999.

A. Muixí, S. Fernández-Méndez, and A. Rodríguez-Ferran. A hybridizable discontinuous Galerkin phase-field model for brittle fracture. *Reports@SCM*, 4(1):31–42, 2018.

A. Muixí, S. Fernández-Méndez, and A. Rodríguez-Ferran. An HDG phase-field model for brittle fracture with adaptive refinement. `https://www.youtube.com/watch?v=pjgxZz9vbLI`, July 2019a.

A. Muixí, S. Fernández-Méndez, and A. Rodríguez-Ferran. Phase-field solution of brittle fracture with adaptive refinement. `https://youtu.be/FiQQe6UpenI`, December 2019b.

A. Muixí, S. Fernández-Méndez, and A. Rodríguez-Ferran. Adaptive refinement for phase-field models of brittle fracture based on Nitsche's method. *Comput Mech*, 66:69–85, 2020a.

A. Muixí, O. Marco, A. Rodríguez-Ferran, and S. Fernández-Méndez. A combined XFEM phase-field computational model for crack growth without remeshing. *Submitted*, 2020b.

A. Muixí, A. Rodríguez-Ferran, and S. Fernández-Méndez. A Hybridizable Discontinuous Galerkin phase-field model for brittle fracture with adaptive refinement. *Int J Numer Methods Eng*, 121(6):1147–1169, 2020c.

S. Nagaraja, M. Elhaddad, M. Ambati, S. Kollmannsberger, L. De Lorenzis, and E. Rank. Phase-field modeling of brittle fracture with multi-level *hp*-FEM and the finite cell method. *Comput Mech*, 63:1283–1300, 2019.

J. Nitsche. Über ein variationsprinzip zur lösung von Dirichlet-problemen bei verwendung von teilr äumen, die keinen randbedingungen unterworfen sind. *Abh Math Se Univ*, 36(1):9–15, 1971.

N. Noii, F. Aldakheel, T. Wick, and P. Wriggers. An adaptive global-local approach for phase-field modeling of anisotropic brittle fracture. *Comput Methods Appl Mech Eng*, 361:112744, 2020.

M. Paipuri, S. Fernández-Méndez, and C. Tiago. Comparison of high-order continuous and hybridizable discontinuous Galerkin methods in incompressible fluid flow problems. *Math Comput Simulat*, 153:35–58, 2018.

R. U. Patil, B. K. Mishra, and I. V. Singh. An adaptive multiscale phase field method for brittle fracture. *Comput Methods Appl Mech Eng*, 329:254–288, 2018a.

R. U. Patil, B. K. Mishra, and I. V. Singh. A local moving extended phase field method (LMXPFM) for failure analysis of brittle fracture. *Comput Methods Appl Mech Eng*, 342:674–709, 2018b.

W. Qiu, J. Shen, and K. Shi. An HDG method for linear elasticity with strong symmetric stresses. *Math Comp*, 87(309):69–93, 2018.

R. Sevilla, M. Giacomini, A. Karkoulias, and A. Huerta. A super-convergent hybridisable discontinuous Galerkin method for linear elasticity. *Int J Numer Methods Eng*, 116(2):91–116, 2018.

Y. Shao, Q. Duan, and S. Qiu. Adaptive consistent element-free Galerkin method for phasefield model of brittle fracture. *Comp Mech*, 64:741–767, 2019.

Y. Shao, Q. Duan, and S. Qiu. Consistent element-free Galerkin method for three-dimensional crack propagation based on a phase-field model. *Comput Mater Sci*, 179:109694, 2020.

G. C. Sih. Strain-energy-density factor applied to mixed mode crack problems. *Int J Fract*, 10(3):305–321, 1974.

S. C. Soon, B. Cockburn, and H. K. Stolarski. A hybridizable discontinuous galerkin method for linear elasticity. *Int J Numer Methods Eng*, 80(8):1058–1092, 2009.

N. Sukumar, J. Dolbow, and N. Moës. Extended finite element method in computational fracture mechanics: a retrospective examination. *Int J Fract*, 196:189–206, 2015.

C. T. Sun and Z. H. Jin. Fracture Mechanics (1st edition). *Academic Press*, 2012.

E. Tamayo-Mas and A. Rodríguez-Ferran. A medial-axis-based model for propagating cracks in a regularised bulk. *Int J Numer Methods Eng*, 101(7):489–520, 2015.

J.-Y. Wu, V. P. Nguyen, C. T. Nguyen, D. Sutula, S. Bordas, and S. Sinaie. Phase field modelling of fracture. *Adv Appl Mech*, 53, 09 2019.

S. Yakovlev, D. Moxey, R. M. Kirby, and S. J. Sherwin. To CG or to HDG: A Comparative Study in 3D. *J Sci Comput*, 67(1):192–220, 2016.

H. W. Zhang, J. K. Wu, J. Lü, and Z. D. Fu. Extended multiscale finite element method for mechanical analysis of heterogeneous materials. *Acta Mech Sin*, 26: 899–920, 2010.

J. Zhao, Q. Wang, and X. Yang. Numerical approximations to a new phase field model for two phase flows of complex fluids. *Comput Methods Appl Mech Eng*, 310: 77–97, 2016.

Appendix A

Study of the HDG formulation for phase-field models[1]

In this appendix, the HDG formulation for phase-field models presented in Section 2.1 is numerically validated by comparing the results of a well-known benchmark test to those obtained with the standard FEM formulation, for both low and high-order degrees of approximation.

Since the HDG formulations for the equilibrium and the damage equations are based on well-established formulations in the literature, we expect to obtain similar results. However, the study enables to define some numerical considerations when the formulations are applied to phase-field problems, namely, the need of a proper spatial resolution depending on the length-scale parameter l of the model to avoid mesh dependency, and a correct evaluation of the history field $\mathcal{H}$ to prevent oscillations.

A.1 The isotropic phase-field model

Here, we consider the isotropic phase-field model by Bourdin et al. [2000]. Differently to the hybrid phase-field model by Ambati et al. [2015], no tension-compression splitting is considered. For a cracked body in a domain Ω, the system of equations

[1] This appendix is based on Muixí et al. [2018].

reads

$$\begin{cases} \nabla \cdot \boldsymbol{\sigma} = \mathbf{0}, \\ -l^2 \Delta d + d = \dfrac{2l}{G_C}(1-d)\mathcal{H}. \end{cases} \tag{A.1}$$

The stress tensor $\boldsymbol{\sigma}$ is defined as

$$\boldsymbol{\sigma}(\boldsymbol{u}, d) = g(d)\frac{\partial \Psi_0(\boldsymbol{\varepsilon})}{\partial \boldsymbol{\varepsilon}} = g(d)\ \boldsymbol{C} : \boldsymbol{\varepsilon}(\boldsymbol{u}), \tag{A.2}$$

with the quadratic degradation function $g(d) = (1-d)^2 + \eta$, and the history-field variable $\mathcal{H}$ is

$$\mathcal{H}(\boldsymbol{x}, t) = \max_{\tau \in [0,t]} \Psi_0 \left(\boldsymbol{\varepsilon}(\boldsymbol{x}, t)\right),$$

and enforces irreversibility of the crack evolution.

The system of equations (A.1) is to be solved using an incremental procedure for the loading process, this is, evolution is given by incremental boundary conditions. At each load step, we solve the system within a staggered scheme.

A.2 Numerical example: L-shaped panel test

Consider the specimen in Figure A.1 (left), which is fixed on the bottom and has imposed vertical displacement at a 30 mm distance to the right edge. Following Ambati et al. [2015], the material parameters are $E = 25.8423$ GPa, $\nu = 0.18$ and $G_C = 8.9 \cdot 10^{-5}$ kN/mm. The regularization length in the phase-field model is taken as $l = 3$ mm and the residual stiffness is $\eta = 10^{-5}$. The stabilization parameters appearing in the HDG formulations are $\tau = 1$ for both the equilibrium and the damage field equations.

We consider a triangular mesh with 1842 elements, pre-refined along the expected crack path with a mesh size of $h_{\text{ref}} = 3.5$ mm, see Figure A.1 (right), and four nested meshes to this one obtained by dividing the mesh size by two for each level of refinement. The problem is solved with increments in the prescribed vertical displacement of $\Delta u_D = 10^{-3}$ mm. We iterate in the staggered scheme for each load step until convergence is reached, using the relative Euclidean norm for both the damage and the equilibrium fields with a tolerance of 10^{-6}.

Imposing the vertical displacement at just one point causes unphysical damage near the point. This is due to the isotropic model not accounting for a tension-compression splitting, thus cracking is also caused under compression. To cancel this

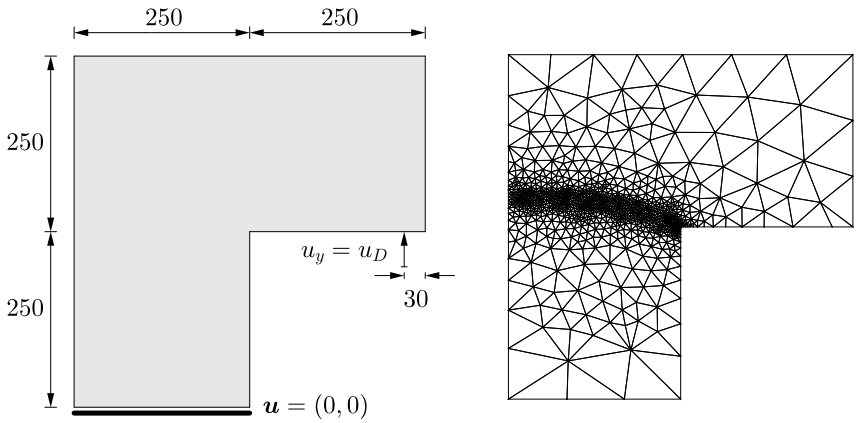

Figure A.1: Geometry and boundary conditions for the test, and coarsest computational mesh. Dimensions are in mm.

out and impose properly the boundary conditions, we set the damage to zero in the region after every iteration of the staggered scheme. Another strategy would be to assign a higher value of G_C where needed, see Wu et al. [2019].

Comparison of FEM and HDG. We start by considering linear approximation functions for both the FEM and the HDG formulations. As expected, the solution tends to converge when refining the mesh. This can be observed in the load-displacement curves in Figure A.2, that show the evolution of the reaction force for an increasing imposed displacement u_D. We obtain similar results for the two formulations, with slightly better accuracy in HDG. Recall that HDG has a better order of convergence for the gradient of the displacement field $\boldsymbol{J}$.

Spatial resolution. Using degree of approximation $p = 1$, the primary mesh with $h_{\text{ref}} = 3.5$ mm is not fine enough to approximate properly the smeared crack with $l = 3$ mm. The obtained diffuse crack becomes mesh-dependent and has a width of one element, as shown in Figure A.3. For the 2-nested level mesh, which is fine enough regarding our choice for the parameter l, the damage field is plotted in Figure A.4. The crack path obtained in this case is comparable to the results in the literature, see Ambati et al. [2015] and Geelen et al. [2018].

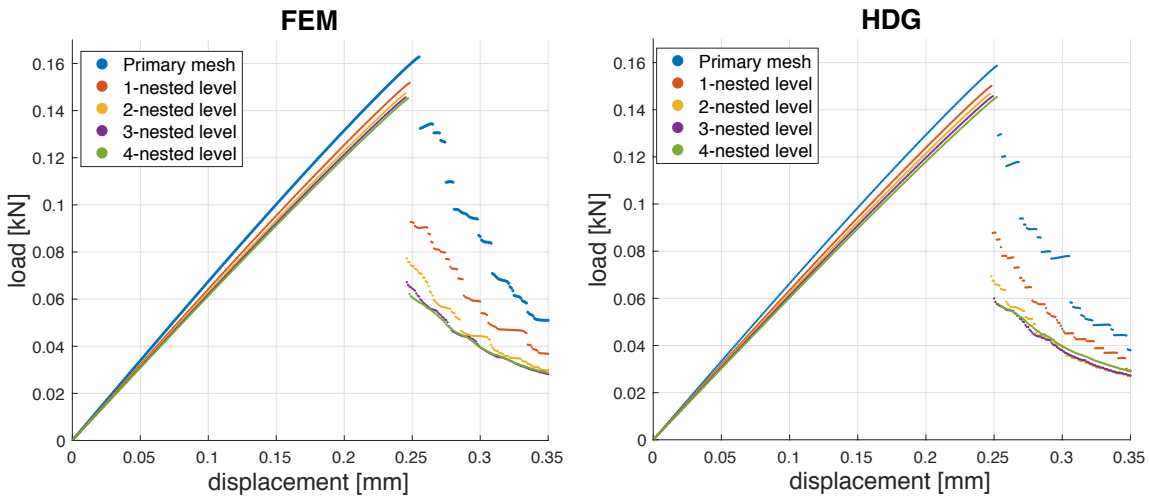

Figure A.2: Load-displacement curves for the L-shaped panel test when using $p = 1$ for both FEM and HDG.

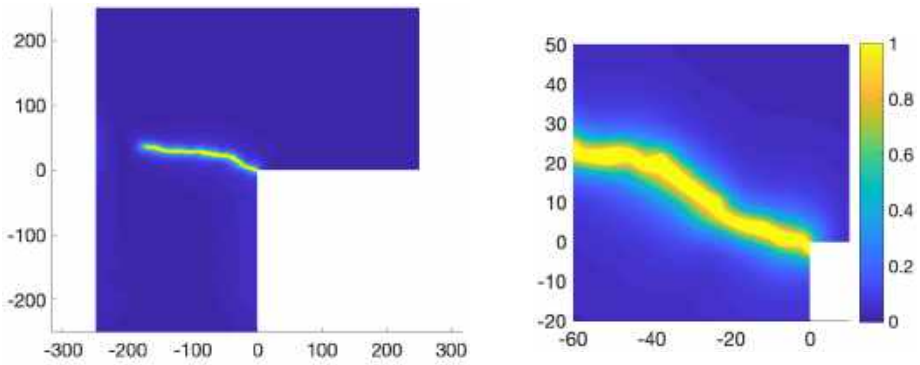

Figure A.3: Damage field obtained with HDG at imposed displacement $u_D = 0.45$ mm. Degree of approximation $p = 1$, primary mesh and $l = 3$ mm.

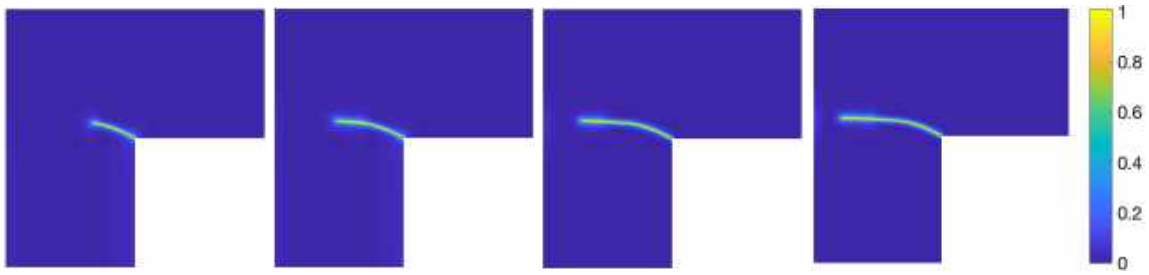

$u_D = 0.25$ mm $\quad$ $u_D = 0.3$ mm $\quad$ $u_D = 0.4$ mm $\quad$ $u_D = 0.5$ mm

Figure A.4: Damage field at some imposed displacements u_D, for degree of approximation $p = 1$, the 2-nested level mesh and $l = 3$ mm.

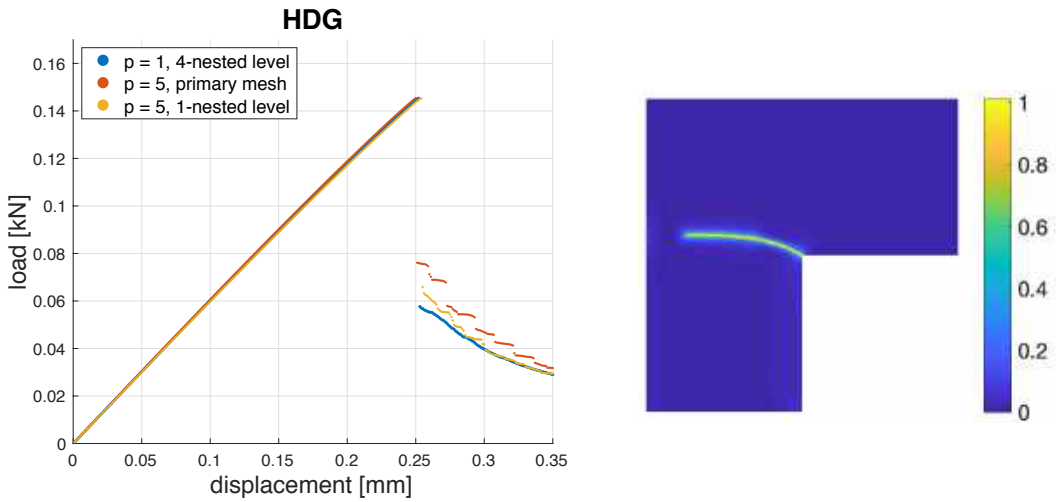

Figure A.5: Left: load-displacement curves obtained with $p = 5$. Right: damage field at $u_D = 0.45$ mm, for $p = 5$ and the primary mesh.

Computation with high-order approximations. To increase the accuracy in space needed to capture the profile of the solution, one can take higher degree p of the approximation basis functions. With $p = 5$, we expect to obtain more accurate results than with $p = 1$ for the same mesh. Indeed, in Figure A.5 (left), we compare the load-displacement curve obtained with degree $p = 1$ and the 4-nested level mesh with the curves obtained for $p = 5$ and coarser meshes. In this case, using a higher-order degree of approximation gives us the same order of accuracy in the solution and with less degrees of freedom. In Figure A.5 (right), we note that solving for $p = 5$ with the primary mesh we no longer observe the mesh dependence we have for $p = 1$ due to low spatial resolution.

Importance of evaluating $\mathcal{H}$ at integration points. If $\mathcal{H}$ is evaluated at nodes and then interpolated to Gauss points, it can reach negative values when using shape functions of degree $p > 1$. To illustrate this phenomenon, let us consider the primary mesh and degree of approximation $p = 5$. If we evaluate $\mathcal{H}$ at nodes, the damage field d is no longer in the interval $[0, 1]$. In Figure A.6, we can see the damage field obtained with this formulation for imposed vertical displacement $u_D = 0.247$ mm. Both the values of d and the pattern obtained are not a proper solution of the problem: the damage field presents oscillations and gets a value of 1.2 at the corner.

For the next load step, corresponding to imposed displacement $u_D = 0.248$ mm, the staggered scheme does not converge. In Figure A.7, we plot the relative Euclidean

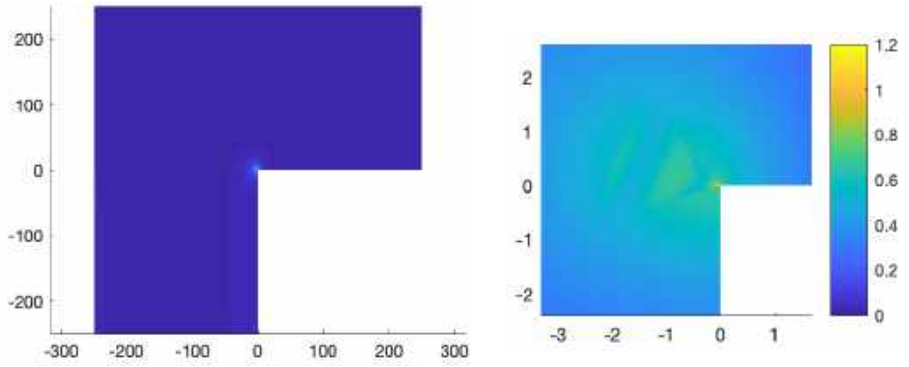

Figure A.6: Evaluating $\mathcal{H}$ at nodes. Damage field for $u_D = 0.247$ mm, with a zoom on the right, for degree of approximation $p = 5$ and the primary mesh. The obtained solution is unphysical.

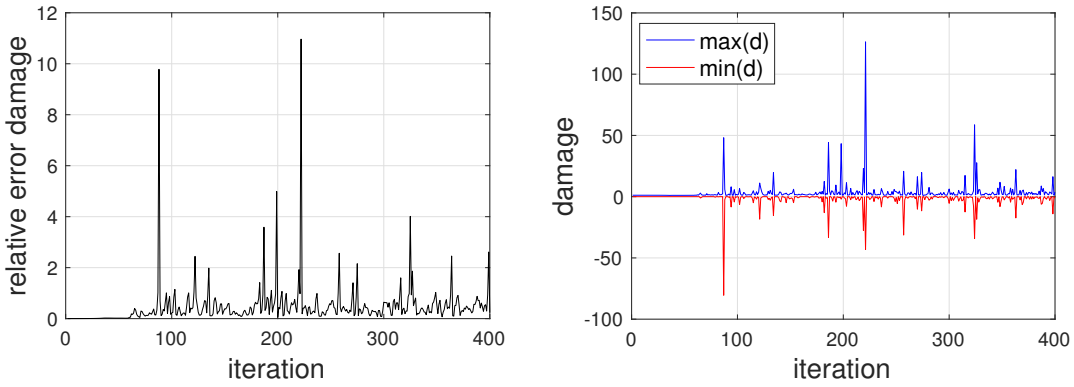

Figure A.7: Evaluating $\mathcal{H}$ at nodes. For imposed displacement $u_D = 0.248$ mm, relative error of d (left) and maximum/minimum values of d (right) for number of iteration. The staggered scheme does not converge in this case.

norm of the difference of consecutive iterates for d and the maximum and minimum values of damage obtained. Notice that the absolute value of the damage field gets arbitrarely large.

A.3 Conclusions

We have compared the results obtained with the proposed HDG formulation for phase-field models in Section 2.1 with a standard FEM formulation in a benchmark test. As expected, both formulations present the same behavior. In particular, the solution is more accurate when refining the mesh or increasing the degree of approximation. With HDG we obtain better accuracy than with FEM for the same mesh and degree

of approximation, but at the price of a higher computational cost, see for instance Kirby et al. [2012] and Yakovlev et al. [2016]. Nevertheless, our interest in HDG for this problem is motivated by the suitability of the method for adaptivity.

For the new HDG formulation, we have observed that poor spatial resolution causes mesh dependency of the solution, as also happens with the FEM. Special care has to be taken in the evaluation of the history field variable $\mathcal{H}$ in order to avoid oscillations of the solution.